MEMO^2: MEthane goes MObile – MEasurements and MOdelling

Temporal and meteorological influences on CH_4 at fixed sites

Malika Menoud
Thomas Röckmann, Dave Lowry

Utrecht University (UU)
Princetonplein 5,
3584 CC, Utrecht
The Netherlands

Telephone: +31 (0)30 253 35 50
Email: m.menoud@uu.nl

Deliverable D2.4

Delivery month Annex I	42		
Actual delivery month	48		
Lead participant: UU	Work package: 2	Nature: Report	Dissemination level: PU
Version: 01			

This project has received funding from the European Union's Horizon 2020 research and innovation programme under the Marie Sklodowska-Curie grant agreement No 722479.

Table of contents

Annex:

Menoud, M., van der Veen, C., Scheeren, B., Chen, H., Szénási, B., Morales, R.P., Pison, I., Bousquet, P., Brunner, D., Röckmann, T., 2020. Characterisation of methane sources in Lutjewad, The Netherlands, using quasi-continuous isotopic composition measurements. Tellus B: Chemical and Physical Meteorology 72, 1–19. https://doi.org/10.1080/16000889.2020.1823733

Menoud M, Van der Veen C., Necki J., Bartyzel J., Szénéasi B., Stanisavljecic M., Pison I., Bousquet P., Röckmann T., 2021. Methane (CH_4) sources in Krakow, Poland: insights from isotope analysis. Atmospheric Chemistry and Physics, in review. Submitted 2021-02-19.

1. Executive Summary

The purpose of this deliverable was answered through two scientific publications (Menoud et al. 2020, Menoud et al. 2021, both attached). The present report synthetizes the key findings in a plain language summary, illustrated with example figures.

We performed continuous measurements of methane (CH_4) mole fraction and isotopic composition (^{13}C and $^{2}H/D$ in methane) in ambient air, at two locations: Lutjewad (The Netherlands) and Krakow (Poland), for 5 to 6 months. The objectives of these observations were to distinguish different sources of CH_4 at a regional scale, based on the different isotopic signatures.

The isotopic composition of CH_4 changes depending on the formation process, which is directly linked to the type of emission, mainly fossil fuel extraction, wetlands, ruminants, waste degradation and biomass burning. Our time series allowed to analyse temporal variations in CH_4 pollution and isotopic signals. By linking this data to the meteorological data, especially wind direction, we could investigate the main emission sources at each study site. An example of the datasets is illustrated in Fig. 1, where CH_4 mole fractions and isotopic compositions collected in Lutjewad are displayed in relation with the wind directions.

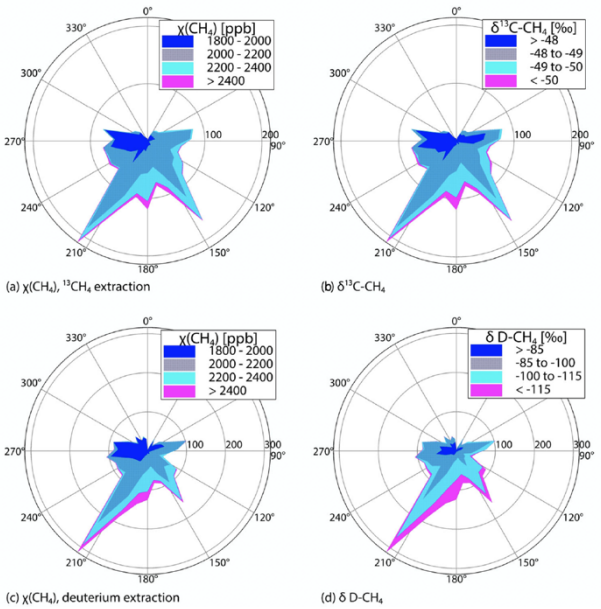

Fig. 1: Wind directions during the ambient air measurement period at utjewad. Bar lengths are number of records (r-axis); colours define the range if CH_4 mole fraction (a and c), $\delta^{13}C$ (b) and δD (d) in CH_4

Each CH_4 increase observed in our time series was related to a certain isotopic signature. Once we derived them for all CH_4 plumes, we could conclude on the emission process and link it to certain geographical locations using the wind data (Fig. 2). The observed time series were compared with simulations made with an atmospheric transport model and based on emissions reported by inventories.

The two sites are affected by different climatology: Lutjewad is a coastal site with an oceanic climate, and Krakow beneficiate a continental climate with comparatively large daily temperature variations. The generally higher windspeeds observed at Lutjewad allowed for a very accurate modelling of the CH_4 signal, because of the relatively small influence of small-scale processes. The timing of the CH_4 elevations in Krakow were not as well reproduced as in Lutjewad.

At Lutjewad, we found no temporal trend in the types of CH_4 emissions throughout the season (November 2016 to March 2017). They were irregularly advected from continental sources mostly related to biogenic CH_4 (cattle farming and waste/sewage management; Fig. 3).

In Krakow, we observed a night-time accumulation, especially in fall and when spring returned (data from September 2018 to March 2019). The local sources were mainly fossil fuel related (Fig. 3). During the winter, winds from the west brought large CH_4 emissions from the exploitation of Silesia coal mines, about 50 km away.

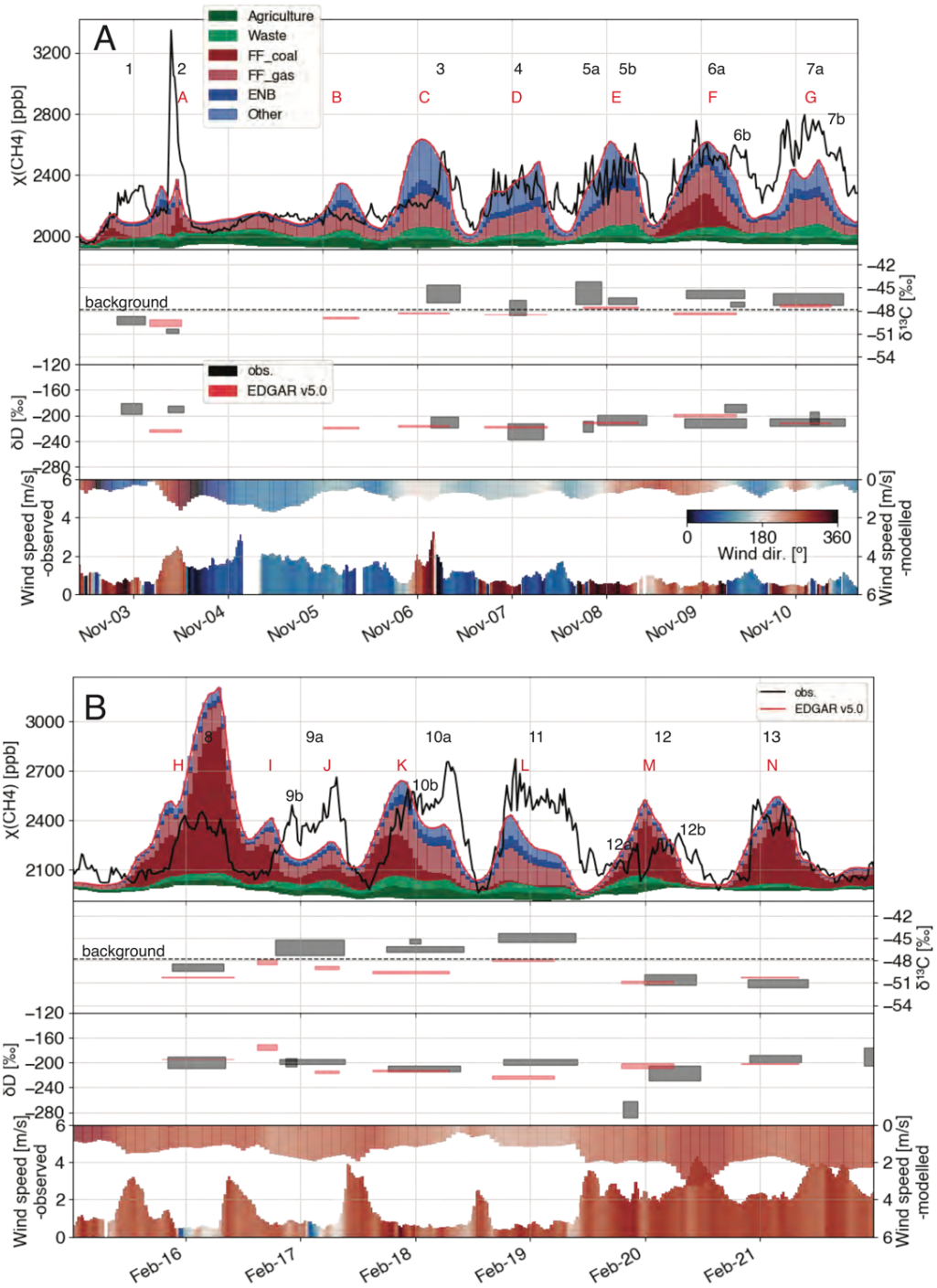

Fig. 2: Detailed analysis of two subsets of the Krakow dataset, (a) from Nov. 2 to 10, 2018, (b) from Feb. 15 to 22, 2019. Top panels: observed (grey) and modelled (red) mole fractions and relative source contributions from the EDGAR v5.0 inventory. Middle panels: δ13C and δ2H source signatures of individual peaks of the observed (grey, from peak 1 to 13) and modelled (red, from peak A to N) time series. Box heights represent ±1 σ of each peak isotopic signature. Bottom panels: wind speed and direction measured simultaneously at the study site (pointing up), and used for the CHIMERE simulations (pointing down).

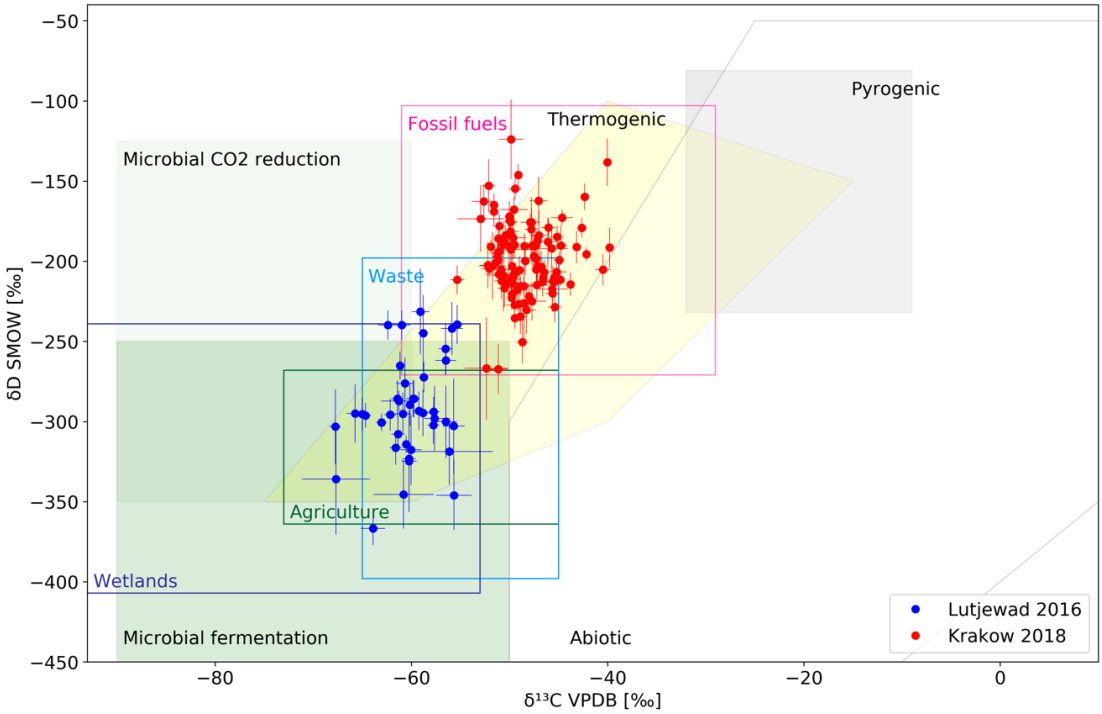

Fig. 3: Dual isotope plot showing the isotopic composition of CH_4 produced from different processes and in different regions. Shaded areas indicate the reported ranges in isotopic composition of CH_4 produced from different geophysical processes (thermogenic, pyrogenic and biogenic). Areas surrounded by colored lines indicate reported isotope signatures from specific source categories (wetlands, agriculture, waste, fossil fuels). Blue and red symbols show isotope source signatures assigned to methane plumes observed in long-time measurement periods at Lutjewad (The Netherlands) and Krakow (Poland).

2. Main conclusions

- The analysis of our results in relation with the wind data allowed for the attribution of the observed plumes to likely source regions/processes.
- We did not observe major changes in the CH_4 emission sources within each studied region, at least not that we could not explain with the wind direction. The CH_4 elevations at both sites were isotopically very different (Fig. 3), even when considering some internal variability.
- CH_4 emissions were affected by daily temperature changes in Krakow, which we didn't observe in Lutjewad. The different climates at our two study sites also influenced the precision of the modelling output.

3. References

Menoud, M., van der Veen, C., Scheeren, B., Chen, H., Szénási, B., Morales, R.P., Pison, I., Bousquet, P., Brunner, D., Röckmann, T., 2020. Characterisation of methane sources in Lutjewad, The Netherlands, using quasi-continuous isotopic composition measurements. Tellus B: Chemical and Physical Meteorology 72, 1–19. https://doi.org/10.1080/16000889.2020.1823733

Menoud M, Van der Veen C., Necki J., Bartyzel J., Szénéasi B., Stanisavljecic M., Pison I., Bousquet P., Röckmann T., 2021. Methane (CH_4) sources in Krakow, Poland: insights from isotope analysis. Atmospheric Chemistry and Physics, in review. Submitted 2021-02-19.

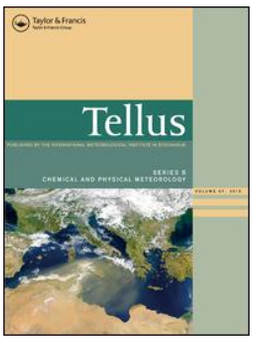

Tellus B: Chemical and Physical Meteorology

ISSN: (Print) (Online) Journal homepage: https://www.tandfonline.com/loi/zelb20

Characterisation of methane sources in Lutjewad, The Netherlands, using quasi-continuous isotopic composition measurements

Malika Menoud , Carina van der Veen , Bert Scheeren , Huilin Chen , Barbara Szénási , Randulph P. Morales , Isabelle Pison , Philippe Bousquet , Dominik Brunner & Thomas Röckmann

To cite this article: Malika Menoud , Carina van der Veen , Bert Scheeren , Huilin Chen , Barbara Szénási , Randulph P. Morales , Isabelle Pison , Philippe Bousquet , Dominik Brunner & Thomas Röckmann (2020) Characterisation of methane sources in Lutjewad, The Netherlands, using quasi-continuous isotopic composition measurements, Tellus B: Chemical and Physical Meteorology, 72:1, 1-20, DOI: 10.1080/16000889.2020.1823733

To link to this article: https://doi.org/10.1080/16000889.2020.1823733

Tellus SERIES B CHEMICAL AND PHYSICAL METEOROLOGY
PUBLISHED BY THE INTERNATIONAL METEOROLOGICAL INSTITUTE IN STOCKHOLM

Characterisation of methane sources in Lutjewad, The Netherlands, using quasi-continuous isotopic composition measurements

By MALIKA MENOUD[1]*, CARINA VAN DER VEEN[1], BERT SCHEEREN[2], HUILIN CHEN[2], BARBARA SZÉNÁSI[3], RANDULPH P. MORALES[4], ISABELLE PISON[3], PHILIPPE BOUSQUET[3], DOMINIK BRUNNER[4], and THOMAS RÖCKMANN[1], [1]*Institute for Marine and Atmospheric Research Utrecht (IMAU), Utrecht University, Utrecht, The Netherlands;* [2]*Centre of Isotope Research, University of Groningen, Groningen, The Netherlands;* [3]*Laboratoire des Sciences du Climat et de l'Environnement, Université de Versailles Saint-Quentin, Paris, France;* [4]*Swiss Federal Laboratories for Materials Science and Technology, Empa, Dübendorf, Switzerland*

(Manuscript Received 20 April 2020; in final form 9 September 2020)

ABSTRACT

Despite the importance of methane for climate change mitigation, uncertainties regarding the temporal and spatial variability of the emissions remain. Measurements of CH_4 isotopic composition are used to partition the relative contributions of different emission sources. We report continuous isotopic measurements during 5 months at the Lutjewad tower (north of the Netherlands). Time-series of $\chi(CH_4)$, $\delta^{13}C\text{-}CH_4$, and $\delta D\text{-}CH_4$ in ambient air were analysed using the Keeling plot method. Resulting source signatures ranged from −67.4 to −52.4‰ vs V-PDB and from −372 to −211‰ vs V-SMOW, for $\delta^{13}C$ and δD respectively, indicating a prevalence of biogenic sources. Analysis of isotope and wind data indicated that (i) emissions from off-shore oil and gas platforms in the North Sea were not detected during this period, (ii) CH_4 from fossil fuel related sources was usually advected from the east, pointing towards the Groningen gas field or regions further east in Germany. The results from two atmospheric transport models, CHIMERE and FLEXPART-COSMO, using the EDGAR v4.3.2 and TNO-MACC III emission inventories, reproduce $\chi(CH_4)$ variations relatively well, but the isotope signatures were over-estimated by the model compared to the observations. Accounting for geographical variations of the $\delta^{13}C$ signatures from fossil fuel emissions improved the model results significantly. The difference between model and measured isotopic signatures was larger when using TNO-MACC III compared to EDGAR v4.3.2 inventory. Uncertainties in the isotope signatures of the sources could explain a significant fraction of the discrepancy, thus a better source characterisation could further strengthen the use of isotopes in constraining emissions.

Keywords: methane, isotope ratio mass spectrometry, source isotopic signatures, emission inventories, in-situ measurements

1. Introduction

Anthropogenic greenhouse gas emissions to the atmosphere are the main driver of the current global climate change. Reducing these emissions is therefore a key goal of climate change mitigation policies. Numerous countries committed to reduce emissions of greenhouse gases as part of the 2015 UN Paris Agreement on Climate Change. This agreement sets an objective to limit future warming to 2 °C (if possible 1.5 °C) compared to pre-industrial temperatures. However, according to Nisbet et al. (2019), the increasing trend in methane concentration in the past years represents a severe threat to reach this goal.

Methane (CH_4) is present at relatively low mole fractions in the troposphere: a global average of 1869 ppb in 2018 is reported by the World Meteorological Organization (WMO, 2019). Yet it is an effective greenhouse gas. The Global Warming Potential (GWP) of CH_4

*Corresponding author. e-mail: m.menoud@uu.nl

Citation: Tellus B: 2020, **72**, 1823733, https://doi.org/10.1080/16000889.2020.1823733

is about 30 kg/kg CO_2 over a 100 year time frame and more than 80 over a 20 year horizon (IPCC, 2013). Furthermore, methane has a relatively short lifetime in the troposphere: 9.1 ± 0.9 years (Saunois et al., 2016). Therefore, focusing on the reduction of methane emissions can effectively contribute to climate change mitigation in the near future.

Methane is emitted from various natural and anthropogenic sources at the Earth's surface. They are usually grouped in three categories: biogenic (e.g. agriculture and farming, waste, biogas production, wetlands and inland water systems), thermogenic (fossil fuel extraction, combustion and consumption, geological sources), and pyrogenic (biomass and biofuel burning). The current understanding of the global methane budget (Saunois et al., 2016) is based on the interpretation of long-term high accuracy atmospheric records (e.g. Dlugokencky et al., 2011), and increasingly satellite retrievals (Monteil et al., 2013; Jacob et al., 2016; Hu et al., 2018; Borsdorff et al., 2019), often used in inverse modelling approaches (Bousquet et al., 2006; Bergamaschi et al., 2009; Rigby et al., 2012; Houweling et al., 2014; Pandey et al., 2017). However, information on the emission rates and locations, and the temporal and spatial variability of the different methane sources still includes large uncertainties both at global (Kirschke et al., 2013; Worden et al., 2017; Pandey et al., 2019; Turner et al., 2019) and regional scales (e.g. Bergamaschi et al., 2018). A better quantification of methane sources is crucial to devise efficient climate change mitigation policies.

The different emission sources can be distinguished using the isotopic composition of CH_4, because its stable isotope content (^{13}C and deuterium) depends on the methane formation process. Measurements of isotopic signatures have been used in many studies to characterise the emissions from individual sites or regions (Levin et al., 1993; Tarasova et al., 2006; Beck et al., 2012; Townsend-Small et al., 2016; Zazzeri et al., 2017). They have also been applied to constrain budget changes in the past (Monteil et al., 2011; Rigby et al., 2012; Schaefer et al., 2016; Worden et al., 2017). Whereas most measurements to date have been performed using analysis in the laboratory on collected samples, field-deployable instruments have only become available recently (Santoni et al., 2012; Eyer et al., 2016; Röckmann et al., 2016).

This article reports high-precision in-situ measurements of methane mole fraction and isotopic composition in ambient air using the isotope ratio mass spectrometry (IRMS) system described in Röckmann et al. (2016). The instrument was deployed for 5 months at Lutjewad, in the North of the Netherlands. The notation $\chi(CH_4)$ refers to methane mole fractions in dry ambient air and is given in nmole/mole or parts per billion, ppb. The isotopic composition is reported in δ notation as:

$$\delta = \frac{R_{sample} - R_{standard}}{R_{standard}}$$

R is the ratio between the heavy and light stable isotopes, here $R = \frac{^{13}C}{^{12}C}$ or $R = \frac{^{2}H \text{ or } D}{^{1}H}$. The standard values are $11180.2 \pm 2.8 \times 10^{-6}$ (Vienna Pee Dee Belemnite, V-PDB) and $155.75 \pm 0.08 \times 10^{-6}$ (Vienna Standard Mean Ocean Water, V-SMOW), respectively for the $\frac{^{13}C}{^{12}C}$ and $\frac{^{2}H}{^{1}H}$ ratios (Werner and Brand, 2001). Both δ^{13}C-CH_4 and δD-CH_4 were continuously measured, together with $\chi(CH_4)$ mole fractions in the air with high-precision IRMS (see below).

Previous measurements made in 2014–2015 at the Cabauw tower in the central Netherlands (Röckmann et al., 2016), showed a prevalence of isotopically depleted sources of methane in the footprint of the station, demonstrating a large contribution from agricultural activities. Landfills and natural gas operations were identified as secondary sources. The Lutjewad coastal site is closer to the on-shore and off-shore North Sea oil and gas installations. One goal was to investigate whether emissions from these anthropogenic sources are more important at Lutjewad compared to the Cabauw site. Off-shore gas extraction facilities emit CH_4 through gas flaring, oil loading, as well as fugitive and operational emissions (Riddick et al., 2019). The detection of methane emissions by these sites was discussed in Yacovitch et al. (2018), based on aircraft measurements along the Dutch coast. They crossed a methane plume during a flight, but could not draw a robust conclusion on its origin. They hypothesised that emissions from offshore platforms may result in a broad elevated baseline $\chi(CH_4)$, combined with sharper signals from other local sources. The isotopic measurements in this study are expected to help assess the influence of different sources on these coastal pollution events. The observations are also interpreted by comparison with two atmospheric dispersion models, based on two emissions inventories. The observations are used to evaluate the model performance and to test our understanding of methane sources and their isotopic signatures in the Netherlands and the surrounding regions.

2. Methodology

2.1. Study site

From the 3rd of November 2016 to the 31st of March 2017, measurements of $\chi(CH_4)$, δ^{13}C-CH_4, and δD-CH_4 in ambient air were conducted at the Lutjewad atmospheric station (53°24'13.5"N, 6°21'10.6"E). This 60 m-tall tower is located in the north of the Netherlands, on the Wadden Sea coast (Fig. 1). The station is part of the Integrated Carbon Observation System (ICOS) network, and continuously provides data on CO_2, CH_4 and CO mole fractions at 60 m height.

The surrounding area on land is mostly covered by intensive agriculture, including grazing land and production of

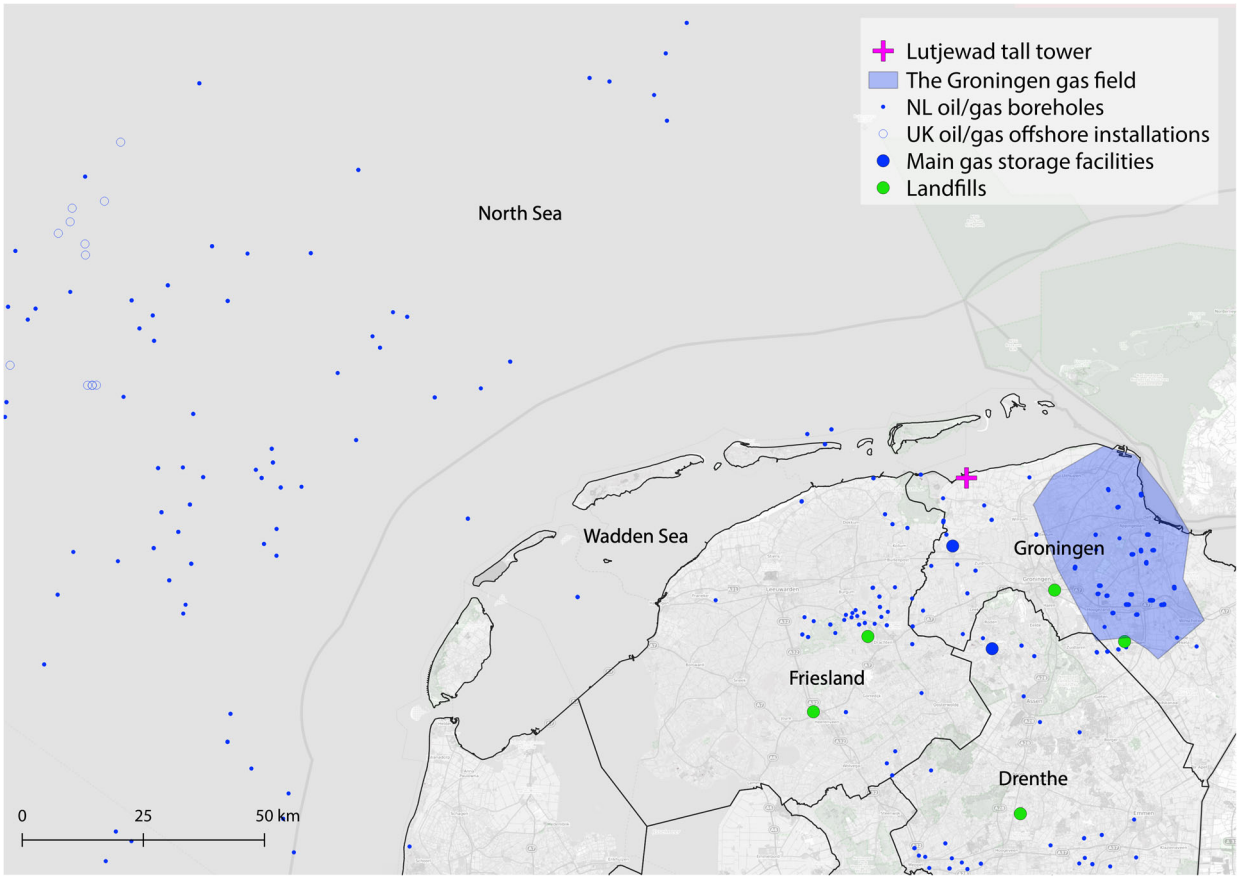

Fig. 1. Location of the measurement site (magenta cross) and potential on-shore and off-shore methane sources. Sources: https://www.openstreetmap.org, OSPAR Commission (2015), Vlek (2018), Ministerie van Economische Zaken, TNO (2018), and Stortplaatsen in Nederland (2019).

vegetables, mais and other cereals (Wageningen University & Research, 2015). The region has one of the highest livestock densities in Europe, among which a majority of bovines since the largest dairy farms in the Netherlands are in the province of Friesland (European Union, 1995; Fig. 1). The region is also characterised by the extraction of natural gas from sandstone layers at about 3 km depth. Locations of individual onshore boreholes are shown in Fig. 1. The Groningen gas field, the biggest natural gas reservoir of the Netherlands, is located east/southeast of Lutjewad at a distance of about 30 km (Fig. 1).

In the North Sea, between the Netherlands and the UK, a total of 445 platforms for oil and gas extraction are in operation (OSPAR Commission, 2015). They are mostly located in the west and northwest of Lutjewad (Fig. 1).

2.2. Measurements

2.2.1. Isotope ratio mass spectrometry system. The isotope measurement system is based on a continuous flow isotope ratio mass spectrometry (CF-IRMS) system. One IRMS instrument (Thermo Delta Plus XP, Thermo Fisher Scientific Inc., Germany) was used to measure alternatively ^{13}C-CO_2 and ^{2}H-H_2. Before injection into the mass spectrometer, CH_4 needs to be isolated from the other air components and converted to CO_2 or H_2. To extract the CH_4, ambient air is first pumped through magnesium perchlorate, a drying agent. Then, the dry air is sent through two successive cryogenic traps, cooled to $-120\,^{\circ}C$ and filled with HayeSep D in the center and glass beads on each end. The cooling is achieved by a Polycold compact cooler compressor (Brooks Automation Inc., USA), filled with coolant PT-30. The cold end is attached to a copper block on which the traps are mounted. The traps are kept under vacuum to avoid condensation of water and to allow a fast and precise temperature control of each of them. The methane is released by heating the traps to $-45\,^{\circ}C$, and then it is converted to CO_2 and H_2 in combustion and pyrolysis furnaces, at temperatures of 1150 and $1350\,^{\circ}C$, respectively. CO_2 is further purified on a gas chromatography (GC) column, at a temperature between 0 and $10\,^{\circ}C$. The

whole extraction process is illustrated in Fig. S1, and described in more detail in Röckmann et al. (2016). A picture of the extraction system installed at Lutjewad is shown in Fig. S2.

The fully automated system achieves one measurement of δ^{13}C- or δD-CH_4 every 20 min, together with the CH_4 mole fraction. Ambient air measurements were alternated with measurements of air from a reference cylinder. The cylinder contained air with 1974.0 ppb CH_4, and isotope values of $\delta^{13}C = -47.75 \pm 0.05‰$ vs V-PDB and $\delta D = -87.9 \pm 1.1‰$ vs V-SMOW, linked to a previous calibration against the international standard material at the Max Planck Institute for Biogeochemistry, Jena, Germany (Sperlich et al., 2016). After processing, the data resulted in time series for δ^{13}C-CH_4 and δD-CH_4 in ambient air, at a non-regular interval of 51 minutes on average.

CH_4 mole fractions were measured continuously by two CRDS (cavity ring-down spectrometry) instruments (model G2301 until 13/12/2016 followed by model G2401 since then, Picarro inc., CA, USA) connected to the same inlet as the IRMS. A set of instrument-specific empirical water vapor correction factors were used to derive CH_4 dry air mole fractions (Chen et al., 2010; Rella et al., 2013). For calibration of the G2301 CRDS we used working standard mixtures made in-house from dried ambient air and a suite of 5 primary standards (provided by the Earth System Research Laboratory (ESRL) of the National Oceanic and Atmospheric Administration (NOAA)) linked to the World Meteorological Organization (WMO) X2004 scale for CH_4. Together with the installation of the G2401 CRDS we replaced our calibration tanks by a suite of new ICOS standard mixtures prepared by the ICOS Central Analytical Laboratory (Jena, Germany) linked to the WMO X2004A scale for CH_4 for calibration. The total uncertainty of the CRDS $\chi(CH_4)$ was estimated to be 2 ppb. The measurements were made at 1 Hz; however, minute averaged values were used for the analyses. The measured $\chi(CH_4)$ from the IRMS were compared to these values. To do so, the time series were cut into subsets from 3 h to 8 days, according to maintenance breaks in the measurements. The average difference between the IRMS and CRDS $\chi(CH_4)$ values was calculated for each subset but only for $\chi(CH_4)$ <2250 ppb, because the values changed very rapidly during pollution events. If the average difference was larger than its standard deviation, it was considered a significant offset. The IRMS data were then corrected relatively to the CDRS values by applying this average difference. Corrections were finally applied to 62% of the data. They ranged from 2.17 to 112 ppb. Not every subset had a significant offset, and these $\chi(CH_4)$ differences were always very stable within each subset.

2.2.2. Meteorological data. Hourly measurements of wind speed and wind direction were used to interpret the methane time series. The meteorological data collected at Lutjewad at the different heights (7, 40 and 60 m above ground) were incomplete with missing data from 23 January 2017, onwards. Therefore, another dataset was used, from a nearby station of Lauwersoog (53°25'N 6°12'E), operated by The Royal Netherlands Meteorological Institute (KNMI). It is situated at about 10 km from the Lutjewad tall tower, and wind measurements at 10 m height are available for the entire measurement period. Both datasets show very similar wind characteristics despite the spatial and elevation difference.

2.3. Modelling

Using the atmospheric transport models CHIMERE and FLEXPART-COSMO, the time series of $\chi(CH_4)$, δ^{13}C-CH_4 and δD-CH_4 at the Lutjewad tall tower were modelled for the period of the measurements. CH_4 was treated as a non-reactive tracer in the models, considering the limited size of the domain and the correspondingly short residence time of the air compared to the lifetime of CH_4.

CHIMERE is a Eulerian regional chemistry-transport model (Menut et al., 2013; Mailler et al., 2017), here driven by the PYVAR system developped for forward comparison of model outputs and observations and variational inversions (Fortems-Cheiney et al., 2019). Forward simulations of CH_4 mole fractions were carried out at a horizontal resolution of 0.1° × 0.1° over a domain covering [43.6–55.6 N] in latitude and [5.0 W–12.0 E] in longitude. For the simulations, 29 vertical levels were used, reaching up to a top pressure of approximately 300 hPa. The meteorological data used to drive the model were taken from the European Centre for Medium-Range Weather Forecast (ECMWF) operational forecast product with a 10 km horizontal and 3-hour temporal resolution. The boundary and initial $\chi(CH_4)$ conditions were obtained from the analysis and forecasting system developed in the Monitoring Atmospheric Composition and Climate (MACC) project (Marécal et al., 2015). The version used for this study consists of 71 vertical levels, a horizontal resolution of 0.563° × 0.653°, and a temporal resolution of three hours. The meteorological products and the mole fraction fields were interpolated to the model domain both spatially and temporally by the PYVAR-CHIMERE system.

The FLEXPART-COSMO model is a version of FLEXPART (Pisso et al., 2019), an offline Lagrangian particle dispersion model (LPDM). This version uses the output of the mesoscale numerical weather prediction model COSMO (Baldauf et al., 2011) as the driving

Table 1. Initial $\delta^{13}C$ and δD values from literature used in the models for the different emission sectors (Szénási 2019). They are derived from signatures found in the cited studies. The range of values is reported in the brackets. Only the $\delta^{13}C$ value for fossil fuel emissions (bold) was modified from Szénási 2019 to better represent the emissions from this sector in the Netherlands.

Emission sector	δ13C-CH4 [o]	δD-CH4 [o]	Literature source
Agriculture	−68.0 [−70.6; −46.0]	−319 [−361; −295]	Uzaki et al., 1991; Levin et al., 1993; Tyler et al., 1997; Bréas et al., 2001; Bilek et al., 2001; Klevenhusen et al., 2010; Röckmann et al., 2016
Waste	−55 [−73.9; −45.5]	−293 [−312; −293]	Games and Hayes, 1976; Levin et al., 1993; Bergamaschi et al., 1998; Zazzeri et al., 2015; Röckmann et al., 2016
Extraction and distribution of fossil fuels & non-industrial combustion	**−40.0** [−66.4; −30.9]	−175 [−199; −175]	Levin et al., 1999; Lowry et al., 2001; Thielemann et al., 2004; Zazzeri et al., 2016; Röckmann et al., 2016
Other anthropogenic sources	−35.0 [−60; −9]	−175 [−175; −81]	Levin et al., 1999; Chanton et al., 2000; Nakagawa et al., 2005; Röckmann et al., 2016
Natural wetlands	−69 [−88.9; −51.5]	−330 [−358; −246]	Tyler et al., 1987; Smith et al., 2000; Galand et al., 2010; Happell et al., 1995; Martens et al., 1992; Bilek et al., 2001; Sugimoto and Fujita, 2006

meteorology. All meteorological fields are preserved on the original COSMO vertical grid, which strongly reduces uncertainties in the interpolation, compared to other versions of FLEXPART (Henne et al., 2016). For this study, FLEXPART-COSMO was driven by hourly output of the operational COSMO-7 analyses of the Swiss weather service MeteoSwiss at a horizontal resolution of 7 km × 7 km and with 60 vertical levels. 50,000 Lagrangian particles (air parcels) were released from the location of the monitoring site and its inlet at 60 m above surface every 3 hours and followed backwards in time over 4 days in order to derive sensitivity maps or footprints (Seibert and Frank, 2004).

The input anthropogenic CH_4 emissions were extracted from two gridded inventories for 2011: the EDGAR v4.3.2 (Janssens-Maenhout et al., 2017) and TNO-MACC III (Kuenen et al., 2014), with a horizontal resolution of approximately 11 km × 11 km and 7 km × 7 km, respectively. The CHIMERE simulations also used natural wetland emissions obtained from the ORCHIDEE-WET model (Ringeval et al., 2011) for 2009.

To be able to compare the two inventory outputs, the anthropogenic emission categories were grouped under the SNAP (Selected Nomenclature for Air Pollution) level-1 sectors (EEA (European Environment Agency), 2000). The emissions from five source categories were used to model the $\chi(CH_4)$ in CHIMERE: agriculture (SNAP 10), waste (SNAP 9), wetlands (SNAP 11), non-industrial combustion plants (SNAP 2), and production, extraction and distribution of fossil fuels (SNAP 5). The rest was characterised as" other" emission sources. In the results, SNAP 2 and SNAP 5 sectors were combined into one category for fossil fuel. The total simulated CH_4 mole fraction is a combination of the contribution of these emission sources and the background.

The $\delta^{13}C$-CH_4 and δD-CH_4 time series were calculated by both models based on the combination of the simulated CH_4 mole fractions for each source category and their associated isotopic signatures taken as one scalar per category, and were assigned based on previous studies (Table 1). The background isotopic signatures were obtained from the 3-hourly simulations of $\delta^{13}C$ and δD using the Laboratoire de Météorologie Dynamique (LMDz) model (Hourdin et al., 2006). The simulations followed the methods described by Thanwerdas et al. (2019). The values were taken from a model grid-cell above the North Atlantic. The background $\delta^{13}C$ values from this global model are on average −0.2‰ lower than the ones from the measurements. A corresponding correction was applied to the background isotopic composition to align it to the observations. The background δD values were also raised by 12‰, to better correspond to the observations. This correction is rather large, but corresponds to an offset between the scales of two groups of institutes - IMAU at Utrecht University, the Max Planck Institute for Chemistry in Mainz, Germany (MPIC), the National Institute for Water and Atmospheric Research in Wellington, New Zealand (NIWA) on the one hand and the University of California Irvine (UCI), Tohoku University (TU), the Institute of Arctic and Alpine Research (INSTAAR), and Pennsylvania State University (PSU) on the other hand - that was identified in an

international inter-comparison of isotope scales (Umezawa et al., 2018).

The total $\delta^{13}C$ and δD at each time point were computed in the following way:

$$\delta = \frac{1}{x(CH_4)_{tot}} \sum_{i}^{n=6} \delta_{s,i} * x(CH_4)_i$$

with δ_s being the source signatures defined in Table 1, for each emission sector i including the background.

2.4. Data analysis

The data were analysed using a Keeling plot approach (Keeling, 1961; Pataki et al., 2003), to obtain the source isotopic signatures of the recorded pollution events. This method is based on a mass balance equation considering addition of CH_4 from a single emission source (s) of a certain compound to a stable background (bg) in the measured sample (m):

$$\delta_m c_m = \delta_{bg} c_{bg} + \delta_s c_s$$

where δ is the isotopic value and c the mole fraction of the compound.

Re-arranging the equation, a linear relation can then be derived between $1/c_m$ and the measured isotopic signature (δ_m). The intercept corresponds to a maximum (infinite) concentration, that reflects the emission source isotopic signature δ_s:

$$\delta_m = \frac{c_{bg}}{c_m}(\delta_{bg} - \delta_s) + \delta_s$$

In the case of a mixture of several sources, δ_s may reflect the mean isotopic signature, weighted by emissions from the individual sources.

The Keeling plot method was applied in a similar way as in Röckmann et al. (2016), but with slight modifications. The moving time window had a width of 12 h of data and moved in steps of 1 h. At each step, $\chi(CH_4)$ values below the lower 10% percentile, and <2100 ppb, taken within a larger 24 h window were also included as background. A minimum number (n) of 5 points and a $\chi(CH_4)$ range of at least 200 ppb were used to select suitable datasets in these time windows. An orthogonal distance regression was then applied to determine the intercept of the $\delta_m : 1/c_m$ correlation and its uncertainty. Only linear fits with a standard error of the regression $s < 2.5‰$ were selected for further evaluation. This represents the typical distance between the data and the regression line. If this condition was not fulfilled, the window was narrowed by 1 h, until either $n < 5$ (rejected) or $s < 2.5‰$ (selected).

The signatures obtained were then filtered for those with a well-defined isotopic composition, indicating that the dataset can be fit assuming a source with a constant isotope signature. The following criteria was applied:

$$\sigma_{\text{intercept}} < \begin{cases} 1.5‰ & \text{for } \delta^{13}C \\ 30‰ & \text{for } \delta D \end{cases} \text{ and } \sigma_{\text{winddir.}} < 90^{\circ}$$

with $\sigma_{\text{intercept}}$ and $\sigma_{\text{winddir.}}$ being the standard deviation of the regression intercept and of the wind directions in the window. Applying these criteria filtered out 14% of the initial signatures from the moving window Keeling plot in total. The $\sigma_{\text{intercept}}$ threshold filters out more data than the one for the $\sigma_{\text{winddir.}}$.

In some cases, several regression intercepts were derived from the same pollution event, i.e. when a $\chi(CH_4)$ peak was longer than 12 h. In this case, they were averaged over the duration of the peak to obtain one source signature per pollution event.

3. Results

3.1. Overview

The complete dataset measured over 5 months is shown in Fig. 2. The gaps in the data are caused by technical failures.

The $\chi(CH_4)$ time series shows pronounced variability, compared with measurements from the Mace Head background station in Ireland made by the Advanced Global Atmospheric Gases Experiment (AGAGE, Prinn et al., 2008). In the first half of the period (until mid January 2017), CH_4 elevations were interrupted by periods when background values prevailed over longer periods. For example, the $\chi(CH_4)$ stayed stable and matched Mace Head values over a few days in the end of December 2016. The average $\chi(CH_4)$ measured at Mace Head was 1950 ± 39 ppb, which compares well with the observed background value of 1933 ± 11 ppb from Lutjewad (average of the lower 10% percentile of $\chi(CH_4)$).

The $\delta^{13}C$ time series can also be compared to measurements from flask samples taken at Mace Head, by the National Oceanic and Atmospheric Administration (NOAA; Dlugockenky et al., 2019; Fig. 2). No measurements are available for δD, but we expect δD values at Mace Head to match the background values from the Lutjewad measurements in a similar way as for $\delta^{13}C$. CH_4 elevations in the Lutjewad dataset are systematically accompanied by negative excursions of both $\delta^{13}C$ and δD values. The isotopic values reached down to $-51.8‰$ for $\delta^{13}C$ and $-147‰$ for δD, whereas the average background was -47.7 ± 0.21 and $-84.2 \pm 5.2‰$, respectively. The background from the measurements, calculated as the average of the 10% lower percentile of $\chi(CH_4)$, compares well with the average $\delta^{13}C$ of $-47.7 \pm 0.1‰$ at Mace Head during the time period.

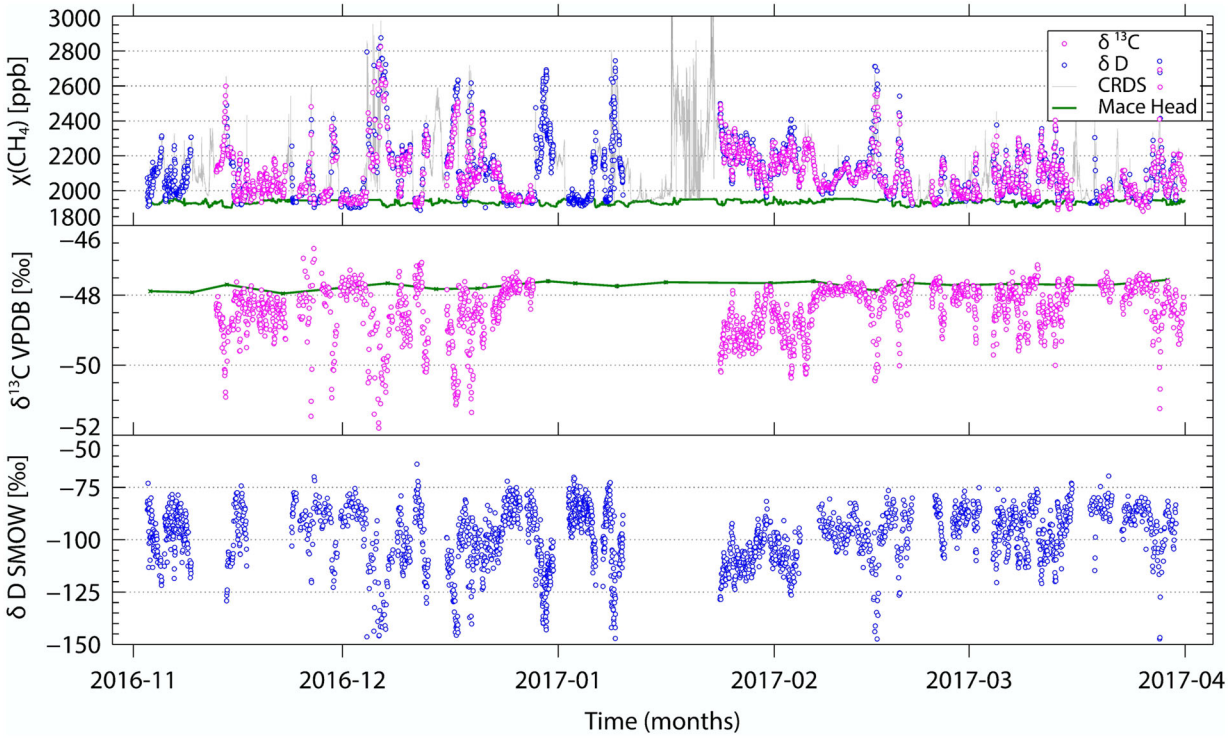

Fig. 2. Overview of the entire dataset, including corrections made on IRMS $\chi(CH_4)$ to match the CDRS records. The Mace Head $\delta^{13}C$-CH_4 data (Dlugockenky et al., 2019) was corrected by $-0.11‰$ according to the scale difference between the INSTAAR and the IMAU measurements evaluated in Umezawa et al. (2018).

In Fig. 3, the recorded methane and isotope data are plotted in wind roses. The main wind directions during the study period were from south-west (195° to 225°) and south-east (150°). A north-east to south-west line separates the land and sea. One can see that most of the pollution events originate from the land, and that periods with a pronounced northerly wind component were rare. The wind from the sea generally advects air with background $\chi(CH_4)$.

Accordingly, the background isotopic signatures are also observed during periods with north/north-west winds. Background isotope values are the high values for $\delta^{13}C$ and δD. The measured methane enhancements are mostly caused by isotopically depleted sources from the land, especially in the south, from which the lowest $\delta^{13}C$ and δD values were measured.

We also investigated the daytime-nighttime difference of mole fraction and isotope values (shown in Fig. S3). Background values of $\chi(CH_4)$, lower than 2000 ppb, are observed more often during the day than at night. Indeed, 35.5% of daytime $\chi(CH_4)$ records are lower than 2000 ppb, compared to only 30.5% nighttime. Small elevations in $\chi(CH_4)$ (lower than 2300 ppb) occur more during the night. Yet there is no clear distinction between daytime and nighttime for higher CH_4 elevations.

3.2. Model results

3.2.1. Time series. Modelled time series generated with CHIMERE and FLEXPART-COSMO are shown in Fig. 4(a,b). In general, the timing of the pollution events is in good agreement with the observations, and this is also true for the variations in the isotope signatures.

Figure S6 shows $\chi(CH_4)$, $\delta^{13}C$ and δD-CH_4 histograms from the measurements and model results. Correlation plots between model and observations are also provided in the supplementary material (Fig. S7). According to the distribution of CH_4 mole fractions in Fig. S6(a), higher $\chi(CH_4)$ elevations are less present in the simulation results compared to the measurements, especially from CHIMERE. This variation is likely due to the comparison between hourly averages of instant measurements at a certain location and values over a larger grid cell provided by the model. The general $\chi(CH_4)$ distribution is better reproduced with FLEXPART-COSMO (Fig. S7(a)). A higher proportion of $\chi(CH_4)$ values between 2050 and 2100 ppb was computed with CHIMERE, mostly from an overestimation of the mole fractions in March 2017 (Fig. 4(a,b)).

The difference between model results and observations at higher mole fractions also affects the isotopic composition. Figure 6(a,b) show that the modelled isotopic

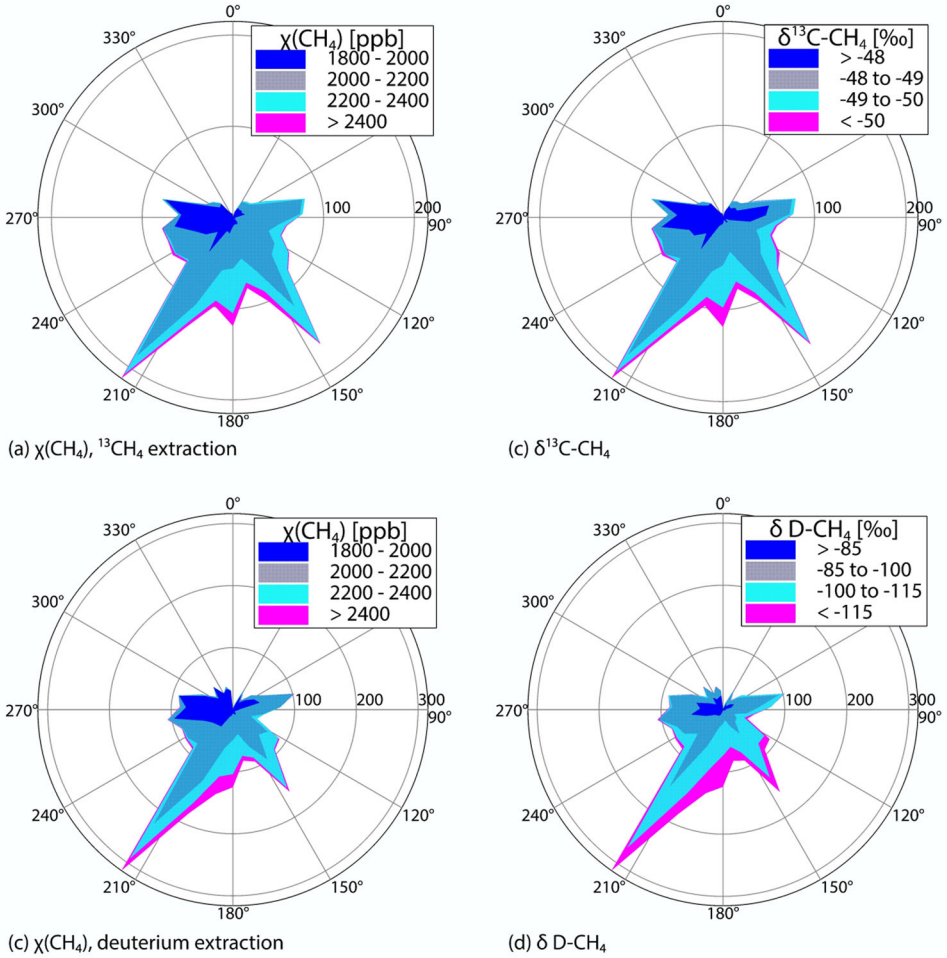

Fig. 3. Wind rose diagrams of $\chi(CH_4)$, $\delta^{13}C\text{-}CH_4$, and $\delta D\text{-}CH_4$, in number of records with respect to the wind direction. The North is set at 0°, as for all the direction angles throughout the article.

signatures are often less depleted than the measured ones, especially for the FLEXPART-COSMO simulations. In general, the differences are also higher for δD, but the time series of this isotope also have higher uncertainties.

There is no clear difference between the use of the TNO-MACC III inventory and the EDGAR v.4.3.2 inventory regarding the overall distribution of $\chi(CH_4)$ and $\delta D\text{-}CH_4$. For $\delta^{13}C\text{-}CH_4$, using the TNO-MACC III inventory leads to more enriched values than with EDGAR v.4.3.2 (Fig. 6(a)).

3.2.2. Source partitioning. The contributions from each CH_4 source category as computed with the CHIMERE model are presented in Table 2. The dominant source is the agriculture sector, with a contribution close to 60%. The second most important source is waste, followed by emissions from fossil fuels. Other sources and wetlands contribute less than 10%. Both inventories agree on the ranking of the different sources. The largest difference is in the share of the fossil fuel contribution. When TNO-MACC III inventory is used, the contribution of fossil sources to the modelled CH_4 elevations is about 45% larger than for EDGAR v4.3.2.

3.3. Source signatures

From the Keeling plots of the entire observations dataset (Fig. S4(a,b)), the total averaged source signatures are $-59.55 \pm 0.13‰$ and $-287.2 \pm 1.4‰$ for $\delta^{13}C$- and $\delta D\text{-}CH_4$, respectively. These values are typical for microbial (including waste) methane emissions, in agreement with the source attribution from the model.

The results from the moving window Keeling plots also show a prevalence of isotopically depleted sources: the mean isotope signatures of the evaluated peaks are respectively $-60.3 \pm 3.1‰$ and $-286.3 \pm 27.5‰$ for $\delta^{13}C$ and δD. These values agree within the uncertainties with the Keeling plot intercepts made with all points of the

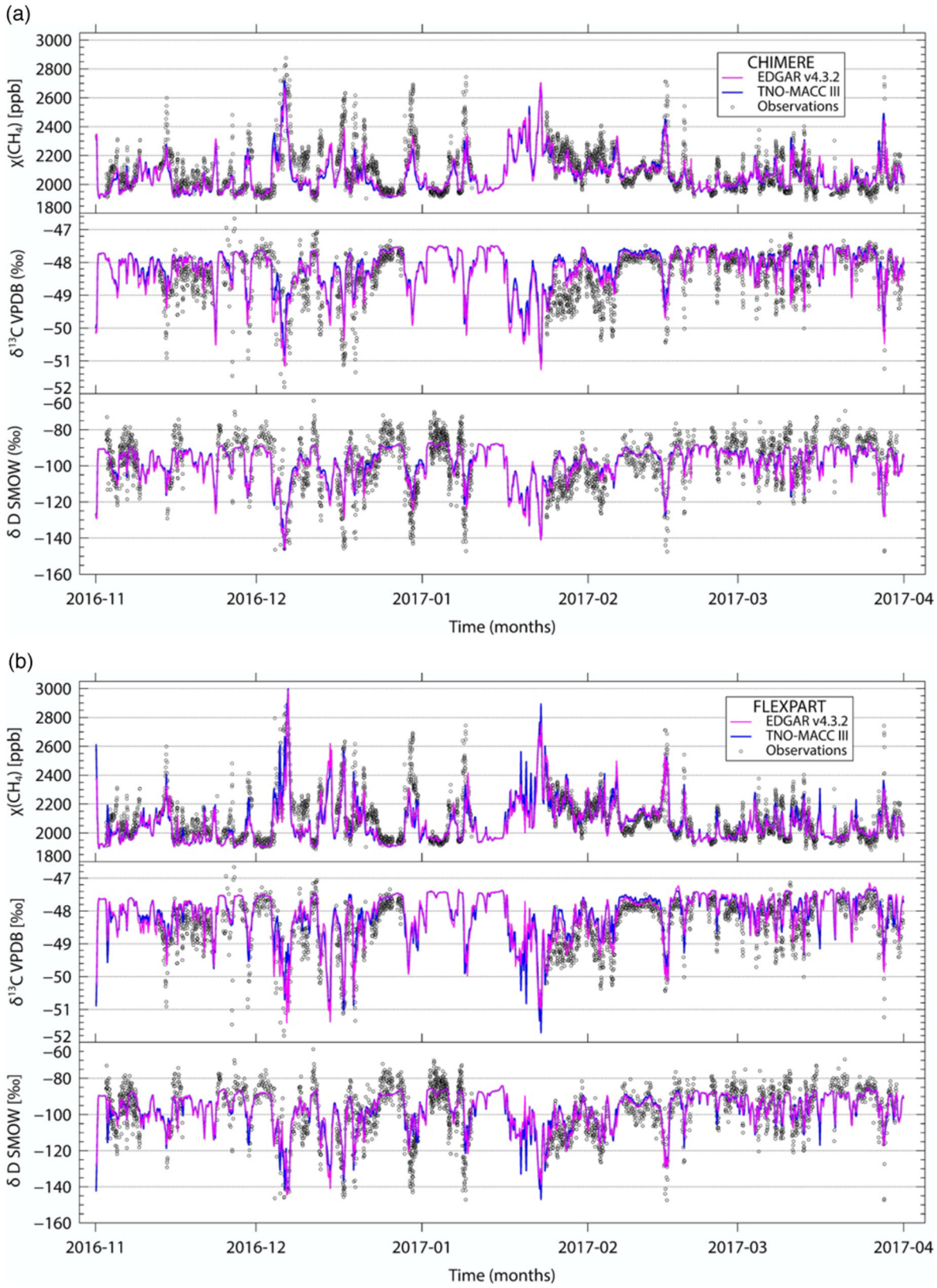

Fig. 4. Model results from CHIMERE and FLEXPART-COSMO, using two emission inventories.

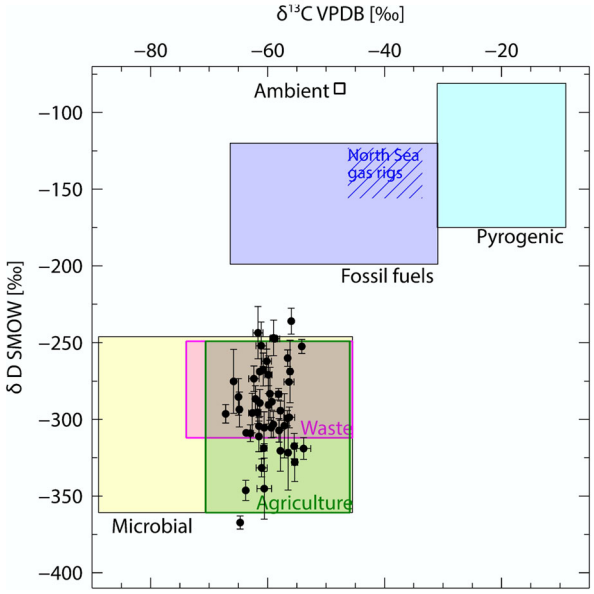

Fig. 5. δ^{13}C- and δD-CH_4 source signatures, derived with the moving window Keeling plot approach (black dots). The background CH_4 isotopic composition corresponds to the 10th lower percentile of the $\chi(CH_4)$ in this study's dataset. Colored areas indicate typical isotope signatures for CH_4 (referred in Table 1 and partially from unpublished measurements of biogenic sources made in the Netherlands). The δ^{13}C of the North Sea gas rigs is between −32 and −45‰, from Hitchman, S. P. (1989), Cain et al. (2017) and Riddick et al. (2019).

dataset. Figure 5 compares our observed atmospheric average isotopic signatures to typical ranges for specific sources in previous studies. Almost all of the source signatures from Lutjewad fall within the 'Agriculture' and 'Waste' areas, that are anthropogenic emissions of 'Microbial' origins. The δD and δ^{13}C spread suggests variations in the contribution from thermogenic sources. The reported isotopic composition of North Sea and on-shore Dutch natural gas lie in the upper range of thermogenic ^{13}C (^{13}C-$CH_4 = -33 \pm 1$‰ reported by Cain et al. (2017), ^{13}C-$CH_4 = -43.7$‰ reported by Riddick et al. (2019), and δD-$CH_4 = -158$ to -121‰ reported by (Hitchman, S. P. 1989). This already shows that the observed methane elevations contain only relatively small fractions of thermogenic methane.

Histograms of the peak source signatures are shown in Fig. 6. The source signatures from modelled time series also fall in the range of biogenic emissions. Using the TNO-MACC III inventory leads to more enriched source signatures because of its higher proportion of fossil fuel emissions.

3.4. Individual pollution events

Two periods were selected to analyse individual pollution events in more detail, together with results from the CHIMERE model. The Keeling plots for a moving time window were also applied to the CHIMERE results, using the same criteria as for the observations. The first subset is from the 16–21 December 2016 (Fig. 7) and the second from the 10–16 March 2017 (Fig. 8).

In the first subset (16–21 December 2016), there are three pollution events of relatively high magnitudes. They are labelled in Fig. 7 as 1 (December 17), 2 (December 19), and 3 (December 21). The elevations are also seen in the CHIMERE model results, albeit with lower magnitude, likely due to the rather coarse resolution of this model. Wind directions varied considerably during this time period: 219 ± 30°, 149 ± 32°, and 179 ± 21°N, respectively for each event (Fig. 7). The isotope source signatures of the first two events are between −64.3 and −62.6‰ for δ^{13}C and between −323 and −297‰ for δD in the measurements, but increase to −55.1‰ for δ^{13}C and −233‰ for δD during the third event. The model captures the isotope signatures of the three events relatively well when the EDGAR inventory is used. The TNO-MACC III inventory shows an increase in fossil fuel-related emissions on December 19th and 20th, and a corresponding δ^{13}C enrichment. For event 2, this is not confirmed by the measured δ^{13}C values, which indicate a prevalent biogenic source. For event 3, the measured δD source isotopic signature reaches −232 ± 6.7‰, the highest value derived from this dataset. In Fig. 5, this point clearly falls outside typical isotope signatures for biogenic sources and waste. The associated δ^{13}C-CH_4 is −55.1 ± 0.71‰. It does not correspond to the typical North Sea gas source signature, which is usually more enriched (Fig. 5). Yet it is also among the highest δ^{13}C values derived from this dataset. This strongly suggests that this pollution event contained a higher proportion of CH_4 from non-biogenic sources on land (because of a southern wind). Event 3 was not elevated enough in the model using TNO-MACC III to allow calculation of the isotope source signatures (selection criteria (see section 2.4) were not fulfilled). Both emission inventories show a higher proportion of wetland emissions, combined with a relatively large fossil fuel contribution in EDGAR v4.3.2. This also caused higher signatures for this event from the model results, but not as much as in the measurements, likely because of the additional contribution of isotopically depleted CH_4 from wetlands. The inventories locate wetlands along the North Sea coast of the Netherlands, but in this case the emissions are not confirmed by the measurements.

In the second subset (10–16 March 2017), four pollution events were recorded, also labelled in Fig. 8. The two events on March 11th (4 & 5) closely follow each other, the second one showing a smaller elevation than the first. The model reproduces well events 4, 6 and 7,

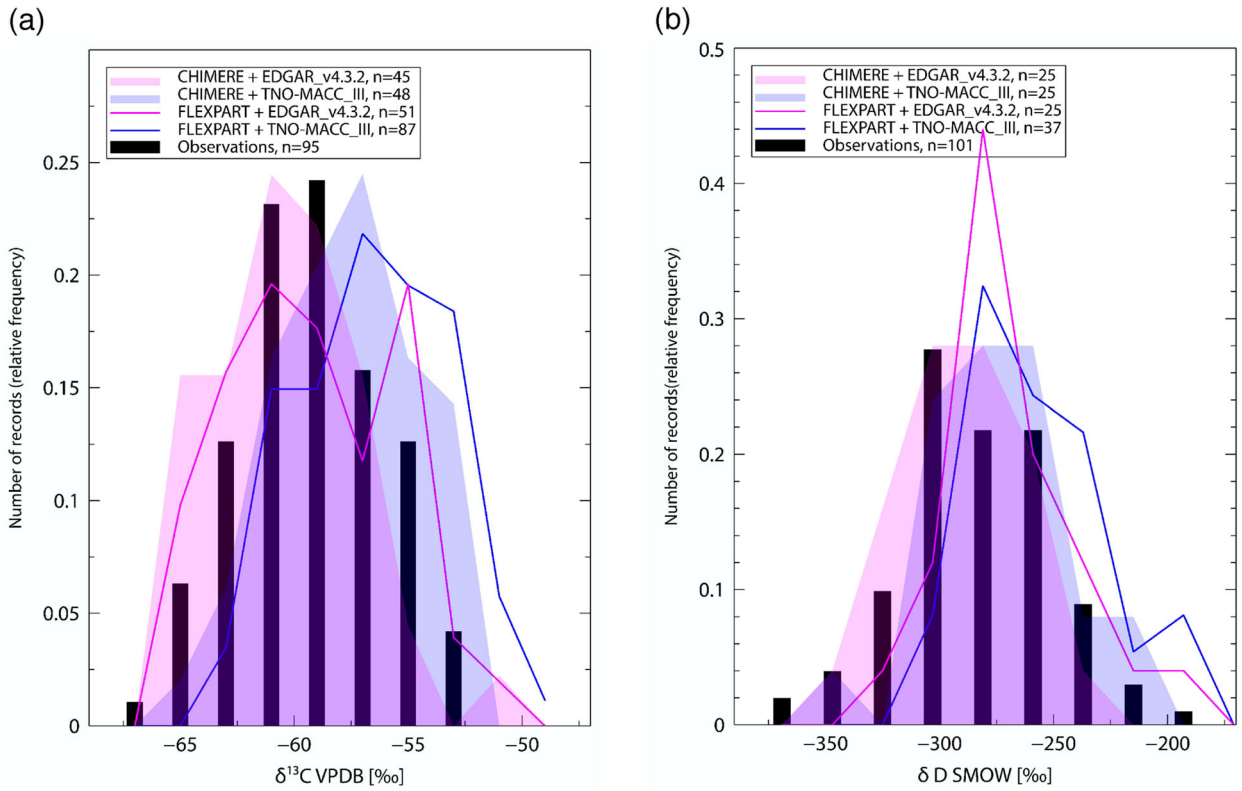

Fig. 6. Frequency distribution of the $\delta^{13}C$ and δD source signatures derived from the moving window Keeling plot approach applied to the observation and modelled time series, interpolated linearly to the measurement times. Signatures from the same peak were averaged to give one value per pollution event.

but shows another pollution event before event 4, which was not measured. Also, the small $\chi(CH_4)$ elevation of event 5 is not present in the model simulations, so no Keeling plot intercept could be derived. Event 4 is associated with a sharp switch in wind direction: from northwest background air to southeast land emissions. It is characterised by a higher contribution from fossil fuel sources, modelled with both TNO-MACC III and EDGAR v4.3.2 inventories. Yet this contribution is overestimated by TNO-MACC III. The corresponding $\delta^{13}C$ and δD signatures are still low, because biogenic emissions are still the prominent source. Even though the wind direction stays at $132 \pm 14°$, the measured isotope source signatures clearly decrease further for event 5. This qualitatively confirms the decrease in the fossil fuel contribution for the model runs using the EDGAR v4.3.2 inventory between these two events. Event 7 (morning of March 14, Fig. 8) was not elevated enough in the model to obtain an isotope source signatures from the Keeling plots. The source partitioning from both inventories still suggests a higher contribution from fossil fuel sources during this event. This is confirmed by the higher δD during event 7 compared to event 6 from the measurements. Yet, the measured $\delta^{13}C$ decreases slightly. This anti-correlation between $\delta^{13}C$ and δD is rarely observed in the time series and cannot be explained with the assignment of fixed isotope signatures used in our evaluation. There is a shift in the wind direction during event 6: from $123 \pm 5°$N to $235 \pm 18°$N. This suggests a change in the pollution source, yet the signatures from the observations remain stable.

4. Discussion & conclusion

4.1. Spatial and temporal variability

There is a seasonal cycle in the background methane mole fractions in the northern hemisphere due to the higher abundance of OH radicals in the summer (Dlugokencky et al., 2011). The dataset presented here was taken over the fall and winter months and is not strongly affected by this annual variability. The background $\chi(CH_4)$ measured at Mace Head were stable over the 5 months of measurements, and were in good agreement with the measured values when the wind was coming from the west.

Diurnal variability is to a large degree driven by the accumulation of compounds from surface emissions during the night, and more vertical mixing during the day.

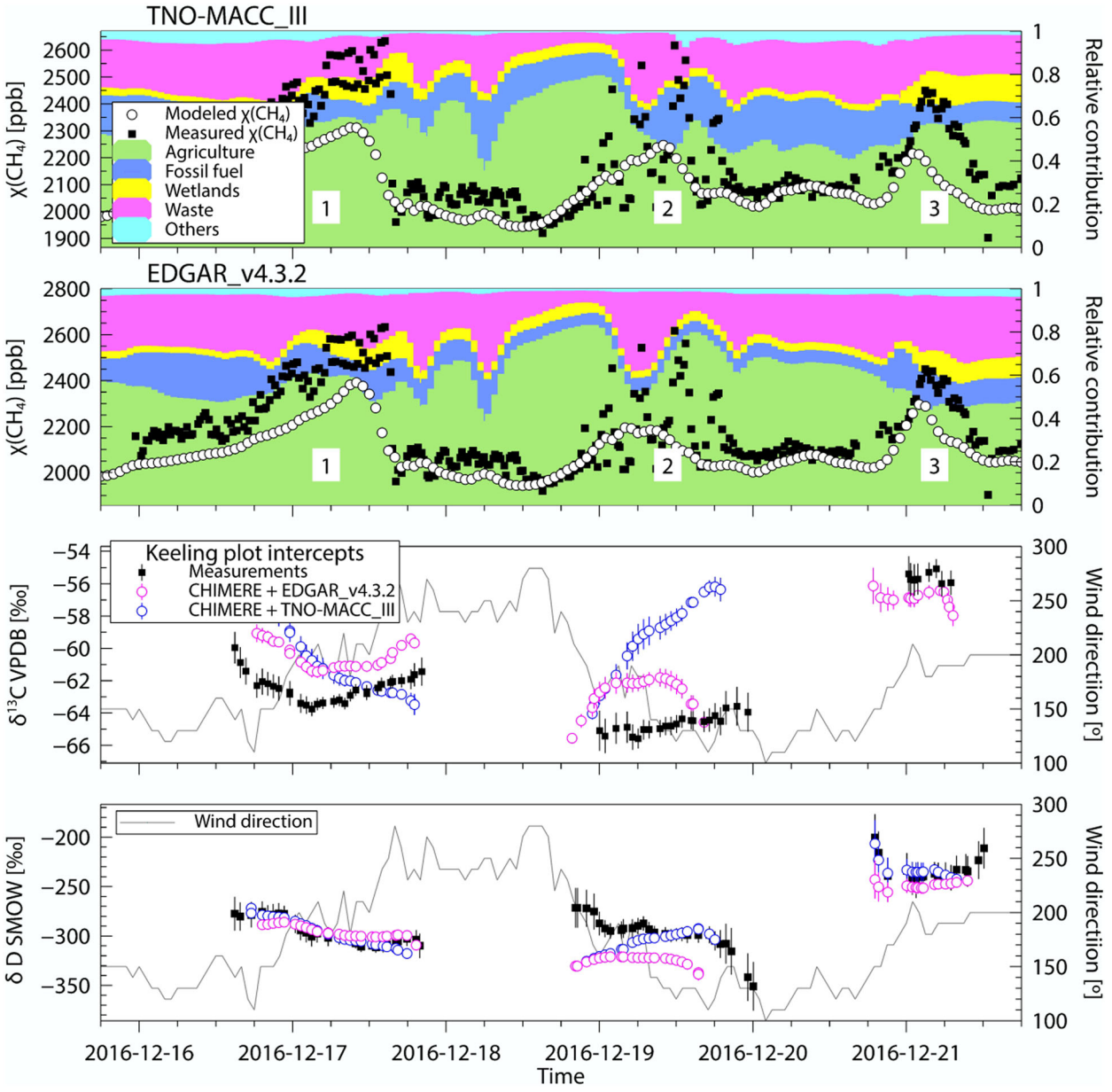

Fig. 7. December 16 to 21 subset. The upper panels show $\chi(CH_4)$ time series with an average time resolution of 51 min for the observations and 1 h for the model (left axis), with the modelled source partitioning (right axis). The lower panels show source signatures resulting from the moving window Keeling plot (left axis) with the recorded wind directions (right axis).

Table 2. Overall contribution from each source type to $\chi(CH_4)$ from CHIMERE, in [%] $\pm 1\sigma$.

Source sector	TNO-MACC III	EDGAR v4.3.2
Agriculture	58.6 ± 12.0	62.3 ± 12.9
Fossil fuels	14.5 ± 7.9	10.7 ± 5.9
Waste	17.9 ± 7.8	19.0 ± 9.6
Wetlands	6.1 ± 3.5	5.7 ± 2.7
Others	3.0 ± 2.5	2.3 ± 1.0

During the two episodes presented in detail in the results section, the highest $\chi(CH_4)$ elevations were recorded in the beginning of the day. The nighttime accumulation is therefore visible in the measurements almost everyday, at least during the winter months.

On March 10, no elevation was recorded: the average $\chi(CH_4)$ was 1954 ± 13 ppb from 00:00 to 22:00, which is close to the the overall background of 1933 ± 11 ppb (section 3.1), and the values observed at Mace Head. This

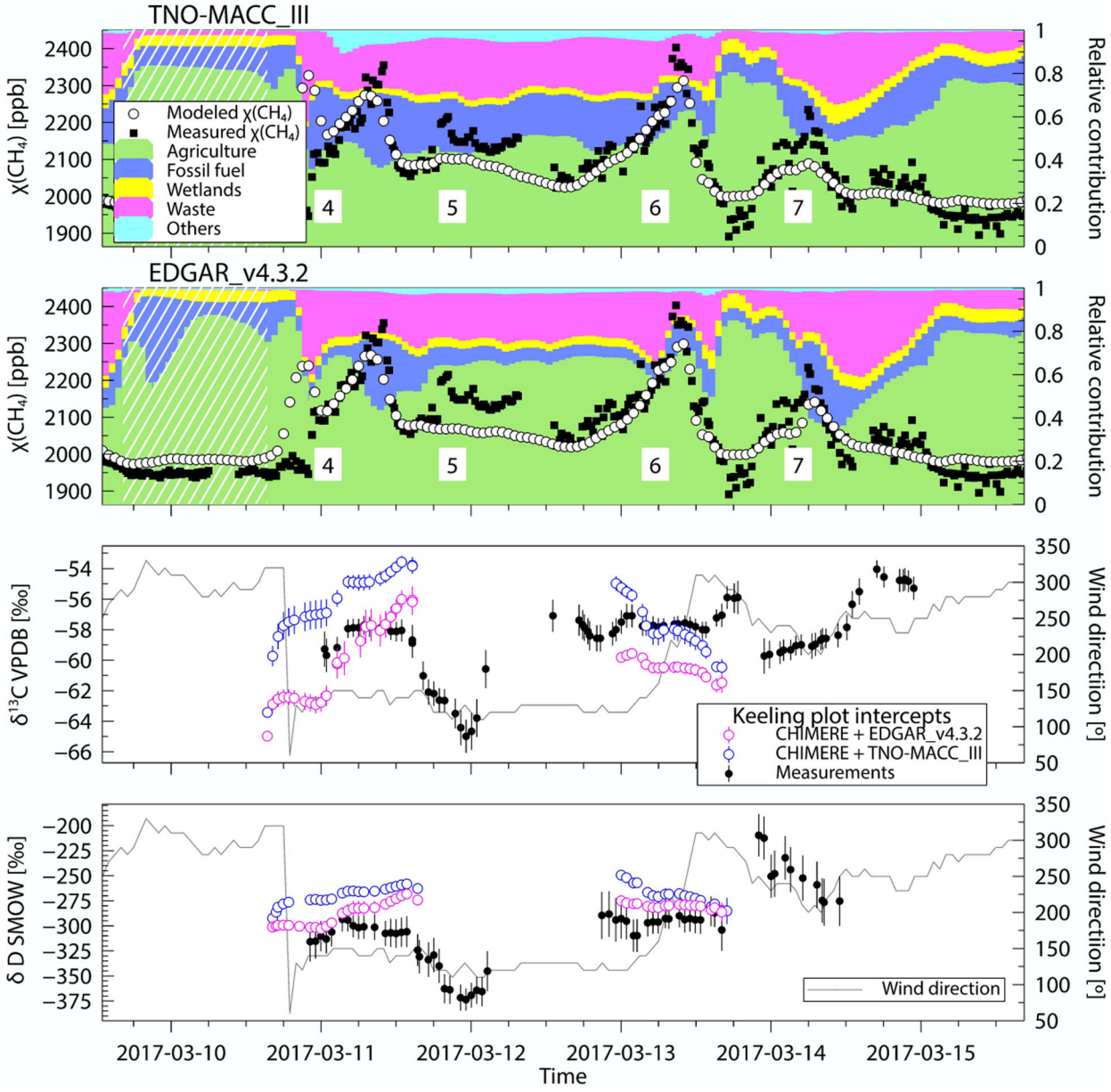

Fig. 8. March 10 to 15 subset. The upper panels show $\chi(CH_4)$ time series with an average time resolution of 51 min for the observations and 1 h for the model (left axis), with the modelled source partitioning (right axis). The lower panels show source signatures resulting from the moving window Keeling plot (left axis) with the recorded wind directions (right axis). The white hatching shows stable background $\chi(CH_4)$ advected by northern winds.

part is highlighted in Fig. 8 (white hatching). The wind in the period March 9, 16:00 to March 10, 18:00 was from west/northwest ($300 \pm 14°$N), bringing background air from the sea. In general, background values in the dataset were mostly advected by winds from 250 to 360°N.

Variations in wind direction on longer time scales also affect the results: southerly to southwesterly winds were prominent in December and January, whereas easterly winds, from 80 to 100°N, almost never occurred. Southwesterly winds advected the highest mole fractions of the dataset (Fig. 3(c,d)), corresponding to important biogenic CH_4 sources. They can be attributed to agriculture (mainly cattle farming), waste management, and to a smaller extent, wetlands (Fig. 7, event 1). Easterly winds did not bring air with very high $\chi(CH_4)$, but some of the elevations were associated with a significantly higher $\delta^{13}C$ (Fig. S5). Emissions from the Groningen gas field can potentially be the cause of this enrichment. Both

Table 3. Comparison of the averaged source signatures obtained from the Cabauw and Lutjewad time series. The values (y-intercept in [‰] $\pm 1\sigma$) are obtained from a weighted orthogonal distance regression (ODR) minimising the sum of squared weighted orthogonal distances of all the data points to the fitted curve.

Averaged source signatures	Cabauw (Röckmann et al., 2016)	Lutjewad (this study)
δ^{13}C vs V-PDB	-60.8 ± 0.2	-59.5 ± 0.1
δD vs V-SMOW	-298 ± 1	-287 ± 1

EDGAR v4.3.2 and TNO-MACC III inventories report large fossil fuel emissions in northwest Germany, which may have also contributed. There is no clear evidence, however, of this higher fossil fuel contribution from the δD results. Fewer δD signatures were obtained from easterly winds. Indeed, the selection criteria for the moving window Keeling plots were rarely fulfilled due to the low CH_4 elevations combined with the higher measurement uncertainties for this isotope signature.

4.2. Source identification

The resulting source isotopic signatures clearly confirms that at Lutjewad station the dominant sources are microbial. This includes emissions from the waste sector, but these source categories are not easy to disentangle since the source isotopic signatures partially overlap (Fig. 5). The emission sources that characterise the area are regional human activities such as cattle farming and waste management. The isotopic analysis gives a consistent interpretation of the methane source contributions, and is confirmed by the modelling exercise.

From November 2014 to March 2015, similar measurements were performed at the Cabauw tall tower site, in central Netherlands (Röckmann et al., 2016). The resulting source signatures derived from the entire datasets are compared in Table 3. Both δ^{13}C- and δD- CH_4 values point towards biogenic emissions, but are significantly different. The reasons might be a slightly larger contribution from enriched sources in the Lutjewad region, such as fossil fuel related emissions from the Groningen gas field and the German Ruhr area. Another possible explanation is that source signatures from biogenic emissions might vary slightly depending on the region. A potential seasonal effect is excluded, as both measurements were performed through the winter.

The presence of off-shore oil and gas platforms in the North Sea, in the northwest direction from Lutjewad did not lead to advection of thermogenic methane that could be detected on the Dutch coast. In contrast, the northwest wind transported mainly background air to our measurement station, and at higher wind speeds, supported by $\chi(CH_4)$ measurements at Mace Head. This is likely due to the large distance between the off-shore platforms and the coast. Yacovitch et al. (2018) suggested a larger contribution of CH_4 venting from off-shore facilities to the total Dutch oil and gas emissions than the one reported in the inventories. However, low emission rates were derived by Riddick et al. (2019), from measurements at 8 oil and gas platforms in the UK. Cain et al. (2017) also detected methane enhancements over UK gas rigs. The broad methane plume detected by Yacovitch et al. (2018) on 1 September 2016 could reasonably come from these installations. Measurements at closer distances from Dutch off-shore platforms, and at different times of the year are therefore required to better detect the isotopic composition of these emissions.

One pollution event with a larger contribution from fossil fuel sources was identified on 21 December 2016 (Fig. 7, event 3), coming from south of Lutjewad. The cause could be the two natural gas storage facilities that are in this direction. The isotopic enrichment was partially confirmed by the CHIMERE results. In the EDGAR v4.3.2 inventory, the fossil fuel emissions increased, but also the wetland contribution, which is characterised by an isotopically depleted CH_4. Wetland sources from the ORCHIDEE-WET model are located both in the central Netherlands and along the North Sea coast from Amsterdam to the North of France. But for this specific event, a larger influence from wetlands is not confirmed by the observations.

The modelled source contributions do not always agree with the isotopic measurements (Figs. 7 and 8). However, uncertainties remain in the range of signatures assigned to one source. The consequences will be discussed in the next section.

4.3. Model performance

The model time series agree well with the observations regarding the timing of the pollution events (Fig. 4). The measurements of $\chi(CH_4)$ show in general higher elevations, and consequently more depleted isotopic signatures. In the model, CH_4 mole fractions are averaged per hour, and therefore are always smoothed compared to measurement data. The time series from FLEXPART-COSMO correlate better with the measured mole fractions than

Table 4. Comparison of the averaged source signatures from measurements and models. They correspond to the Keeling plot intercepts using all data. The values (y-intercept in [‰] ± 1σ) are obtained from a weighted orthogonal distance regression (ODR) minimising the sum of squared weighted orthogonal distances of all the data points to the fitted curve.

	Obervations	CHIMERE	FLEXPART-COSMO	Inventory
δ^{13}C vs V-PDB	−59.5 ± 0.1	−57.2 ± 0.2	−57.2 ± 0.1	EDGAR v4.3.2
		−55.2 ± 0.2	−55.4 ± 0.1	TNO-MACC III
δD vs V-SMOW	−287 ± 1	−266 ± 2	−253 ± 1	EDGAR v4.3.2
		−254 ± 2	−249 ± 2	TNO-MACC III

CHIMERE, which may be explained by its higher horizontal resolution.

Although the results are generally similar when using the two different inventories (Fig. 4), the relative source contributions do change when another inventory is used. The main difference is in the contribution from fossil fuel sources, estimated as 14.5% when using the TNO-MACC III inventory, whereas it is only 10.7% when using the EDGAR v4.3.2 (Table 2). Simulations using the TNO-MACC III inventory overestimate the average source signature by 2 and 12‰ more for δ^{13}C and δD respectively, than simulations with EDGAR v4.3.2 (Table 4, Fig. 6). This is in line with the higher fossil fuel emissions in TNO-MACC III. The average source signature and the ones of individual events from the CHIMERE model results are closer to the observations when using EDGAR v4.3.2 (Table 2, Figs. 7 and 8).

Table 4 shows the average source signatures resulting from the Keeling plot of the entire dataset. The source signatures are overestimated when using both models, with both inventories. The best agreement for the average source signatures is with the CHIMERE results using the EDGAR v4.3.2 inventory. Wetland CH_4 emissions were not taken into account in FLEXPART-COSMO, which explains the relative enrichment in δ^{13}C compared to the CHIMERE results. If the wetland emissions are neglected in CHIMERE, the average source signature would change by +0.7 and +7‰ respectively for δ^{13}C and δD. Taking these emissions into account could significantly improve the agreement between the results from FLEXPART-COSMO and the observations.

The input isotopic signatures for the model are based on previous measurements reported in the literature. In the case of δ^{13}C, the numerous measurements reported for North Sea gas (Hitchman, S. P. 1989; Zazzeri et al., 2015; Cain et al., 2017; Riddick et al., 2019) allowed to adapt the fossil fuel emission source signature to the study location. A value of −40‰ was chosen for this category. Initial model calculations used with the original fossil fuel δ^{13}C of −47‰ as input to CHIMERE and FLEXPART-COSMO. The variability in the δ^{13}C observations was then not well reproduced by the model results, and the overall source signature was underestimated. Another test using a value of −33‰ was made with CHIMERE to represent only the most enriched North Sea gas emissions, and resulted in an overestimation of δ^{13}C compared to the measurements. This confirms the geographical dependency in the isotopic signature of fossil fuel CH_4 emissions.

Further sensitivity studies were performed to evaluate the origin of the mismatch in the average isotopic signature between observations and model. Only changes in the agriculture, waste and fossil fuel source signatures have a significant effect on the average, because they represent the largest shares of emissions. Regarding the fossil fuel signature, it is well constrained by previous measurements, as described in the previous paragraph. In order to match the observed overall Keeling plot intercept, δ^{13}C and δD source signatures in the CHIMERE model using EDGAR v4.3.2 emissions would need to be lowered to −72 and −349‰ for agriculture and −58 and −313‰ for waste, respectively. Using the TNO-MACC III inventory would imply even lower values for agriculture and waste. Within these categories, such depleted isotope signatures are not fully excluded, but highly unlikely based on values published in the literature. It is therefore unlikely that the differences can be attributed only to uncertainties in the assigned isotope signatures. Thus, our semi-continuous isotope measurements provide evidence for lower contributions from fossil sources compared to what is included in the inventories. A more comprehensive evaluation of source contributions using the same parametrisation of CHIMERE is currently in preparation (by B. Szénási).

Röckmann et al. (2016) assessed that fossil fuel related emissions were likely overestimated in the previous version of EDGAR v4.2 and these emissions have been significantly reduced in version EDGAR v4.3.2 used for this study. The results presented here demonstrate that this adjustment in the fossil fuel contribution leads to better agreement with the isotope measurements. However, the source partitioning in the inventory likely needs to be adjusted further.

4.4. Future investigations

Reported source signatures in the literature are much less numerous for δD-CH_4 than $\delta^{13}C$, and the input δD-CH_4 values for the different sources in the models are more uncertain. In this study, we observed a correlation between $\delta^{13}C$ and δD signatures, with a $\delta^{13}C$: δD slope of about 10 ‰/‰. However, this situation is specific to the Netherlands, as the thermogenic sources are particularly enriched (Fig. 5). In regions where fossil sources have lower $\delta^{13}C$ values than in the Netherlands, measurements of δD-CH_4 become crucial for source attribution. In general, more measurements of $\delta^{13}C$ and δD-CH_4 from the various sources would be valuable to better constrain the isotopic signatures used as input to the models, i.e. by taking into account potential seasonal and geographical variations within source categories.

The combination of isotope measurements with model data is particularly valuable for assessing the accuracy of emission inventories. In our study, the average isotopic signatures do not precisely match the measurements, but still confirm the predominance of biogenic emissions, which is expected in the Netherlands. The source contributions obtained from the CHIMERE model show that for some pollution events the modelled source attribution is supported by the measured isotope changes, but for others not. This demonstrates the power of the high temporal resolution isotope time series that can be obtained with an IRMS system operating at various locations. In the future, measurements of high-frequency $\delta^{13}C$ and δD at several locations and other countries, would better constrain the emissions on a larger scale. Current challenges lie in the technical complexity of the measurements and high quality logistics required to perform these measurements. They are the limiting factors for conducting similar studies in more remote and under-studied regions.

Data availability statement

The data that support the findings of this study are openly available in mamenoud/CH4-Lutjewad-2016-2017: First release (Version v1.0.0) at http://doi.org/10.5281/zenodo.3970888.

Disclosure statement

No potential conflict of interest was reported by the authors.

Supplemental data

Supplemental data for this article can be accessed **here**

Acknowledgements

We specially thank Bert Kers and Marcel de Vries at CIO for the technical support they provided during the measurements at Lutjewad.

Funding

This work was supported by the ITN project Methane goes Mobile – Measurements and Modelling ($MEMO^2$; https://h2020-memo2.eu/). This project has received funding from the European Union's Horizon 2020 research and innovation programme under the Marie Sklodowska-Curie grant agreement No 722479. AGAGE is supported principally by NASA (USA) grants to MIT and SIO, and also by: BEIS (UK) and NOAA (USA) grants to Bristol University; CSIRO and BoM (Australia): FOEN grants to Empa (Switzerland); NILU (Norway); SNU (Korea); CMA (China); NIES (Japan); and Urbino University (Italy).

References

Baldauf, M., Seifert, A., Förstner, J., Majewski, D., Raschendorfer, M. and co-authors. 2011. Operational convective-scale numerical weather prediction with the COSMO model: description and sensitivities. *Mon. Weather Rev. 139*, 3887–3905. doi:10.1175/MWR-D-10-05013.1

Beck, V., Chen, H., Gerbig, C., Bergamaschi, P., Bruhwiler, L. and co-authors. 2012. Methane airborne measurements and comparison to global models during BARCA: methane in the Amazon during BARCA. *J. Geophys. Res. 117*, 15310. doi:10.1029/2011JD017345

Bergamaschi, P., Frankenberg, C., Meirink, J. F., Krol, M., Villani, M. G. and co-authors. 2009. Inverse modeling of global and regional CH_4 emissions using SCIAMACHY satellite retrievals. *J. Geophys. Res. 114*, 301.

Bergamaschi, P., Lubina, C., Königstedt, R., Fischer, H., Veltkamp, A. C. and co-authors. 1998. Stable isotopic signatures (^{13}C,D) of methane from European landfill sites. *J. Geophys. Res. 103*, 8251–8265. doi:10.1029/98JD00105

Bergamaschi, P., Karstens, U., Manning, A. J., Saunois, M., Tsuruta, A. and co-authors. 2018. Inverse modelling of European CH_4 emissions during 2006–2012 using different inverse models and reassessed atmospheric observations. *Atmos. Chem. Phys. 18*, 901–920. doi:10.5194/acp-18-901-2018

Bilek, R. S., Tyler, S. C., Kurihara, M. and Yagi, K. 2001. Investigation of cattle methane production and emission over a 24-hour period using measurements of ^{13}C and D of emitted CH_4 and rumen water. *J. Geophys. Res. 106*, 15405–15413. doi:10.1029/2001JD900177

Borsdorff, T., Brugh, J., Aan de, Pandey, S., Hasekamp, O., Aben, I. and co-authors. 2019. Carbon monoxide air pollution on sub-city scales and along arterial roads detected

by the Tropospheric Monitoring Instrument. *Atmos. Chem. Phys. 19*, 3579–3588. doi:10.5194/acp-19-3579-2019

Bousquet, P., Ciais, P., Miller, J. B., Dlugokencky, E. J., Hauglustaine, D. A. and co-authors. 2006. Contribution of anthropogenic and natural sources to atmospheric methane variability. *Nature 443*, 439–443. doi:10.1038/nature05132

Bréas, O., Guillou, C., Reniero, F. and Wada, E. 2001. The global methane cycle: isotopes and mixing ratios, sources and sinks. *Isotopes Environ. Health Stud. 37*, 257–379. doi:10.1080/10256010108033302

Cain, M., Warwick, N. J., Fisher, R. E., Lowry, D., Lanoisellé, M. and co-authors. 2017. A cautionary tale: a study of a methane enhancement over the North Sea. *J. Geophys. Res. Atmos. 122*, 7630–7645. doi:10.1002/2017JD026626

Chanton, J. P., Rutkowski, C. M., Schwartz, C. C., Ward, D. E. and Boring, L. 2000. Factors influencing the stable carbon isotopic signature of methane from combustion and biomass burning. *J. Geophys. Res. 105*, 1867–1877. doi:10.1029/1999JD900909

Chen, H., Winderlich, J., Gerbig, C., Hoefer, A., Rella, C. W. and co-authors. 2010. High-accuracy continuous airborne measurements of greenhouse gases (CO_2 and $CH_{4)}$ using the cavity ring-down spectroscopy (CRDS) technique. *Atmos. Meas. Tech. 3*, 375–386. doi:10.5194/amt-3-375-2010

Dlugockenky, E. J., Crotwell, A. M., Mund, J. W., Crotwell, M. J. and Thoning, K. W. 2019. Atmospheric methane dry air mole fractions from the NOAA ESRL carbon cycle cooperative global air sampling network, 1983-2018, Version: 2019-07. Online at: https://www.esrl.noaa.gov/gmd/dv/data/index.php?category=Greenhouse

Dlugokencky, E. J., Nisbet, E. G., Fisher, R. and Lowry, D. 2011. Global atmospheric methane: budget, changes and dangers. *Philos. Trans. A Math. Phys. Eng. Sci. 369*, 2058–2072.

EEA (European Environment Agency). 2000. *EMEP/CORINAIR atmospheric emission inventory guidebook - Second edition 1999*. Output from Annual Management Plan. Online at: https://www.eea.europa.eu/publications/EMEPCORINAIR

European Union. 1995. *Eurostat*. European Commission website. Online at: https://ec.europa.eu/eurostat/statistical-atlas/gis/viewer/?

Eyer, S., Tuzson, B., Popa, M. E., van der Veen, C., Röckmann, T. and co-authors. 2016. Real-time analysis of ^{13}C- and D-CH_4 in ambient air with laser spectroscopy: method development and first intercomparison results. *Atmos. Meas. Tech. 9*, 263–280. doi:10.5194/amt-9-263-2016

Fortems-Cheiney, A., Pison, I., Dufour, G., Broquet, G., Berchet, A. and co-authors. 2019. *Variational regional inverse modeling of reactive species emissions with PYVAR-CHIMERE*. Preprint. *Atmos. Sci*. Online at: https://www.geosci-model-dev-discuss.net/gmd-2019-186/

Galand, P. E., Yrjälä, K. and Conrad, R. 2010. Stable carbon isotope fractionation during methanogenesis in three boreal peatland ecosystems. *Biogeosciences 7*, 3893–3900. doi:10.5194/bg-7-3893-2010

Games, L. M. and Hayes, J. M. 1976. On the mechanisms of CO_2 and CH_4 production in natural anaerobic environments. *Environ. Biogeochem. 1*, 51–73.

Happell, J. D., Chanton, J. P. and Showers, W. J. 1995. Methane transfer across the water-air interface in stagnant wooded swamps of Florida: evaluation of mass-transfer coefficients and isotropic fractionation. *Limnol. Oceanogr. 40*, 290–298. doi:10.4319/lo.1995.40.2.0290

Henne, S., Brunner, D., Oney, B., Leuenberger, M., Eugster, W. and co-authors. 2016. Validation of the Swiss methane emission inventory by atmospheric observations and inverse modelling. *Atmos. Chem. Phys. 16*, 3683–3710. doi:10.5194/acp-16-3683-2016

Hitchman, S.P., 1989. Stable isotope ratios in methane containing gasess in the United Kingdom. Technical Report WE/89/30. British Geological Survey.

Hitchman, S. P., 1989. Stable Isotope Ratios in Methane Containing Gasess in the United Kingdom. Technical Report WE/89/30. British Geological Survey.

Hourdin, F., Musat, I., Bony, S., Braconnot, P., Codron, F. and co-authors. 2006. The LMDZ4 general circulation model: climate performance and sensitivity to parametrized physics with emphasis on tropical convection. *Clim. Dyn. 27*, 787–813. doi:10.1007/s00382-006-0158-0

Houweling, S., Krol, M., Bergamaschi, P., Frankenberg, C., Dlugokencky, E. J. and co-authors. 2014. A multi-year methane inversion using SCIAMACHY, accounting for systematic errors using TCCON measurements. *Atmos. Chem. Phys. 14*, 3991–4012. doi:10.5194/acp-14-3991-2014

Hu, H., Landgraf, J., Detmers, R., Borsdorff, T., Brugh, J. and co-authors. 2018. Toward global mapping of methane with TROPOMI: first results and intersatellite comparison to GOSAT. *Geophys. Res. Lett. 45*, 3682–3689. doi:10.1002/2018GL077259

IPCC 2013. *Climate Change 2013: The Physical Science Basis; Working Group I Contribution to the Fifth Assessment Report of the Intergovernmental Panel on Climate Change* (OCLC: 871571414). Cambridge University Press, Cambridge, UK.

Jacob, D. J., Turner, A. J., Maasakkers, J. D., Sheng, J., Sun, K. and co-authors. 2016. Satellite observations of atmospheric methane and their value for quantifying methane emissions. *Atmos. Chem. Phys. 16*, 14371–14396. doi:10.5194/acp-16-14371-2016

Janssens-Maenhout, G., Crippa, M., Guizzardi, D., Muntean, M., Schaaf, E. and co-authors. 2019. EDGAR v4.3.2 global atlas of the three major greenhousegas emissions for the period 1970-2012. *Earth Syst. Sci. Data* 11.3, 959–1002. doi:10.5194/essd-11-959-2019

Keeling, C. D. 1961. The concentration and isotopic abundances of carbon dioxide in rural and marine air. *Geochim. Cosmochim. Acta. 24*, 277–298. doi:10.1016/0016-7037(61)90023-0

Kirschke, S., Bousquet, P., Ciais, P., Saunois, M., Canadell, J. G. and co-authors. 2013. Three decades of global methane sources and sinks. *Nat. Geosci. 6*, 813–823. doi:10.1038/ngeo1955

Klevenhusen, F., Bernasconi, S. M., Kreuzer, M. and Soliva, C. R. 2010. Experimental validation of the Intergovernmental Panel on Climate Change default values for ruminant-derived methane and its carbon-isotope signature. *Anim. Prod. Sci. 50*, 159. doi:10.1071/AN09112

Kuenen, J. J. P., Visschedijk, A. J. H., Jozwicka, M., Gon, H. A. C. and Denier van der, 2014. TNO-MACC_ii emission inventory; a multi-year (2003-2009) consistent high-resolution European emission inventory for air quality modelling. *Atmos. Chem. Phys 14*, 10963–10976. doi:10.5194/acp-14-10963-2014

Levin, I., Bergamaschi, P., Dörr, H. and Trapp, D. 1993. Stable isotopic signature of methane from major sources in Germany. *Chemosphere 26*, 161–177. doi:10.1016/0045-6535(93)90419-6

Levin, I., Glatzel-Mattheier, H., Marik, T., Cuntz, M., Schmidt, M. and co-authors. 1999. Verification of German methane emission inventories and their recent changes based on atmospheric observations. *J. Geophys. Res. 104*, 3447–3456. doi:10.1029/1998JD100064

Lowry, D., Holmes, C. W., Rata, N. D., O'Brien, P. and Nisbet, E. G. 2001. London methane emissions: use of diurnal changes in concentration and d^{13} C to identify urban sources and verify inventories. *J. Geophys. Res. 106*, 7427–7448. doi:10.1029/2000JD900601

Mailler, S., Menut, L., Khvorostyanov, D., Valari, M., Couvidat, F. and co-authors. 2017. CHIMERE-2017: from urban to hemispheric chemistry-transport modeling. *Geosci. Model Dev. 10*, 2397–2423. doi:10.5194/gmd-10-2397-2017

Marécal, V., Peuch, V.-H., Andersson, C., Andersson, S., Arteta, J. and co-authors. 2015. A regional air quality forecasting system over Europe: the MACC-II daily ensemble production. *Geosci. Model Dev.* **8**, 2777–2813. doi:10.5194/gmd-8-2777-2015

Martens, C. S., Kelley, C. A., Chanton, J. P. and Showers, W. J. 1992. Carbon and hydrogen isotopic characterization of methane from wetlands and lakes of the Yukon-Kuskokwim delta, western Alaska. *J. Geophys. Res. 97*, 16689. doi:10.1029/91JD02885

Menut, L., Bessagnet, B., Khvorostyanov, D., Beekmann, M., Blond, N. and co-authors. 2013. CHIMERE 2013: a model for regional atmospheric composition modelling. *Geosci. Model Dev. 6*, 981–1028. doi:10.5194/gmd-6-981-2013

Ministerie van Economische Zaken, TNO. 2018. *Overview of all boreholes.* Online at: https://www.nlog.nl/en/map-boreholes

Monteil, G., Houweling, S., Butz, A., Guerlet, S., Schepers, D. and co-authors. 2013. Comparison of CH_4 inversions based on 15 months of GOSAT and SCIAMACHY observations: INVERSE MODELING OF SATELLITE RETRIEVED *X* CH_4. *J. Geophys. Res. Atmos. 118*, 11,807–11,823. doi:10.1002/2013JD019760

Monteil, G., Houweling, S., Dlugockenky, E. J., Maenhout, G., Vaughn, B. H. and co-authors. 2011. Interpreting methane variations in the past two decades using measurements of CH_4 mixing ratio and isotopic composition. *Atmos. Chem. Phys. 11*, 9141–9153. doi:10.5194/acp-11-9141-2011

Nakagawa, F., Tsunogai, U., Komatsu, D. D., Yamada, K., Yoshida, N. and co-authors. 2005. Automobile exhaust as a source of ^{13} C- and D-enriched atmospheric methane in urban areas. *Org. Geochem. 36*, 727–738. doi:10.1016/j.orggeochem.2005.01.003

Nisbet, E. G., Manning, M. R., Dlugokencky, E. J., Fisher, R. E., Lowry, D. and co-authors. 2019. Very strong atmospheric methane growth in the 4 years 2014–2017: implications for the Paris agreement. *Global Biogeochem. Cycles 33*, 318–342. doi:10.1029/2018GB006009

OSPAR Commission. 2015. *2015 Update of the Inventory of Oil and Gas Offshore Installations in the OSPAR Maritime Area*. OSPAR Commission, Offshore Industry Series. London, UK.

Pandey, S., Houweling, S., Krol, M., Aben, I., Monteil, G. and co-authors. 2017. Enhanced methane emissions from tropical wetlands during the 2011 La Niña. *Sci. Rep. 7*, 45759. doi:10.1038/srep45759

Pandey, S., Houweling, S., Krol, M., Aben, I., Nechita–Banda, N. and co-authors. 2019. Influence of atmospheric transport on estimates of variability in the global methane burden. *Geophys. Res. Lett. 46*, 2302–2311. doi:10.1029/2018GL081092

Pataki, D. E., Ehleringer, J. R., Flanagan, L. B., Yakir, D., Bowling, D. R. and co-authors. 2003. The application and interpretation of Keeling plots in terrestrial carbon cycle research: application of Keeling plots. *Global Biogeochem. Cycles 17*, 1022. doi:10.1029/2001GB001850.

Pisso, I., Sollum, E., Grythe, H., Kristiansen, N., Cassiani, M. and co-authors. 2019. The Lagrangian particle dispersion model FLEXPART version 10.3. *Geosci. Model Dev. Discuss.* 1–67. Retrieved from https://www.geosci-model-dev-discuss.net/gmd-2018-333/

Prinn, R., Weiss, R., Krummel, P., O'Doherty, S. and Muhle, J. 2008. *The ALE/GAGE/AGAGE Network (DB1001)*. Environmental System Science Data Infrastructure for a Virtual Ecosystem; Carbon Dioxide Information Analysis Center (CDIAC), Oak Ridge National Laboratory (ORNL), Oak Ridge, TN.

Rella, C. W., Chen, H., Andrews, A. E., Filges, A., Gerbig, C. and co-authors. 2013. High accuracy measurements of dry mole fractions of carbon dioxide and methane in humid air. *Atmos. Meas. Tech. 6*, 837–860. doi:10.5194/amt-6-837-2013

Riddick, S. N., Mauzerall, D. L., Celia, M., Harris, N. R. P., Allen, G. and co-authors. 2019. Measuring methane emissions from oil and gas platforms in the North Sea. *Atmos. Chem. Phys. Discuss. 19*, 9787–9796. doi:10.5194/acp-2019-90

Rigby, M., Manning, A. J. and Prinn, R. G. 2012. The value of high-frequency high-precision methane isotopologue measurements for source and sink estimation: methane isotopologues in inversions. *J. Geophys. Res. 117,* D12312, 1–14. doi:10.1029/2011JD017384

Ringeval, B., Friedlingstein, P., Koven, C., Ciais, P., de Noblet-Ducoudré, N. and co-authors. 2011. Climate-CH_4 feedback from wetlands and its interaction with the climate-CO_2 feedback. *Biogeosciences 8*, 2137–2157. doi:10.5194/bg-8-2137-2011

Röckmann, T., Eyer, S., Veen, C., van der, Popa, M. E., Tuzson, B. and co-authors. 2016. In situ observations of the

isotopic composition of methane at the Cabauw tall tower site. *Atmos. Chem. Phys. 16*, 10469–10487. doi:10.5194/acp-16-10469-2016

Santoni, G. W., Lee, B. H., Goodrich, J. P., Varner, R. K., Crill, P. M. and co-authors. 2012. Mass fluxes and isofluxes of methane (CH_4) at a New Hampshire fen measured by a continuous wave quantum cascade laser spectrometer: methane isofluxes at a New Hampshire fen. *J. Geophys. Res. 117*, 1–15. Retrieved from http://doi.wiley.com/10.1029/2011JD016960

Saunois, M., Bousquet, P., Poulter, B., Peregon, A., Ciais, P. and co-authors. 2016. The global methane budget 2000–2012. *Earth Syst. Sci. Data 8*, 697–751. doi:10.5194/essd-8-697-2016

Schaefer, H., Fletcher, S. E. M., Veidt, C., Lassey, K. R., Brailsford, G. W. and co-authors. 2016. A 21st-century shift from fossil-fuel to biogenic methane emissions indicated by ^{13}CH□. *Science 352*, 80–84. doi:10.1126/science.aad2705

Seibert, P. and Frank, A. 2004. Source-receptor matrix calculation with a Lagrangian particle dispersion model in backward mode. *Atmos. Chem. Phys. 4*, 51–63. doi:10.5194/acp-4-51-2004

Smith, L. K., Lewis, W. M., Jr., Chanton, J. P., Cronin, G. and Hamilton, S. K. 2000. Methane emissions from the Orinoco River floodplain, Venezuela. *Biogeochemistry 51*, 113–140. doi:10.1023/A:1006443429909

Sperlich, P., Uitslag, N. A. M., Richter, J. M., Rothe, M., Geilmann, H. and co-authors. 2016. Development and evaluation of a suite of isotope reference gases for methane in air. *Atmos. Meas. Tech. 9*, 3717–3737. doi:10.5194/amt-9-3717-2016

Stortplaatsen in Nederland. 2019. Online at: https://www.bodemplus.nl/onderwerpen/bodem-ondergrond/verwerking-grond/stortplaatsen/stortplaatsen/

Sugimoto, A. and Fujita, N. 2006. Hydrogen concentration and stable isotopic composition of methane in bubble gas observed in a natural wetland. *Biogeochemistry 81*, 33–44. doi:10.1007/s10533-006-9028-4

Szénási, B. 2019. *Forward modelling simulations of CH_4 and isotopologues* (Deliverable 3.3). Online at: https://h2020-memo2.eu/wp-content/uploads/sites/198/2019/09/Deliverable_D3_3_final_version-SW.pdf

Tarasova, O., Brenninkmeijer, C., Assonov, S., Elansky, N., Rockmann, T. and co-authors. 2006. Atmospheric CH4 along the Trans-Siberian railroad (TROICA) and river Ob: source identification using stable isotope analysis. *Atmos. Environ. 40*, 5617–5628. doi:10.1016/j.atmosenv.2006.04.065

Thanwerdas, J., Saunois, M., Berchet, A., Pison, I., Hauglustaine, D. and co-authors. 2019. Impact of atomic chlorine on the modelling of total methane and its ^{13}C:^{12}C isotopic ratio at global scale. *Atmos. Chem. Phys. Discuss.* In review. doi:10.5194/acp-2019-925

Thielemann, T., Cramer, B. and Schippers, A. 2004. Coalbed methane in the Ruhr Basin, Germany: a renewable energy resource? *Org. Geochem. 35*, 1537–1549. doi:10.1016/S0146-6380(04)00120-2

Townsend-Small, A., Botner, E. C., Jimenez, K. L., Schroeder, J. R., Blake, N. J. and co-authors. 2016. Using stable isotopes of hydrogen to quantify biogenic and thermogenic atmospheric methane sources: a case study from the Colorado Front Range: hydrogen isotopes in the Front Range. *Geophys. Res. Lett. 43*, 11,462–11,471. doi:10.1002/2016GL071438

Turner, A. J., Frankenberg, C. and Kort, E. A. 2019. Interpreting contemporary trends in atmospheric methane. *Proc Natl Acad Sci USA 116*, 2805–2813. doi:10.1073/pnas.1814297116

Tyler, S. C., Bilek, R. S., Sass, R. L. and Fisher, F. M. 1997. Methane oxidation and pathways of production in a Texas paddy field deduced from measurements of flux, d^{13} C, and dD of CH_4. *Global Biogeochem. Cycles 11*, 323–348. doi:10.1029/97GB01624

Tyler, S. C., Blake, D. R. and Rowland, F. S. 1987. $^{13}C/^{12}$ C ratio in methane from the flooded Amazon forest. *J. Geophys. Res. 92*, 1044. doi:10.1029/JD092iD01p01044

Umezawa, T., Brenninkmeijer, C. A. M., Röckmann, T., Veen, C., van der, Tyler, S. C. and co-authors. 2018. Interlaboratory comparison of ^{13} C and D measurements of atmospheric CH_4 for combined use of data sets from different laboratories. *Atmos. Meas. Tech. 11*, 1207–1231. doi:10.5194/amt-11-1207-2018

Uzaki, M., Mizutani, H. and Wada, E. 1991. Carbon isotope composition of CH_4 from rice paddies in Japan. *Biogeochemistry 13*, 159–175.

Vlek, C. 2018. Induced earthquakes from long-term gas extraction in Groningen, the Netherlands: statistical analysis and prognosis for acceptable-risk regulation: induced earthquakes from long-term gas extraction in Groningen. *Risk Anal. 38*, 1455–1473. doi:10.1111/risa.12967

Wageningen University & Research. 2015. *Landelijk Grondgebruik Nederland - LGN7_BRP2015.* Online at: https://www.wur.nl/nl/Onderzoek-Resultaten/Onderzoeksinstituten/Environmental-Research/Faciliteiten-Producten/Kaarten-en-GIS-bestanden/Landelijk-Grondgebruik-Nederland/lgn_viewer.htm

Werner, R. A. and Brand, W. A. 2001. Referencing strategies and techniques in stable isotope ratio analysis. *Rapid Commun. Mass Spectrom. 15*, 501–519. doi:10.1002/rcm.258

Worden, J. R., Bloom, A. A., Pandey, S., Jiang, Z., Worden, H. M. and co-authors. 2017. Reduced biomass burning emissions reconcile conflicting estimates of the post-2006 atmospheric methane budget. *Nat. Commun. 8*, 2227. doi:10.1038/s41467-017-02246-0

World Meteorological Orgnaization (WMO). 2019. *WMO greenhouse gas bulletin (GHG Bulletin) - No. 15: The state of greenhouse gases in the atmosphere based on global observations through 2018*. Tech. Rep. Global Atmospheric Watch. Online at: https://library.wmo.int/doc_num.php?explnum_id=10100

Yacovitch, T. I., Neininger, B., Herndon, S. C., Gon, H. D., Van der, Jonkers, S. and co-authors. 2018. Methane emissions in the Netherlands: the Groningen field. *Elem. Sci. Anth. 6*, 57. doi:10.1525/elementa.308

Zazzeri, G., Lowry, D., Fisher, R., France, J., Lanoisellé, M. and co-authors. 2015. Plume mapping and isotopic

characterisation of anthropogenic methane sources. *Atmos. Environ. 110*, 151–162. doi:10.1016/j.atmosenv.2015.03.029

Zazzeri, G., Lowry, D., Fisher, R. E., France, J. L., Lanoisellé, M. and co-authors. 2016. Carbon isotopic signature of coal-derived methane emissions to the atmosphere: from coalification to alteration. *Atmos. Chem. Phys. 16*, 13669–13680. doi:10.5194/acp-16-13669-2016

Zazzeri, G., Lowry, D., Fisher, R. E., France, J. L., Lanoisellé, M. and co-authors. 2017. Evaluating methane inventories by isotopic analysis in the London region. *Sci. Rep. 7*, 4854. doi:10.1038/s41598-017-04802-6

Methane (CH_4) sources in Krakow, Poland: insights from isotope analysis

Malika Menoud[1], Carina van der Veen[1], Jaroslaw Necki[2], Jakub Bartyzel[2], Barbara Szénási[3], Mila Stanisavljević[2], Isabelle Pison[3], Philippe Bousquet[3], and Thomas Röckmann[1]

[1]Institute for Marine and Atmospheric research Utrecht (IMAU), Utrecht University, Utrecht, The Netherlands
[2]Faculty of Physics and Applied Computer Science, AGH University of Science and Technology, Kraków, Poland
[3]Laboratoire des sciences du climat et de l'environnement (LSCE), Université Paris-Saclay, CEA, CNRS, UVSQ, Gif-sur-Yvette, France

Correspondence: Malika Menoud (m.menoud@uu.nl)

Abstract. Methane (CH_4) emissions from human activities are a threat to the resilience of our current climate system, and to the adherence of the Paris Agreement goals. The stable isotopic composition of methane (δ^{13}C and δ^{2}H) allows to distinguish between the different CH_4 origins. A significant part of the European CH_4 emissions, 3.6 % in 2018, comes from coal extraction in Poland; the Upper Silesian Coal Basin (USCB) being the main hotspot.

Measurements of CH_4 mole fraction ($\chi(CH_4)$), δ^{13}C and δ^{2}H in CH_4 in ambient air were performed continuously during 6 months in 2018 and 2019 at Krakow, Poland, 50 km east of the USCB. In addition, air samples were collected during parallel mobile campaigns, from multiple CH_4 sources in the footprint area of the continuous measurements. The resulting isotopic signatures from sampled plumes allowed us to distinguish between natural gas leaks, coal mine fugitive emissions, landfill and sewage, and ruminants. The use of δ^{2}H in CH_4 is crucial to distinguish the fossil fuel emissions in the case of Krakow, because their relatively depleted δ^{13}C values overlap with the ones of microbial sources. The observed $\chi(CH_4)$ time series showed regular daily night-time accumulations, sometimes combined with irregular pollution events during the day. The isotopic signatures of each peak were obtained using the Keeling plot method, and generally fall in the range of thermogenic CH_4 formation - with δ^{13}C between -55.3 and -39.4 ‰ V-PDB, and δ^{2}H between -285 and -124 ‰ V-SMOW. They compare well with the signatures measured for gas leaks in Krakow and USCB mines.

The CHIMERE transport model was used to compute the CH_4 and isotopic composition time series in Krakow, based on two emission inventories. The $\chi(CH_4)$ are generally under-estimated in the model. The simulated isotopic source signatures, obtained with Keeling plots on each simulated peak using the EDGAR v5.0 inventory, indicate that a higher contribution from fuel combustion sources in EDGAR would lead to a better agreement. The isotopic mismatches between model and observations are mainly caused by uncertainties in the assigned isotopic signatures for each source category, and the way they are classified in the inventory. These uncertainties are larger for emissions close to the study site, which are more heterogenous than the ones advected from the USCB coal mines. Our isotope approach proves to be very sensitive in this region, thus helping to evaluate emission estimates.

1 Introduction

The emissions of greenhouse gases from human activities are the main cause of the current warming of our Earth's climate. It is urgent to decrease these emissions in order to minimise the negative consequences (IPCC (2018)). The second most important anthropogenic greenhouse gas after carbon dioxide (CO_2) is methane (CH_4; IPCC (2018)). CH_4 has a Global Warming Potential (GWP; integrated radiative forcing relative to that of CO_2 per kg of emission) of 86 over a 20 year time horizon, including carbon cycle feedbacks (IPCC (2013)). On a global scale, 23 % of the additional radiative forcing since 1750 is attributed to CH_4, whereas total CH_4 anthropogenic emissions represent only 3 % of the ones of CO_2 in term of carbon mass flux (Etminan et al. (2016)). In recent years, the total CH_4 emissions have been rising: they increased by 5 % in the period 2008-2017 (and 9 % in 2017), compared to the period 2000-2006 (Saunois et al. (2020)). It is not clear which sources have caused these changes, but Saunois et al. (2020) estimated anthropogenic emissions to represent 60 % of the total emissions of the past 10 years. An effective reduction of CH_4 emissions requires knowledge of the locations and magnitudes of the different sources.

Atmospheric measurements of greenhouse gases at several locations have been used to investigate the rates, origins, and variations in emissions. However, for methane, these are not always in agreement with what is reported in the emissions inventories (Saunois et al. (2020)). Isotopic measurements are used to better constrain the sources of methane at regional (e.g. Levin et al. (1993), Tarasova et al. (2006), Beck et al. (2012), Röckmann et al. (2016), Townsend-Small et al. (2016), Hoheisel et al. (2019), Menoud et al. (2020b)) and global (e.g. Monteil et al. (2011), Rigby et al. (2012), Schwietzke et al. (2016), Schaefer et al. (2016), Nisbet et al. (2016), Worden et al. (2017), Turner et al. (2019)) scales. Indeed, the different CH_4 generation pathways lead to different isotopic signatures (Milkov and Etiope (2018), Sherwood et al. (2017), Quay et al. (1999)). Recently, instruments for continuous measurements of the isotopic composition of CH_4 have been developed (Eyer et al. (2016), Chen et al. (2016), Röckmann et al. (2016)) and used to characterise the main sources of a specific region (Röckmann et al. (2016), Yacovitch et al. (2020), Menoud et al. (2020b)). Using model simulations, the observations can be used to evaluate the partitioning of the different sources reported in the inventories (Rigby et al. (2012), Szénási (2020)).

Saunois et al. (2020) stated the need for more measurements in regions where very few observations are available so far. In Europe, inventories report high CH_4 emissions from Poland (European Environment Agency (2019)). In 2018, they represented 10 % of total European Union emissions, with more than 48 Mt CO_2 eq.. Half of these are from the energy sector, among which 72 % are due to the exploitation of underground coal mines (National Centre for Emission Management (KOBiZe) and Institute of Environmental Protection - National Research Institute (2020), Swolkień (2020)). The Upper Silesian Coal Basin (USCB), where most mining activity occurs in Poland, is certainly a CH_4 emission hotspot in Europe. Atmospheric measurements at the USCB were mostly performed in the recent years (Swolkień (2020), Luther et al. (2019), Gałkowski et al. (2020), Fiehn et al. (2020)), and focused on the coal extraction activities. The area covered by the USCB includes other sources of methane, such as ruminant farming and waste degradation. In this study we investigate whether we can use isotopic signals to distinguish the different sources. We attempted to detect them from Krakow, where we wanted to establish the main CH_4 sources affecting such a densely populated area. Finally, we investigate whether we can use this tool to put constrains on the emission inventories in order to improve them.

To this end, we carried out and investigated quasi-continuous measurement of CH_4 mole fraction, $^{13}C/^{12}C$ and $^{2}H/^{1}H$ isotopic ratios of CH_4 in ambient air during 6 months at a fixed location in Krakow, Poland. Time series of these isotopic ratios were also simulated with an atmospheric transport model, based on two different emission inventories. The local CH_4 sources were sampled during several mobile measurement campaigns, to determine their isotopic signatures and compared with the ambient measurements.

2 Methods

2.1 Target region and time period

The region of study is characterised by the presence of a large coal mining region: the Upper Silesian Coal Basin (USCB). It gathers 20 active coal mines spread over an area of 1100 km^2 (Swolkień (2020)), and is located about 50 km west of Krakow (Fig. 1). Other potential CH_4 sources around Krakow are from waste management and wastewater treatment facilities, industrial activity, energy production and the natural gas distribution network. Large-scale agriculture activities are not characteristic for this area, and only very few cattle farms could be located.

Ambient air measurements were performed from the Faculty of Physics and Applied Computer Science building, at AGH university in Krakow (50°04'01.1"N, 19°54'46.9"E, Fig. 1). We used a 1/2" o.d. Synflex Dekabon air intake line that draws air from the top of a mast on top of the building (35 m above ground level, 255 m a.s.l.) down to the laboratory of the Environmental Physics Group. A fraction of the incoming air was directed via a T-split to the IRMS system in the period from September 14^{th}, 2018 to March 14^{th}, 2019.

Individual emission locations of methane were visited in and around the city of Krakow, and in the USCB during mobile surveys. The surveys were performed in May 2018 (from 24^{th} to 29^{th}), February 2019 (from 5^{th} to 7^{th}) and March 2019 (from 20^{th} to 22^{th}). We visited the following areas, which are shown on the map in Fig. 1: the Silesian coal basin, Barycz landfill, the industrial park, the city center and other residential areas, and rural areas west of the city.

2.2 Sampling

The mobile surveys were conducted with an Integrated Cavity Output Spectroscopy (ICOS) instrument (MGGA - 918, Microportable Greenhouse Gas Analyser, Los Gatos Research, ABB) onboard of a car. An 1/8" Parflex inlet line was placed on top of the vehicle's roof and connected to the analyser. Real time CH_4 mole fractions were read on a tablet screen, so that an emission plume could be detected while driving. If the increase was higher than 200 ppb above background, we drove back to the plume and took one to three samples directly from the outflow of the CH_4 analyser, using sampling bags (Supel™-Inert Multi-Layer Foil, Sigma-Aldrich Co. LLC).

One or two samples were taken where we observed the lowest $\chi(CH_4)$ during each survey day, in order to obtain the background we can associate with the plumes sampled each day in a certain area.

The samples collected during the mobile surveys were analysed on the same IRMS instrument as the ambient air, partly when it was installed in Krakow, and partly when it was installed back at the IMAU lab in Utrecht.

2.3 Isotopic measurements

The $^{13}C/^{12}C$ and $^{2}H/^{1}H$ isotope ratios in CH_4 are expressed as $\delta^{13}C$ and $\delta^{2}H$ (deuterium), respectively, in per mil (‰), relative to the international reference materials, Vienna Pee Dee Belmnite (V-PDB) for $\delta^{13}C$ and Vienna Standard Mean Ocean Water (V-SMOW) for $\delta^{2}H$.

The isotopic composition measurements were performed using an Isotope Ratio Mass Spectrometry (IRMS) system, as the one described in Röckmann et al. (2016) and Menoud et al. (2020b). Ambient air or sample air measurements were interspersed with measurements of a reference cylinder filled with air with assigned composition of $\chi(CH_4)$ = 1950.3 ppb, δ^{13}C-CH_4 = -47.82 $\pm$ 0.09 ‰ V-PDB, and δ^{2}H-CH_4 = -92.2 $\pm$ 1.8 ‰ V-SMOW. The reference air bottle was previously calibrated against a reference gas measured at the Max Planck Institute in Jena, Germany (Sperlich et al. (2016)).

The extraction and measurement steps are illustrated in Fig. S1 of the supplementary material. Each measurement of either $\delta^{13}C$ or $\delta^{2}H$ returned a value of CH_4 mole fraction ($\chi(CH_4)$). A δ^{13}C-CH_4 or δ^{2}H-CH_4 value in ambient air was obtained on average every 27 minutes during the periods of normal operation. In addition to unexpected disturbances or failures, the scheduled replacement of several components (oven catalysts, chemical dryer, fittings, etc.) and the regular flushing and heating of the traps required to stop the measurements for a few hours up to a few days, several times during the study period.

The air was simultaneously measured by a CRDS instrument (G2201-i Isotopic Analyzer, Picarro) installed in the same lab as the IRMS system and drawing air from the same inlet tube. Time series of CH_4 mole fractions from both instruments were compared for quality control.

2.4 Meteorological data

Data on the hourly wind direction, speed, and temperature were obtained from an automatic weather station (Vaisala WXT520, Vaisala inc.) installed on the same building as the inlet line (220 m a.s.l.). The station is operated by the Environmental Physics Group, and the data is publicly available at http://meteo.ftj.agh.edu.pl/archivalCharts (registration required). Data on PM10 concentrations is also available on the same platform at this location.

2.5 Modelling

Time series of $\delta^{13}C$ and $\delta^{2}H$ -CH_4 were generated from simulated CH_4 mole fractions using the CHIMERE atmospheric transport model (Menut et al. (2013), Mailler et al. (2017)), driven by the PYVAR system (Fortems-Cheiney et al. (2019)). CHIMERE is a three-dimensional Eulerian limited-area chemistry-transport model for the simulation of regional atmospheric concentrations of gas-phase and aerosol species.

The simulations were carried out at a horizontal resolution of 0.1 ° x 0.1 ° in a domain covering Poland and nearby countries; [46.0° - 55.9°] in latitude and [12.0° - 25.9°] in longitude. The meteorological data used to drive CHIMERE were obtained

from the European Centre for Medium-Range Weather Forecast (ECMWF) operational forecast product. The boundary and initial concentrations of $\chi(CH_4)$ were taken from the analysis and forecasting system developed in the Monitoring Atmospheric Composition and Climate (MACC) project (Marécal, 2015). They were used to derive the background mole fractions.

The CH_4 emission rates over the domain are reported in emission inventories, following a bottom-up approach. We used two anthropogenic emission inventories for this study: EDGAR v5.0 (Emission Database for Global Atmospheric Research, Crippa et al. (2019)) and CAMS-REG-GHG v4.2 (The Copernicus Atmosphere Monitoring Service REGional inventory for Air Pollutants and GreenHouse Gases, Granier et al. (2012)). We classified the emissions in 6 anthropogenic source categories based on the European Environment Agency (EEA) greenhouse gas inventory common reporting format (CRF, European Environment Agency (2019)). We considered one additional category for natural wetland emissions, which are obtained from the ORCHIDEE-WET process model (Ringeval et al. (2011)). The classifications used in CHIMERE and the corresponding categories in the inventories are summarised in Table 1.

The isotopic values at each time t were calculated using the following formula:

$$\delta_t = \frac{1}{c_t} \sum_{i}^{n_S} (c_{S,i} * \delta_{S,i})$$

with c_t the total mole fraction from the model at time t, c_S the modelled mole fraction attributed to the source S, and δ_S the source signature of each specific source S. In this mass balance, the contribution of the background is treated as a source with assigned isotopic composition. All the assigned source signatures are defined in Table 1.

2.6 Isotopic signatures assigned to CH_4 elevations in the long-term time series

Periods of methane enhancement were identified from the $\chi(CH_4)$ time series using a peak extraction method, based on the detection of local maxima from comparison with the neighbouring points. The peaks were selected based on two criteria:

- the peak has a minimal amplitude of 100 ppb
- the peak is composed of at least three data points, from the maximum to a relative height of 0.6 times the peak height.

In order to define the background more robustly, we included additional data from the 10^{th} lower percentile of $\chi(CH_4)$ in a window of $\pm$ 24 h around the maximum of each peak. The Keeling plot method was thus applied to the data points in the peak, together with the neighbouring background data.

The Keeling plot is a mass balance approach (Keeling (1961), Pataki et al. (2003)), considering the measured CH_4 (m) in ambient air as the sum of a contribution of CH_4 from an emission source (s) and a background (bg) CH_4, such that:

$$c_m = c_{bg} + c_s$$

$$c_m \delta_m = c_{bg} \delta_{bg} + c_s \delta_s$$

with c and δ referring to the mole fraction and isotopic signatures of either ^{13}C or ^{2}H, respectively. Re-arranging the formula leads to:

$$\delta_m = c_{bg} * (\delta_{bg} - \delta_s)(1/c_m) + \delta_s$$

We assumed the background mole fraction and isotopic composition to be stable over the time period of each peak. In this case, δ_s is given by the y-intercept of the regression line, when plotting δ_m against $1/c_m$.

To derive an average source signature for the entire dataset, the Miller-Tans approach was used (Miller and Tans (2003)), because the hypothesis of stable background is violated. This method is based on the following formula:

$$c_m\delta_m = \delta_s c_m - c_{bg}(\delta_{bg} - \delta_s)$$

where δ_s is now given by the slope of the regression line, when plotting $c_m * \delta_m$ against c_m.

The linear regressions were made with the Bivariate Correlated Errors and intrinsic Scatter (BCES) fitting method (Akritas and Bershady (1996)), to allow for measurement errors in both variables. An isotopic signature was obtained for each regression. The corresponding uncertainty is always given as 1 standard deviation of the estimated parameter (intercept for the Keeling plot or slope for the Miller-Tans plot).

The method was applied to both δ^{13}C and δ^2H measurement results. If two peaks were detected within a 6 hour time window in the δ^{13}C and δ^2H time series, they were considered one single peak and the two signatures were allocated to it. The same method was also used for the modelled $\chi(CH_4)$ time series, to allow the comparison of modelled and measured source signatures.

3 Results and discussion

3.1 Observed time series

The observed time series are shown in Fig. 2, together with measurements from the KASLAB laboratory at the top of Kasprowy Wierch, a mountain in southern Poland (49°13'57"N, 19°58'55"E, 1989 m a.s.l.; Necki et al. (2013)). We note that in the period February-March 2019, we observed a mismatch of about 80 ppb between the IRMS-derived and simultaneous CRDS $\chi(CH_4)$ measurements in the same laboratory (shaded area in Fig. 2). A mismatch in mole fraction can potentially affect the Keeling plot intercepts, and we investigated possible artefacts using various attempts for correction. We realised that the effect of these corrections on the isotopic source signatures is small compared to the observed range (average peak δ^{13}C and δ^2H changed by 0.1 ‰; differences per peak are shown in Fig. S2). As no obvious reason for a malfunction of the IRMS instrument could be detected, we decided to use the original data without correction. The peaks in $\chi(CH_4)$, compared to the background measured at Kasprowy Wierch, reflect pollution events in Krakow or advected to the measurement site. The maximum $\chi(CH_4)$ value was 3634 ppb, measured on October 19th, 2018 at 5:30 am. Simultaneous changes are visible in the δ^{13}C and δ^2H time series. Increased $\chi(CH_4)$ were always linked with a lower δ^2H, but for δ^{13}C the measured values could be higher or lower.

The general background threshold is 1986.0 ppb, which corresponds to the 10th lower percentile of the entire dataset. We have found that 70.5 % of the background values ($\chi(CH_4) < 1986.0$ ppb) occurred during daytime. The dominant feature in the CH_4 time series is indeed the presence of a diurnal cycle: $\chi(CH_4)$ elevations regularly occurred during the night. This is due to the lowering of the boundary layer when the temperature decreases in the evening. The morning and evening variations in $\chi(CH_4)$ were negatively correlated with the temperature data we obtained at the study site. In addition, there were isolated

pollution events occurring on top of the night-time accumulation. Between the emission peaks, $\chi(CH_4)$ generally went back to a local background level.

The night-time accumulation was particularly visible in the period September 14th to mid-November 2018, and shown in the supplementary material (Fig. S3). Similar nighttime elevations are also visible in the observations of other pollutants such as PM10 at the study location. There was a clear difference in local temperature before and after November 15, 2018: the average air temperature decreased from 12 $\pm$ 5.3 ºC to 2.1 $\pm$ 4.4 ºC and the dew point temperature from 5.3 $\pm$ 3.4 ºC to -3.9 $\pm$ 3.4 ºC until the end of the measurements. The period before mid-November will be referred to as fall throughout the paper.

The wind directions at the study site were combined with the CH_4 measurement data in Fig. 3; and with wind speeds in Fig. S4 of the supplementary material. The spread of the wind directions was similar for most of the months: mainly from the west, and partly from east/north-east. An exception was November 2018, when most of the wind was from the east/north-east direction. March 2019 was characterised by winds from the west only, and at particularly strong speeds (on average 3.1 m/s, compared to 1.8 m/s for the other months; Fig. S4). The average CH_4 diurnal cycle, defined as the prominence of night peaks, was on average 334 ppb throughout the entire time period, but only of 195 ppb when the winds were $>$ 2.5 m/s. This decrease in amplitude with higher wind speeds was not influenced by the direction of the wind. During fall, 84 % of the peaks were observed at night and associated with low wind speeds, which suggests the influence of local pollution sources, and a relatively low influence of the wind direction.

The average isotopic values of the background were δ^{13}C = -47.8 $\pm$ 0.16 ‰, and δ^2H = -90.0 $\pm$ 3.0 ‰. The CH_4 elevations were associated with consistently more negative δ^2H, but varying δ^{13}C. This indicates that the sources were sometimes higher in δ^{13}C compared to the ambient CH_4 (i.e. δ^{13}C$>$ -47.8 ‰). In contrast, all CH_4 elevations were associated with lower δ^2H during the entire time period.

3.2 Modelled time series

The CH_4 time series obtained with CHIMERE for the grid cell containing the observation site, are shown in Fig. 4. We first compared the CH_4 mole fractions measured at Krakow and modelled by CHIMERE in Fig. 5. They show a poor correlation (Person's correlation coefficients r^2 = 0.527 and r^2 = 0.514, for model calculations using the EDGAR v5.0 and CAMS-REG-GHG v4.2 inventories, respectively; Fig. 5.A). The model globally under-estimates the measured $\chi(CH_4)$ significantly, with a root mean square error (RMSE) of 164.4 ppb and 173.4 ppb for EDGAR and CAMS, respectively. Yet we see that modelled $\chi(CH_4)$ can sometimes be larger than the observations, which is usually due to a shift in the timing of a pollution event (Fig. 4). The wind data used in the model are generally in good agreement with the wind measurements at the study site, but small discrepancies can partly explain the differences in the timing of the peaks. The time series are best reproduced during the fall 2018, using EDGAR v5.0 (r^2 = 0.648; Fig. 5.B). As mentioned in section 3.1, this period shows a more regular pattern of night-time elevations of relatively similar amplitudes compared to the winter period. This is better reproduced by the model (Fig. 4). However, the two highest $\chi(CH_4)$ measurements were observed in this period (October 18, and November 3, 2018) and were not modelled to the same level (points on the lower right, Fig. 5.B). These events largely contribute to the general model under-estimation when only considering the fall data.

In winter, the pollution events were less regular, with a less predictable $\chi(CH_4)$ diurnal cycle. The mismatch in the timing of pollution events caused an over-estimation by the model (points on the upper left, Fig. 5.B). The general slope is still lower than 1, and the fit is worse than during fall. There is a general under-estimation of the CH_4 mole fractions at Krakow by the model. This could be explained by the model time series being hourly averages, compared to the observations of sampled air. To account for this bias, we compared the model data with observations that are also averaged over a 1h window, and/or interpolated to the modelled times. This had no effect on the correlation coefficients, suggesting a minor impact of the temporal representation error. But potential CH_4 sources in the close surroundings of the laboratory could affect the measurements compared to the model, where they are diluted over the 11 km grid cell. This spatial representation error could explain $\chi(CH_4)$ under-estimation in CHIMERE. Other potential reasons of misfit include errors in the transport modelling or too low emissions in the inventories. Szénási (2020) identified the emission inventories as the main source of discrepancies between CHIMERE results and measured time series at two other European locations. The implications on the two inventories are discussed in detail in section 3.4.

Time series of $\delta^{13}C$ and $\delta^{2}H$ in CH_4 show negative or positive excursions relative to the background, and are linked to $\chi(CH_4)$ peaks (Fig. 4). When using CAMS-REG-GHG v4.2, $\delta^{13}C$ and $\delta^{2}H$ are always negatively correlated with $\chi(CH_4)$. But when using the EDGAR v5.0 inventory, $\delta^{13}C$ values are closer to the background, and only $\delta^{2}H$ values are systematically lower at higher $\chi(CH_4)$. The isotopic discrepancies will be analysed in detail in relation to the source partitioning in the inventories, and the signatures we assigned to each source in section 3.4.

3.3 Isotopic source signatures

A total of 126 and 156 peaks were identified in the $\delta^{13}C$ and $\delta^{2}H$ time series, respectively. 114 peaks were measured commonly by both isotope lines. From the Keeling plot applied to each of the peaks, we obtained the source signatures of the corresponding accumulation events. They can be compared with the determined isotope signatures of the sources sampled in the surrounding area (Fig. 6.A).

3.3.1 Isotopic characterisation of the surrounding sources

The results from individual sites are presented in Table 2, and shown in the supplementary material (Fig. S6.A). They are in good agreement with the ranges defined for the different categories in the literature (Sherwood et al. (2017)). Biogenic sources (a landfill, 3 manholes and a cow barn) correspond to the acetate fermentation pathway, characterised by relatively depleted $\delta^{13}C$ ($<$ -50 ‰) and $\delta^{2}H$ ($<$ -275] ‰; Milkov and Etiope (2018)). The landfill CH_4 is isotopically more enriched than the cow barn. This can be due to an isotope fractionation from diffusion and oxidation in the soil layers (De Visscher (2004), Bakkaloglu et al. (2021)). The fossil fuel CH_4 emissions we sampled were from coal exploitation and use of natural gas. The natural gas distribution network was sampled outside of compressor stations, close to gas stations and supply valves in residential areas. The results ranged between [-52.4, -44.1] ‰ for $\delta^{13}C$, and [-226, -176] ‰ for $\delta^{2}H$. To check for temporal variations, two plumes were sampled at an interval of 6 weeks, on February 5 and March 19, 2019. The $\delta^{13}C$ results agreed within $\pm$ 5 %, and the $\delta^{2}H$ within $\pm$ 10 %. One sample was directly taken from the gas supply pipe at the AGH lab in March 2019. The pure

gas was 3.4 ‰ and 13 ‰ more depleted in δ^{13}C and δ^{2}H, respectively, than the average from all leaks (signature in brackets in Table 2), but still falls in the same range as the sampled leaks. The network gas composition can change in time because the proportions of gas from several origins varies. Gas migrating in the distribution network can undergo secondary processes such as oxidation, that influence the isotopic signatures, usually towards more enriched values. Isotopic variations among network gas leaks were also observed previously in other cities (Zazzeri et al. (2017), Maazallahi et al. (2020), Defratyka et al. (2021)).

CH_4 emissions from manholes were often observed in the Krakow urban area. The resulting isotopic signatures do not indicate one clear origin, and were divided in two groups with distinct δ^{2}H (Table 2). While the isotopically depleted signatures observed at 3 locations likely come from the sewage system, with a $\delta^{2}H < -250$ ‰, the 5 others contain particularly enriched thermogenic gas (δ^{13}C between [-42.2; -33.3] and δ^{2}H [-201; -148] ‰; Fig. S6.A). We hypothesise that this indicates leakage of natural gas from the distribution pipes to the sewage network, which is sometimes further oxidised leading to even more enriched isotope signatures.

For most emission plumes, we could not visually identify an obvious CH_4 source. The isotopic signatures of these "unknown" sources range from -57.3 to -42.4 ‰ V-PDB for δ^{13}C and from -291.5 to -88.2 ‰ V-SMOW for δ^{2}H. The δ^{2}H range is particularly large, indicating the presence of both fossil fuel and biogenic sources. The average $\delta^{2}H > 200$ ‰, suggesting a major influence from fossil fuel sources. The δ^{13}C is in good agreement with the signature found for natural gas (Table 2 and Fig. S6.A), and since most of these locations were close to roads and urban settlements, it is likely that they were natural gas leaks.

The isotope signatures from coal mine ventilation shafts and residential gas leaks sampled in this study fall in the same range: δ^{13}C between -58.9 and -28.0 ‰ V-PDB, and δ^{2}H between -254 and -139 ‰ V-SMOW, although coal CH_4 has a wider isotopic range. The values of $\delta^{13}C < -60$ ‰ confirmed the presence of microbial gas in the USCB, and reported in the literature (Kotarba (2001), Kotarba and Pluta (2009) and Kedzior et al. (2013); Fig. S6.A). Most δ^{13}C values from coal mines in this study were found between -58 ‰ and -45 ‰, which also indicates a contribution from microbial gas sources, although in our measurements all δ^{13}C signatures from time series peaks and sampled shafts were $>$ -60 ‰. Some of the locations sampled in by Kotarba (2001) were re-visited in this study. However, their method used direct sampling of CH_4 from different coal layers, aiming at representing the variety in the origin of the gas reservoirs. Our approach was to sample outside the shafts, to obtain the isotopic signature of CH_4 emissions from these shafts to the atmosphere. The very depleted δ^{13}C values obtained in these previous studies confirm the presence of purely microbial gas reservoirs in the USCB coal deposits, but our results show that thermogenic gas represents a larger part of the fugitive emissions from mining activities in this area than indicated by Kotarba (2001; Fig. 6.A). The heterogeneity of isotopic signatures from coal mining activities in the USCB reflects the geological complexity of the area. Secondary processes (desorption, diffusion or oxidation) also influence the CH_4 isotopic composition, and depend on external parameters such as physical characteristics of the coal reservoirs and the soil layers (Niemann and Whiticar (2017)). These represent additional difficulties as regards the isotopic characterisation of coal associated CH_4 emissions.

The δ^{2}H signatures allow us to identify the CH_4 emissions from microbial fermentation: values below -250 ‰ are indicative of the anaerobic fermentation pathway, such as in the rumen of cows or during waste degradation. Except for one shaft with

δ^2H = -254 $\pm$ 0.01 ‰ (possibly very early mature thermogenic gas in deep formations, or a late stage of biodegradation if close to the surface; Milkov and Etiope (2018)), both literature data and our sampled shafts have a δ^2H > -250 ‰. This is also true for emissions from the natural gas network, confirming their fossil fuel origin. In the USCB region, δ^2H signatures seem to be more suitable than δ^{13}C values for source apportionment, similar to recent studies made in European cities (in Hamburg by Maazallahi et al., 2020, and in Bucharest by Fernandez et al., 2021)

3.3.2 Isotopic characterisation of CH_4 in ambient air

The isotopic signatures of the CH_4 pollution events observed in Krakow during the study period are shown in Fig. 6. δ^{13}C varied between -55.3 and -40.0 ‰ V-PDB, and δ^2H between -267 and -127 ‰ V-SMOW. As mentioned above, the observed δ^{13}C either increased or decreased with higher $\chi(CH_4)$, indicating source signatures either lower or higher than the background value. Yet δ^{13}C signatures stayed within $\pm$ 8 ‰ from the background, thus never reaching extreme values. The proportion of CH_4 peaks enriched in δ^{13}C with respect to the background was 40.5 %. In contrast, the observed δ^2H values were always more depleted than ambient. The overall source signatures resulting from the Miller-Tans analysis using all the data points were δ^{13}C = -48.3 $\pm$ 0.19 ‰, and δ^2H = -203 $\pm$ 0.95 ‰ (Fig. S5). The comparison with typical signatures of the different CH_4 formation processes indicates that most of these events were from thermogenic sources (Fig. S6.B). When compared with isotope signatures of the surrounding sources (Fig. 6.A), the source signatures from the long-term time series match the range of coal mine and natural gas emissions the best. Fig. 6.B shows that most pollution events associated with strong winds fall in the range of more depleted δ^{13}C signatures. They were also all advected from west of Krakow, where the USCB is located (Fig. 1). In fact, the δ^2H signatures exclude a large contribution from potential biogenic sources, and point towards the emissions from coal mines in Silesia.

In Röckmann et al. (2016) and Menoud et al. (2020b), CH_4 mole fractions, δ^{13}C and δ^2H isotopic signatures in ambient air were measured at two locations in the Netherlands. The time series covered 5 months in 2014-2015 and 2016-2017, at Cabauw and Lutjewad, respectively. The average isotopic signatures were -60.8 $\pm$ 0.2 ‰ and -298 $\pm$ 1 ‰ at Cabauw and -59.5 $\pm$ 0.1 ‰ and -287 $\pm$ 1 ‰, for δ^{13}C and δ^2H, respectively. The main sources contributing to the CH_4 emissions in the Netherlands are cattle farming and waste management. These are biogenic sources, with isotopic signatures representative for the microbial fermentation origin. CH_4 of fossil fuel origin had a minor contribution there, which contrasts a lot with the results from Krakow. Such drastic differences in the isotopic signals of the same greenhouse gas show how a region-specific analysis is crucial to effectively constrain atmospheric emissions.

In Fig. 7, the results of CH_4 mole fraction, peak source signatures and wind speed and direction are shown in more details for 8 days in November 2018, and 7 days in February 2019, together with model results using EDGAR v5.0.

In general, eastern winds advected CH_4 with a relatively enriched δ^{13}C: 60 % were higher than the background δ^{13}C, and all but one were > -50 ‰ V-PDB. In November, the wind was mostly coming from the east (Fig. 3), but elevations were observed at low wind speed (Fig. 7.A, peaks 4 to 7). These pollution events reflect the general signature of the CH_4 emitted in the Krakow urban area and are unlikely to come from coal mines. In Fig. 7.A, the peaks C, D, E and G show a large contribution from the natural gas and from the "other anthropogenic" categories. The latter represents mainly the power generation and transportation

sectors, as well as the manufacture, chemical and metal industries. The main contribution is the energy production from fossil fuels, and we assigned a δ^{13}C signature corresponding to fossil fuel CH_4 to this category (Table 1). The modelled results for these peaks are generally similar to the measured ones. The magnitude of the $\chi(CH_4)$ elevations also matches the observations relatively well: modelled peaks 3, 4, and 5 were 79 ppb, 23 ppb and 14 ppb larger than the observed peaks C, D and E, respectively. Yet for peak C (observed peak 3), the model δ^{13}C signature is 2.5 ‰ lower than the one from the measurements, and showed a majority of emissions from "other anthropogenic" sources (37 %). Part of these emissions can be from the incomplete combustion of CH_4, and such combustion-related emissions have a more enriched δ^{13}C signature than fossil fuel CH_4 (Fig. 6.A). Results from mobile surveys in Paris identified fuel-based residential heating systems as urban CH_4 sources, with a slightly more enriched isotopic composition than the local gas leaks (Defratyka et al. (2021)). Therefore, either the proportion of emissions in the "ENB" category, or the δ^{13}C signature assigned to the "other anthropogenic" emission category were under-estimated. We note that we couldn't characterise this source category by sampling. Uncertainties in the assigned signature are unavoidable when a given category is a combination of different sources; not only the processes have different isotopic signatures, but the contribution from the different sources could change from one pollution event to another. For δ^{2}H, the agreement between observed and modelled signatures for these November night peaks is good. All fossil fuel and pyrogenic δ^{2}H signatures used in this study are relatively close to each other (Table 1), and to the average peak δ^{2}H source signature. Thus, the δ^{2}H signatures do not allow for a distinction between these two processes.

Some peaks advected at low wind speeds during night are also visible in Fig. 7.B (peaks 9 to 11), and show similarly enriched δ^{13}C signatures. The wind direction was different for these night peaks between February and November, but the low wind speeds again indicate that this represents the local emission mix. The model time series showed peaks that occurred simultaneously to the measured ones (K and L in Fig. 7.B), although with different $\chi(CH_4)$ maxima than the measurements (-115, -339 and +203 ppb, respectively). For peaks K and L, the source partitioning from the inventory is similar to the other night peaks shown in Fig. 7.A. The δ^{13}C signatures of these urban emissions are however under-estimated in the model, and so are the CH_4 mole fractions, in particular for peak 11 (corresponding to peak L in the model time series). We suggest that at a close distance east of the study site, the share of emissions from the combustion sources is likely under-estimated. These additional emissions could be from residential heating or the energy production sector. The δ^{2}H signature of peak 11 (L) also differs significantly between model and measurements. This further indicates that the missing CH_4 emissions must be mostly combustion related, because of the relatively enriched δ^{13}C and δ^{2}H we observed (-44.9 ‰ V-PDB and -199 ‰ V-SMOW, respectively, for peak 11).

The δ^{13}C signatures shifted towards more depleted values after February 19. δ^{13}C went from -44.9 $\pm$ 0.6 ‰ for peak 11 to -50.5 $\pm$ 0.7 ‰ for peak 13. Peaks 12 and 13 (respectively M and N in the model), were advected by strong western winds. The share of coal related emissions reported in the inventory increased from peak M compared to peaks K and L, and is supported by the decrease in δ^{13}C also in the modelled signatures. This confirms a source shift from urban to coal activities further west of Krakow from February 19, 2019. Whenever the EDGAR inventory reported large contributions from coal mine emissions, such as in for peaks F, H, K, M and N (corresponding to 6a, 8, 10a, 12 and 13, respectively), the model wind direction corresponds to the USCB. The associated isotopic signatures were in relatively good agreement for peaks H, M, and N, where coal emissions

represented $>$ 50 % of the total. Small discrepancies ($\pm$ 2 ‰ in δ^{13}C) are explained by the heterogeneity of isotopic signatures from the different mine shafts. This confirms that the average isotopic signatures for this category are well characterised in this study. For peaks F and K, δ^{13}C values are at least 2 ‰ lower than the observations (peaks 6a and 10a). The share of emissions from the USCB are therefore likely over-estimated in these 2 cases.

Three peaks showed a δ^{2}H $<$ -260 ‰ V-SMOW, suggesting a larger contribution from biogenic sources (Fig. 6.A). They are associated with large uncertainties, because the peak magnitudes were low. These peaks were not modelled by CHIMERE, using either inventory. They represent isolated pollution events, disconnected from the daily cycle and not particularly related to a certain wind direction. There could be occasionally larger biogenic emissions such as from a waste facility that are advected to the measurement site. In Fig. 7.B, a depleted δ^{2}H signature was derived from a small peak (12a). The $\chi(CH_4)$ enhancement was not significant in the time series of δ^{13}C, which suggests a very short pollution event. It still correlated with a short-term change in wind direction towards a more north/north-west origin. Such abrupt changes are not visible in the model wind data, because of its coarser temporal resolution. Based on its clearly biogenic isotopic signal, as well as the wind direction, this event might reflect the contribution from the 2 large waste treatment facilities located north-west of Krakow (Fig. 1). This needs to be confirmed by observations at higher mole fractions to reduce the uncertainty in the source signature, and be able to derive a signature for δ^{13}C, as we are reaching here our detection limit. Further measurements at this location would be useful to specifically characterise this source.

In addition to the night time accumulations of CH_4, we observed occasional $\chi(CH_4)$ peaks during the day, not linked to the night-time lowering of the boundary layer. CH_4 emissions coming from a specific location and advected by strong winds to the measurement site resulted in sharp peaks, such as peak 2 in Fig. 7.A, that are separate from the daily cycle. An increase in wind speed (from 0.7 to 2.2 m/s) and constant wind direction of 251 ° caused a sharp increase in $\chi(CH_4)$ by 1360 ppb, over only 3h. The peak was reproduced by the model (peak A), but with a lower magnitude, which can be explained by the differences in the wind data. The observed source signatures were δ^{2}H = -190 $\pm$ 5.1 ‰, indicating fossil fuel related emissions, and δ^{13}C = -50.6 $\pm$ 0.26 ‰, pointing to localised coal mine fugitive emissions. The isotope signatures from the model using the EDGAR inventory differ significantly from the observed ones, even though coal extraction is still indicated as main source. The input source signatures in the model represent all coal related emissions and therefore might fail in reproducing the signature of emissions at the scale of individual sites.

3.4 CH_4 source partitioning in the inventories linked to isotopic composition

The CH_4 emissions for each source category from the inventories over the studied domain and the simulated CH_4 mole fractions in the grid-cell of the measurements location are presented in Table 3.

Compared to simulations made with EDGAR v5.0, the modelled isotopic signatures with CAMS-REG-GHG v4.2 show that the CH_4 sources are always more isotopically depleted in δ^{13}C (section 3.2, Fig. 4). When looking at the source partitioning between the 2 inventories, this can be explained by the much higher contribution from waste emissions when using the CAMS inventory (Table 3). These emissions have a particularly large influence at our study site (43.8 % of total added mole fraction), whereas the share in the emissions is not so large over the entire domain (26.2 % of total emissions). The emissions maps of

both inventories are shown in Fig. S7 of the supplementary material. The higher waste emissions in CAMS-REG-GHG v4.2 are indeed coming from the Silesia region (Fig. S7). There is no evidence of particularly large amounts of domestic waste or waste collection facilities in this area. The Silesia and Krakow regions report comparable amounts of municipal waste per inhabitants, and in the same range as other regions of Poland (Statistics Poland, 2018). However, there is 5 times more waste from mining activities reported in Silesia than the other Polish regions (Statistics Poland, 2018). The emissions reported by CAMS are therefore associated with coal mining activities, especially mineral washing in the coal preparation plants. In our approach of distinguishing sources based on their isotopic signature, these emissions should be considered as fossil fuel related. However, in the CAMS inventory they are combined with waste emissions from the fermentation of organic substrate, which have a distinctly depleted isotope signature (Table 2, Fig. 6.A). The emissions from on-site energy use for coal mining and for the manufacture of secondary and tertiary products from coal are included in the "other anthropogenic" category in both inventories (CRF sector 1.B.1.c, European Environment Agency (2019)). But in the EDGAR inventory, emissions categorised as from coal mining include fugitive emissions from the extraction and all the processing steps prior to combustion (CRF sector 1.B.1.a, European Environment Agency (2019)). They were therefore associated with the same signature as the coal extraction itself, which results in a better match with the observations than when using CAMS-REG-GHG v4.2.

The isotopic signatures per peak obtained from the model are compared with the ones from the observations in Fig. 8. The histograms show the distribution of isotopic signatures from the Keeling plots applied to each peak we extracted from the measured and modelled time series. The correlation plots allow to compare the CH_4 peaks detected simultaneously in the observed and modelled time series.

When using the CAMS-REG-GHG v4.2 inventory, the δ^{13}C source signatures varied between -52.4 and -48.5 ‰, a much more narrow range than from -55.3 to -39.4 ‰ for the observations. This reflects the over-representation of the waste category and its associated depleted δ^{13}C signature. This bias towards depleted values is also visible in the δ^{2}H signatures. The source signatures when using the EDGAR v5.0 inventory match the observations better: the average δ^{13}C and δ^{2}H of all elevations agree within their uncertainties, and the δ^{13}C signatures are slightly correlated (r^2=0.33). The distribution of δ^{13}C signatures with EDGAR has a bimodal shape that we also observe in the measured data, but covers a smaller range of values. Some of the most enriched signatures in the observations are not reproduced by the model, for both δ^{13}C and δ^{2}H (Fig. 8). As shown in Fig. 6.A, δ^{2}H allows to distinguish microbial fermentation from fossil fuel (or pyrogenic) sources, whereas the δ^{13}C ranges for these 2 source types overlap. This suggests that the fossil fuel fugitive and combustion related emissions in the inventories are under-estimated. This corresponds to our findings from analysing the emission peak signatures of Fig. 7, and is consistent with the lower $\chi(CH_4)$ in the model compared to the observations described above (Fig. 5).

Finally, the absence of correlation between δ^{2}H signatures from model and observations (Fig. 8.B) emphasises the need for more δ^{2}H measurements in order to more precisely constrain the sources for this isotope signature. This limits the conclusions we could derive from measurements of δ^{2}H.

4 Conclusions

This study presents measurements of CH_4 mole fractions, $\delta^{13}C$ and δ^2H of CH_4 in ambient air, performed continuously during 6 months in 2018 - 2019 at Krakow, Poland. The results were combined with model simulations from a high-resolution regional transport model based on two different emission inventories.

The source signatures of the pollution events observed in Krakow were compared with signatures from sources sampled around the study area. This allows us to identify the fossil fuel related sources as the main contributor to the CH_4 emissions. The wind directions pointed towards Silesian coal mines, but the use of natural gas in the urban area of Krakow is also an important source. Our results showed that despite the presence of microbial CH_4 reservoirs, CH_4 of thermogenic origin contributes the most to the atmospheric emissions from the USCB mine shafts. Despite their variability, the CH_4 isotopic signatures of Silesian coal mines are generally well understood. This study significantly helps constraining the CH_4 isotopic signatures from the USCB coal mining activities. Our isotopic observations when the wind was from the west at relatively high speeds confirm the prominence of coal related CH_4 emissions compared to biogenic ones (agriculture and waste).

In comparison to measurements made in the Netherlands (Röckmann et al. (2016), Menoud et al. (2020b)), the range of CH_4 isotopic signatures derived from the Krakow measurements was more enriched in $\delta^{13}C$ and δ^2H, by 10 ‰ and 100 ‰, respectively. These large differences are directly related to the heterogeneity in the human activities impacting our climate: from agriculture (especially cattle farming) in the Netherlands, to the exploitation of fossil fuels in Poland. This provides additional evidence for the value that the analysis of isotopologues can have in constraining the local to regional methane budget.

The $\chi(CH_4)$ computed using both inventories matched the measurements rather well (r^2=0.65 using EDGAR v5.0) during fall 2018. However, the agreement is less during the winter months (r^2=0.40), largely reflecting discrepancies in the timing of the pollution events. The model also under-estimated the CH_4 levels by on average 170 ppb compared to the observations. The isotopic results suggest that increased emissions in the inventories must be of fossil fuel origin.

The average isotopic source signatures from the model using the EDGAR v5.0 inventory were in good agreement with the ones from the measurements, which confirms the source attribution. Larger differences were observed on the level of individual peaks. Uncertainties remain because of the combination of different sources within one category in the EDGAR v5.0 inventory. Small discrepancies between observed and modelled signatures are also due to the inherent diversity of isotopic signatures, even within one source category, like we observed when sampling the USCB mines. But the emissions within the Krakow urban area, where multiple CH_4 sources are detected at the study site, are affected in a particular way. The CAMS-REG-GHG v4.2 inventory quantified waste emissions as the main contributor to the regional CH_4 emissions, but does not distinguish residential waste from waste associated with the processing of coal, which resulted in a large bias towards isotopically depleted sources. Therefore, our method fails to assess in detail the performance of this inventory. Nevertheless we show the power of continuous isotope data for analysing CH_4 emission sources on monthly and daily scales, in a very detailed manner. The sensitivity of our approach allows precise identification of the different sources. These measurements can be used in future work to improve and validate inventories, and help mitigation. This requires CH_4 sources to be characterised locally, and additional sampling campaigns in the city of Krakow would be required to better define the different sources and their isotopic composition.

Using δ^2H measurements in the identification of the sources was more powerful in this region, compared to δ^{13}C, as the δ^{13}C from coal mine activities and the network gas overlaps with CH_4 emitted from microbial sources such as waste. Yet our conclusions using δ^2H isotopes are restricted by the limited amount of δ^2H measurements available. Our δ^{13}C data generally support the recent re-evaluations of global δ^{13}C-CH_4 from fossil fuel sources towards less enriched values (Schwietzke et al. (2016)). The data presented here was collected in an area that has been under-investigated in the past, compared to its importance for the European CH_4 emissions. It is therefore an important contribution to studies on the global CH_4 budget. The high time resolution and temporal coverage of $\chi(CH_4)$, δ^{13}C and δ^2H in CH_4 provided by this data is also particularly helpful to evaluate transport models on regional and global scales.

Data availability. The data that support the findings of this study are openly available at https://doi.org/10.5281/zenodo.4548748, upon request. It will be made open access once the article is published.

Author contributions. M.M., C.V. J.N. and J.B. performed the isotopic measurements. M.M., J.N. and M.S. performed the mobile surveys and sampling. M.M. and C.V. processed the experimental data. B.S. performed the model simulation. M.M. performed the analysis, drafted the manuscript and designed the figures. T.R. aided in interpreting the results and worked on the manuscript. J.N., B.S., I.P., and T.R., discussed the results and commented on the manuscript. J.N., I.P., P.B. and T.R. were involved in planning and supervised the work.

Competing interests. No competing interests apply for this work.

Acknowledgements. This work was supported by the ITN project Methane goes Mobile – Measurements and Modelling (MEMO^2; https://h2020-memo2.eu/). This project has received funding from the European Union's Horizon 2020 research and innovation programme under the Marie Sklodowska-Curie grant agreement No 722479. We specially thank all the team members of the experimental physics lab of AGH for their support in the installation and maintenance of the IRMS system.

We acknowledge ECCAD (Emissions of atmospheric Compounds and Compilation of Ancillary Data) for the archiving and distribution of the data.

References

Akritas, M. G. and Bershady, M. A.: Linear Regression for Astronomical Data with Measurement Errors and Intrinsic Scatter, The Astrophysical Journal, 470, 706, https://doi.org/10.1086/177901, 1996.

Bakkaloglu, S., Lowry, D., Fisher, R., France, J., Brunner, D., Chen, H., and Nisbet, E.: Quantification of Methane Emissions from UK Biogas Plants, Waste management, in-press, 2021.

Beck, V., Chen, H., Gerbig, C., Bergamaschi, P., Bruhwiler, L., Houweling, S., Röckmann, T., Kolle, O., Steinbach, J., Koch, T., Sapart, C. J., van der Veen, C., Frankenberg, C., Andreae, M. O., Artaxo, P., Longo, K. M., and Wofsy, S. C.: Methane Airborne Measurements and Comparison to Global Models during BARCA: METHANE IN THE AMAZON DURING BARCA, Journal of Geophysical Research: Atmospheres, 117, [15310], https://doi.org/10.1029/2011JD017345, 2012.

Chen, Y., Lehmann, K. K., Peng, Y., Pratt, L., White, J., Cadieux, S., Sherwood Lollar, B., Lacrampe-Couloume, G., and Onstott, T.: Hydrogen Isotopic Composition of Arctic and Atmospheric CH_4 Determined by a Portable Near-Infrared Cavity Ring-Down Spectrometer with a Cryogenic Pre-Concentrator, Astrobiology, 16, 787–797, https://doi.org/10.1089/ast.2015.1395, 2016.

Crippa, M., Guizzardi, D., Muntean, M., Schaaf, E., Vullo, L., Solazzo, E., Monforti-Ferrario, F., Olivier, J., and Vignatti, E.: EDGAR v5.0 Greenhouse Gas Emissions, Tech. rep., European Commission, Joint Research Centre (JRC), 2019.

De Visscher, A.: Isotope Fractionation Effects by Diffusion and Methane Oxidation in Landfill Cover Soils, Journal of Geophysical Research, 109, D18 111, https://doi.org/10.1029/2004JD004857, 2004.

Defratyka, S., Paris, J.-D., Yver-Kwok, C., Fernandez, J. M., Korbeń, P., and Bousquet, P.: Mapping Urban Methane Sources in Paris, France, Environmental Science and Technology, In review, 2021.

Etminan, M., Myhre, G., Highwood, E. J., and Shine, K. P.: Radiative Forcing of Carbon Dioxide, Methane, and Nitrous Oxide: A Significant Revision of the Methane Radiative Forcing: Greenhouse Gas Radiative Forcing, Geophysical Research Letters, 43, 12,614–12,623, https://doi.org/10.1002/2016GL071930, 2016.

European Environment Agency: Annual European Union Greenhouse Gas Inventory 1990-2017 and Inventory Report 2019, Submission under the United Nations Framework Convention on Climate Change and the Kyoto Protocol EEA/PUBL/2019/051, European Commission, Copenhagen, Denmark, 2019.

Eyer, S., Tuzson, B., Popa, M. E., van der Veen, C., Röckmann, T., Rothe, M., Brand, W. A., Fisher, R., Lowry, D., Nisbet, E. G., Brennwald, M. S., Harris, E., Zellweger, C., Emmenegger, L., Fischer, H., and Mohn, J.: Real-Time Analysis of $\delta\ ^{13}C$- and δD-CH_4 in Ambient Air with Laser Spectroscopy: Method Development and First Intercomparison Results, Atmospheric Measurement Techniques, 9, 263–280, https://doi.org/10.5194/amt-9-263-2016, 2016.

Fernandez, J. M., Maazallahi, H., France, J. L., Corbu, M., Menoud, M., Ardelean, M., Calcan, A., van der Veen, C., Röckmann, T., Fisher, R. E., Lowry, D., and Nisbet, E. G.: Something about Urban Methane Emissions in Bucharest, Romania, Atmospheric Environment, In preparation, 2021.

Fiehn, A., Kostinek, J., Eckl, M., Klausner, T., Gałkowski, M., Chen, J., Gerbig, C., Röckmann, T., Maazallahi, H., Schmidt, M., Korbeń, P., Nęcki, J., Jagoda, P., Wildmann, N., Mallaun, C., Bun, R., Nickl, A.-L., Jöckel, P., Fix, A., and Roiger, A.: Estimating CH_4, CO_2, and CO Emissions from Coal Mining and Industrial Activities in the Upper Silesian Coal Basin Using an Aircraft-Based Mass Balance Approach, Atmospheric Chemistry and Physics Discussions, https://doi.org/10.5194/acp-2020-282, 2020.

Fortems-Cheiney, A., Pison, I., Dufour, G., Broquet, G., Berchet, A., Potier, E., Coman, A., Siour, G., and Costantino, L.: Variational Regional Inverse Modeling of Reactive Species Emissions with PYVAR-CHIMERE, Preprint, Atmospheric Sciences, https://doi.org/10.5194/gmd-2019-186, 2019.

Gałkowski, M., Jordan, A., Rothe, M., Marshall, J., Koch, F.-T., Chen, J., Agusti-Panareda, A., Fix, A., and Gerbig, C.: In Situ Observations of Greenhouse Gases over Europe during the CoMet 1.0 Campaign Aboard the HALO Aircraft, Preprint, Gases/In Situ Measurement/Instruments and Platforms, https://doi.org/10.5194/amt-2020-287, 2020.

Granier, C., D'Angiola, A., Denier van der Gon, H., and Kuenen, J.: Report on the Update of Anthropogenic Surface Emissions, MACC-II Deliverable Report D 22.1, TNO Department of Climate, Air and Sustainability, Utrecht, Netherlands, 2012.

Hoheisel, A., Yeman, C., Dinger, F., Eckhardt, H., and Schmidt, M.: An Improved Method for Mobile Characterisation of $\delta^{13}CH_4$ Source Signatures and Its Application in Germany, Atmospheric Measurement Techniques, 12, 1123–1139, https://doi.org/10.5194/amt-12-1123-2019, 2019.

IPCC: Climate Change 2013: The Physical Science Basis ; Working Group I Contribution to the Fifth Assessment Report of the Intergovernmental Panel on Climate Change, Cambridge Univ. Press, Cambridge, UK and New York, NY, USA, 2013.

IPCC: Global Warming of 1.5°C. An IPCC Special Report on the Impacts of Global Warming of 1.5°C above Pre-Industrial Levels and Related Global Greenhouse Gas Emission Pathways, in the Context of Strengthening the Global Response to the Threat of Climate Change, Sustainable Development, and Efforts to Eradicate Poverty, In Press, 2018.

Kedzior, S., Kotarba, M. J., and Pekała, Z.: Geology, Spatial Distribution of Methane Content and Origin of Coalbed Gases in Upper Carboniferous (Upper Mississippian and Pennsylvanian) Strata in the South-Eastern Part of the Upper Silesian Coal Basin, Poland, International Journal of Coal Geology, 105, 24–35, https://doi.org/10.1016/j.coal.2012.11.007, 2013.

Keeling, C. D.: The Concentration and Isotopic Abundances of Carbon Dioxide in Rural and Marine Air, Geochimica et Cosmochimica Acta, 24, 277–298, 1961.

Kotarba, M. J.: Composition and Origin of Coalbed Gases in the Upper Silesian and Lublin Basins, Poland, Organic Geochemistry, 32, 163–180, https://doi.org/10.1016/S0146-6380(00)00134-0, 2001.

Kotarba, M. J. and Pluta, I.: Origin of Natural Waters and Gases within the Upper Carboniferous Coal-Bearing and Autochthonous Miocene Strata in South-Western Part of the Upper Silesian Coal Basin, Poland, Applied Geochemistry, 24, 876–889, https://doi.org/10.1016/j.apgeochem.2009.01.013, 2009.

Levin, I., Bergamaschi, P., Dörr, H., and Trapp, D.: Stable Isotopic Signature of Methane from Major Sources in Germany, Chemosphere, 26, 161–177, https://doi.org/10.1016/0045-6535(93)90419-6, 1993.

Luther, A., Kleinschek, R., Scheidweiler, L., Defratyka, S., Stanisavljevic, M., Forstmaier, A., Dandocsi, A., Wolff, S., Dubravica, D., Wildmann, N., Kostinek, J., Jöckel, P., Nickl, A.-L., Klausner, T., Hase, F., Frey, M., Chen, J., Dietrich, F., Nęcki, J., Swolkień, J., Fix, A., Roiger, A., and Butz, A.: Quantifying CH_4 Emissions from Hard Coal Mines Using Mobile Sun-Viewing Fourier Transform Spectrometry, Atmospheric Measurement Techniques, 12, 5217–5230, https://doi.org/10.5194/amt-12-5217-2019, 2019.

Maazallahi, H., Fernandez, J. M., Menoud, M., Zavala-Araiza, D., Weller, Z. D., Schwietzke, S., von Fischer, J. C., Denier van der Gon, H., and Röckmann, T.: Methane Mapping, Emission Quantification, and Attribution in Two European Cities: Utrecht (NL) and Hamburg (DE), Atmospheric Chemistry and Physics, 20, 14 717–14 740, https://doi.org/10.5194/acp-20-14717-2020, 2020.

Mailler, S., Menut, L., Khvorostyanov, D., Valari, M., Couvidat, F., Siour, G., Turquety, S., Briant, R., Tuccella, P., Bessagnet, B., Colette, A., Létinois, L., Markakis, K., and Meleux, F.: CHIMERE-2017: From Urban to Hemispheric Chemistry-Transport Modeling, Geoscientific Model Development, 10, 2397–2423, https://doi.org/10.5194/gmd-10-2397-2017, 2017.

Menoud, M., Röckmann, T., Fernandez, J., Bakkaloglu, S., Lowry, D., Korben, P., Schmidt, M., Stanisavljevic, M., Necki, J., Defratyka, S., and Kwok, C. Y.: Mamenoud/MEMO2_isotopes: V8.1 Complete, https://doi.org/10.5281/ZENODO.4062356, 2020a.

Menoud, M., van der Veen, C., Scheeren, B., Chen, H., Szénási, B., Morales, R. P., Pison, I., Bousquet, P., Brunner, D., and Röckmann, T.: Characterisation of Methane Sources in Lutjewad, The Netherlands, Using Quasi-Continuous Isotopic Composition Measurements, Tellus B: Chemical and Physical Meteorology, 72, 1–19, https://doi.org/10.1080/16000889.2020.1823733, 2020b.

Menut, L., Bessagnet, B., Khvorostyanov, D., Beekmann, M., Blond, N., Colette, A., Coll, I., Curci, G., Foret, G., Hodzic, A., Mailler, S., Meleux, F., Monge, J.-L., Pison, I., Siour, G., Turquety, S., Valari, M., Vautard, R., and Vivanco, M. G.: CHIMERE 2013: A Model for Regional Atmospheric Composition Modelling, Geoscientific Model Development, 6, 981–1028, https://doi.org/10.5194/gmd-6-981-2013, 2013.

Milkov, A. V. and Etiope, G.: Revised Genetic Diagrams for Natural Gases Based on a Global Dataset of >20,000 Samples, Organic Geochemistry, 125, 109–120, https://doi.org/10.1016/j.orggeochem.2018.09.002, 2018.

Miller, J. B. and Tans, P. P.: Calculating Isotopic Fractionation from Atmospheric Measurements at Various Scales, Tellus B: Chemical and Physical Meteorology, 55, 207–214, https://doi.org/10.3402/tellusb.v55i2.16697, 2003.

Monteil, G., Houweling, S., Dlugockenky, E. J., Maenhout, G., Vaughn, B. H., White, J. W. C., and Rockmann, T.: Interpreting Methane Variations in the Past Two Decades Using Measurements of CH_4 Mixing Ratio and Isotopic Composition, Atmospheric Chemistry and Physics, 11, 9141–9153, https://doi.org/10.5194/acp-11-9141-2011, 2011.

National Centre for Emission Management (KOBiZe) and Institute of Environmental Protection - National Research Institute: Poland's National Inventory Report 2020 - Greenhouse Gas Inventory for 1988-2018, Tech. rep., Ministry of climate, Warsaw, Poland, 2020.

Necki, J. M., Chmura, Ł., Zimnoch, M., and Różański, K.: Impact of Emissions on Atmospheric Composition at Kasprowy Wierch Based on Results of Carbon Monoxide and Carbon Dioxide Monitoring, Polish Journal of Environmental Studies, 22, 1119–1127, 2013.

Niemann, M. and Whiticar, M.: Stable Isotope Systematics of Coalbed Gas during Desorption and Production, Geosciences, 7, 43, https://doi.org/10.3390/geosciences7020043, 2017.

Nisbet, E. G., Dlugokencky, E. J., Manning, M. R., Lowry, D., Fisher, R. E., France, J. L., Michel, S. E., Miller, J. B., White, J. W. C., Vaughn, B., Bousquet, P., Pyle, J. A., Warwick, N. J., Cain, M., Brownlow, R., Zazzeri, G., Lanoisellé, M., Manning, A. C., Gloor, E., Worthy, D. E. J., Brunke, E.-G., Labuschagne, C., Wolff, E. W., and Ganesan, A. L.: Rising Atmospheric Methane: 2007-2014 Growth and Isotopic Shift: RISING METHANE 2007-2014, Global Biogeochemical Cycles, 30, 1356–1370, https://doi.org/10.1002/2016GB005406, 2016.

Pataki, D. E., Ehleringer, J. R., Flanagan, L. B., Yakir, D., Bowling, D. R., Still, C. J., Buchmann, N., Kaplan, J. O., and Berry, J. A.: The Application and Interpretation of Keeling Plots in Terrestrial Carbon Cycle Research: APPLICATION OF KEELING PLOTS, Global Biogeochemical Cycles, 17, 1022, https://doi.org/10.1029/2001GB001850, 2003.

Quay, P., Stutsman, J., Wilbur, D., Snover, A., Dlugokencky, E., and Brown, T.: The Isotopic Composition of Atmospheric Methane, Global Biogeochemical Cycles, 13, 445–461, https://doi.org/10.1029/1998GB900006, 1999.

Rigby, M., Manning, A. J., and Prinn, R. G.: The Value of High-Frequency High-Precision Methane Isotopologue Measurements for Source and Sink Estimation: Methane Isotopologues in Inversions, Journal of Geophysical Research: Atmospheres, 117, 1–14, https://doi.org/10.1029/2011JD017384, 2012.

Ringeval, B., Friedlingstein, P., Koven, C., Ciais, P., de Noblet-Ducoudré, N., Decharme, B., and Cadule, P.: Climate-CH_4 Feedback from Wetlands and Its Interaction with the Climate-CO_2 Feedback, Biogeosciences, 8, 2137–2157, https://doi.org/10.5194/bg-8-2137-2011, 2011.

Röckmann, T., Eyer, S., van der Veen, C., Popa, M. E., Tuzson, B., Monteil, G., Houweling, S., Harris, E., Brunner, D., Fischer, H., Zazzeri, G., Lowry, D., Nisbet, E. G., Brand, W. A., Necki, J. M., Emmenegger, L., and Mohn, J.: In Situ Observations of the Isotopic Composition of Methane at the Cabauw Tall Tower Site, Atmospheric Chemistry and Physics, 16, 10 469–10 487, https://doi.org/10.5194/acp-16-10469-2016, 2016.

Saunois, M., Stavert, A. R., Poulter, B., Bousquet, P., Canadell, J. G., Jackson, R. B., Raymond, P. A., Dlugokencky, E. J., Houweling, S., Patra, P. K., Ciais, P., Arora, V. K., Bastviken, D., Bergamaschi, P., Blake, D. R., Brailsford, G., Bruhwiler, L., Carlson, K. M., Carrol, M., Castaldi, S., Chandra, N., Crevoisier, C., Crill, P. M., Covey, K., Curry, C. L., Etiope, G., Frankenberg, C., Gedney, N., Hegglin, M. I., Höglund-Isaksson, L., Hugelius, G., Ishizawa, M., Ito, A., Janssens-Maenhout, G., Jensen, K. M., Joos, F., Kleinen, T., Krummel, P. B., Langenfelds, R. L., Laruelle, G. G., Liu, L., Machida, T., Maksyutov, S., McDonald, K. C., McNorton, J., Miller, P. A., Melton, J. R., Morino, I., Müller, J., Murguia-Flores, F., Naik, V., Niwa, Y., Noce, S., O'Doherty, S., Parker, R. J., Peng, C., Peng, S., Peters, G. P., Prigent, C., Prinn, R., Ramonet, M., Regnier, P., Riley, W. J., Rosentreter, J. A., Segers, A., Simpson, I. J., Shi, H., Smith, S. J., Steele, L. P., Thornton, B. F., Tian, H., Tohjima, Y., Tubiello, F. N., Tsuruta, A., Viovy, N., Voulgarakis, A., Weber, T. S., van Weele, M., van der Werf, G. R., Weiss, R. F., Worthy, D., Wunch, D., Yin, Y., Yoshida, Y., Zhang, W., Zhang, Z., Zhao, Y., Zheng, B., Zhu, Q., Zhu, Q., and Zhuang, Q.: The Global Methane Budget 2000–2017, Earth System Science Data, 12, 1561–1623, https://doi.org/10.5194/essd-12-1561-2020, 2020.

Schaefer, H., Fletcher, S. E. M., Veidt, C., Lassey, K. R., Brailsford, G. W., Bromley, T. M., Dlugokencky, E. J., Michel, S. E., Miller, J. B., Levin, I., Lowe, D. C., Martin, R. J., Vaughn, B. H., and White, J. W. C.: A 21st-Century Shift from Fossil-Fuel to Biogenic Methane Emissions Indicated by $^{13}CH_4$, Science, 352, 80–84, https://doi.org/10.1126/science.aad2705, 2016.

Schwietzke, S., Sherwood, O. A., Bruhwiler, L. M. P., Miller, J. B., Etiope, G., Dlugokencky, E. J., Michel, S. E., Arling, V. A., Vaughn, B. H., White, J. W. C., and Tans, P. P.: Upward Revision of Global Fossil Fuel Methane Emissions Based on Isotope Database, Nature, 538, 88–91, https://doi.org/10.1038/nature19797, 2016.

Sherwood, O. A., Schwietzke, S., Arling, V. A., and Etiope, G.: Global Inventory of Gas Geochemistry Data from Fossil Fuel, Microbial and Burning Sources, Version 2017, Earth System Science Data, 9, 639–656, https://doi.org/10.5194/essd-9-639-2017, 2017.

Sperlich, P., Uitslag, N. A. M., Richter, J. M., Rothe, M., Geilmann, H., van der Veen, C., Röckmann, T., Blunier, T., and Brand, W. A.: Development and Evaluation of a Suite of Isotope Reference Gases for Methane in Air, Atmospheric Measurement Techniques, 9, 3717–3737, https://doi.org/10.5194/amt-9-3717-2016, 2016.

Statistics Poland: Chapter 6 - Odpady (Waste), in: Statistical Yearbook of the Republic of Poland, 2018, Dominik Rozkrut, Statistical Publishing Establishment, Warsaw, Poland, 2018.

Swolkień, J.: Polish Underground Coal Mines as Point Sources of Methane Emission to the Atmosphere, International Journal of Greenhouse Gas Control, 94, 102 921, https://doi.org/10.1016/j.ijggc.2019.102921, 2020.

Szénási, B.: Atmospheric Monitoring of Methane Emissions at the European Scale, PhD thesis, Université Paris-Saclay, 2020.

Tarasova, O., Brenninkmeijer, C., Assonov, S., Elansky, N., Rockmann, T., and Brass, M.: Atmospheric CH4 along the Trans-Siberian Railroad (TROICA) and River Ob: Source Identification Using Stable Isotope Analysis, Atmospheric Environment, 40, 5617–5628, https://doi.org/10.1016/j.atmosenv.2006.04.065, 2006.

Townsend-Small, A., Botner, E. C., Jimenez, K. L., Schroeder, J. R., Blake, N. J., Meinardi, S., Blake, D. R., Sive, B. C., Bon, D., Crawford, J. H., Pfister, G., and Flocke, F. M.: Using Stable Isotopes of Hydrogen to Quantify Biogenic and Thermogenic Atmospheric Methane Sources: A Case Study from the Colorado Front Range: Hydrogen Isotopes in the Front Range, Geophysical Research Letters, 43, 11,462–11,471, https://doi.org/10.1002/2016GL071438, 2016.

Turner, A. J., Frankenberg, C., and Kort, E. A.: Interpreting Contemporary Trends in Atmospheric Methane, Proceedings of the National Academy of Sciences, 116, 2805–2813, https://doi.org/10.1073/pnas.1814297116, 2019.

Worden, J. R., Bloom, A. A., Pandey, S., Jiang, Z., Worden, H. M., Walker, T. W., Houweling, S., and Röckmann, T.: Reduced Biomass Burning Emissions Reconcile Conflicting Estimates of the Post-2006 Atmospheric Methane Budget, Nature Communications, 8, 2227, https://doi.org/10.1038/s41467-017-02246-0, 2017.

Yacovitch, T. I., Daube, C., and Herndon, S. C.: Methane Emissions from Offshore Oil and Gas Platforms in the Gulf of Mexico, Environmental Science & Technology, 54, 3530–3538, https://doi.org/10.1021/acs.est.9b07148, 2020.

Zazzeri, G., Lowry, D., Fisher, R. E., France, J. L., Lanoisellé, M., Grimmond, C. S. B., and Nisbet, E. G.: Evaluating Methane Inventories by Isotopic Analysis in the London Region, Scientific Reports, 7, 4854, https://doi.org/10.1038/s41598-017-04802-6, 2017.

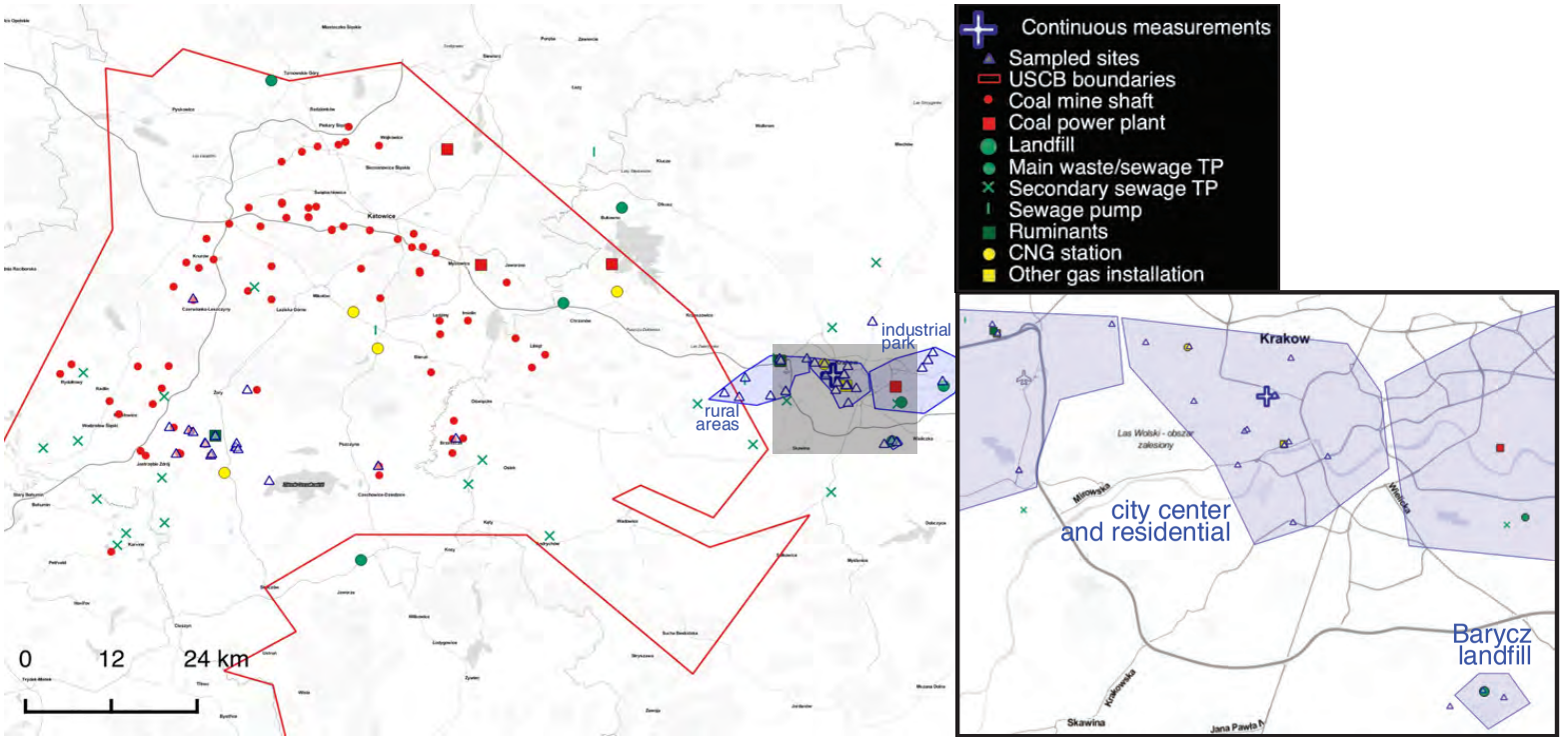

Figure 1. Location of the long-time measurements, sampled sites and potential anthropogenic methane sources. Note that this is not an exhaustive list: not all the sewage pumps are reported, and no official information on cattle farms was obtained. Other emissions from mining activities, coming from processing facilities or waste disposal, are not reported here. No $\chi(CH_4)$ enhancements were measured around stagnant water bodies, therefore they are not all reported here. ("TP" = treatment plant, "CNG" = compressed natural gas)

Sources: https://www.google.com/maps (locations), OpenStreetMap contributors (map)

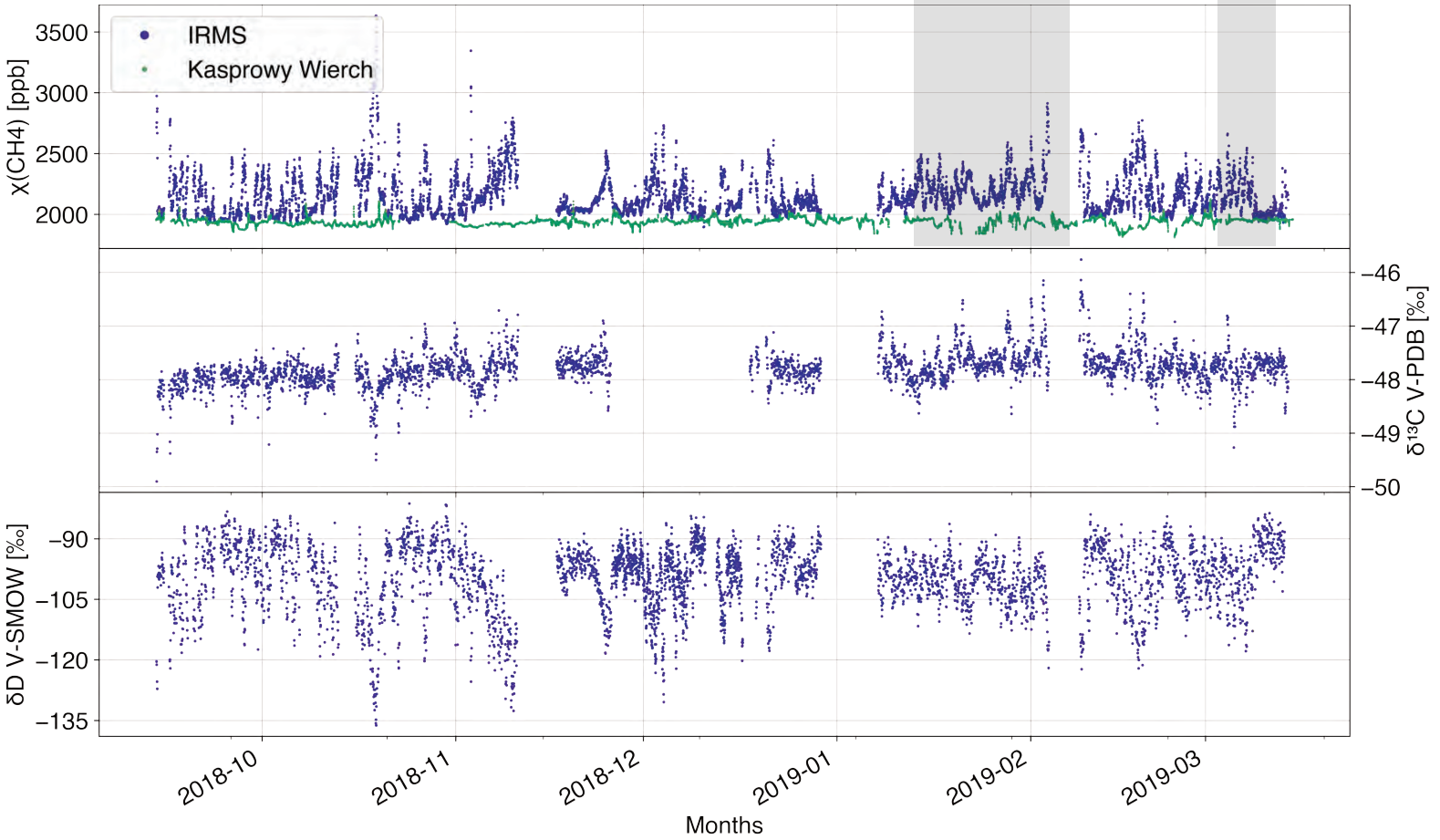

Figure 2. Time series of the observed $\chi(CH_4)$ (n=7886), $\delta^{13}C$ (n=3477), and $\delta^{2}H$ (n=4389), together with the $\chi(CH_4)$ time series observed at Kasprowy Wierch (green; n=21028). The shaded areas show when there was a mismatch between the IRMS and CRDS instruments in the mole fractions.

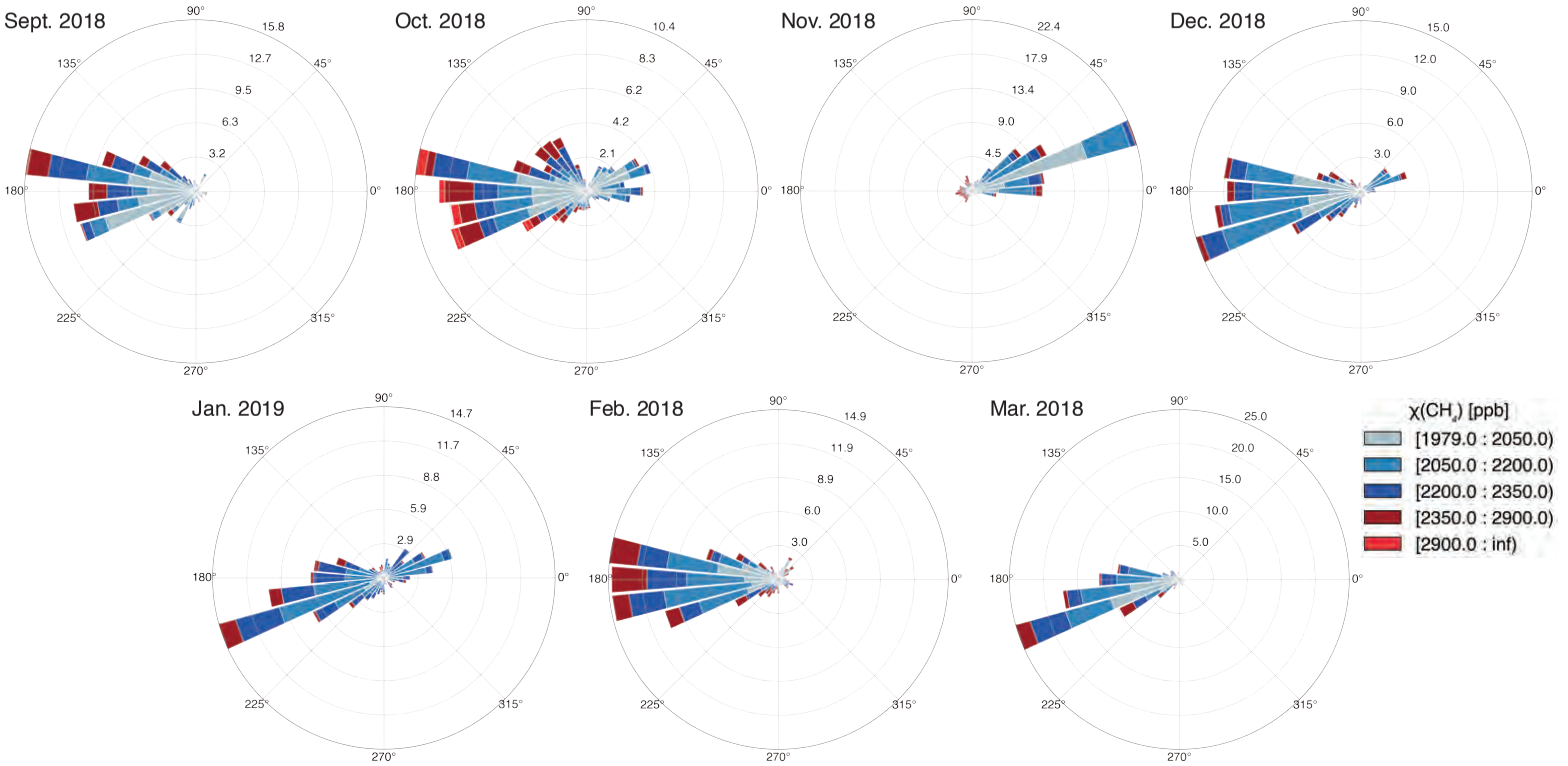

Figure 3. Monthly wind directions during the ambient air measurement period, at the same location. Bar lengths are percentages of records during the specified month (r-axis); colours define the $\chi(CH_4)$ range (legend).

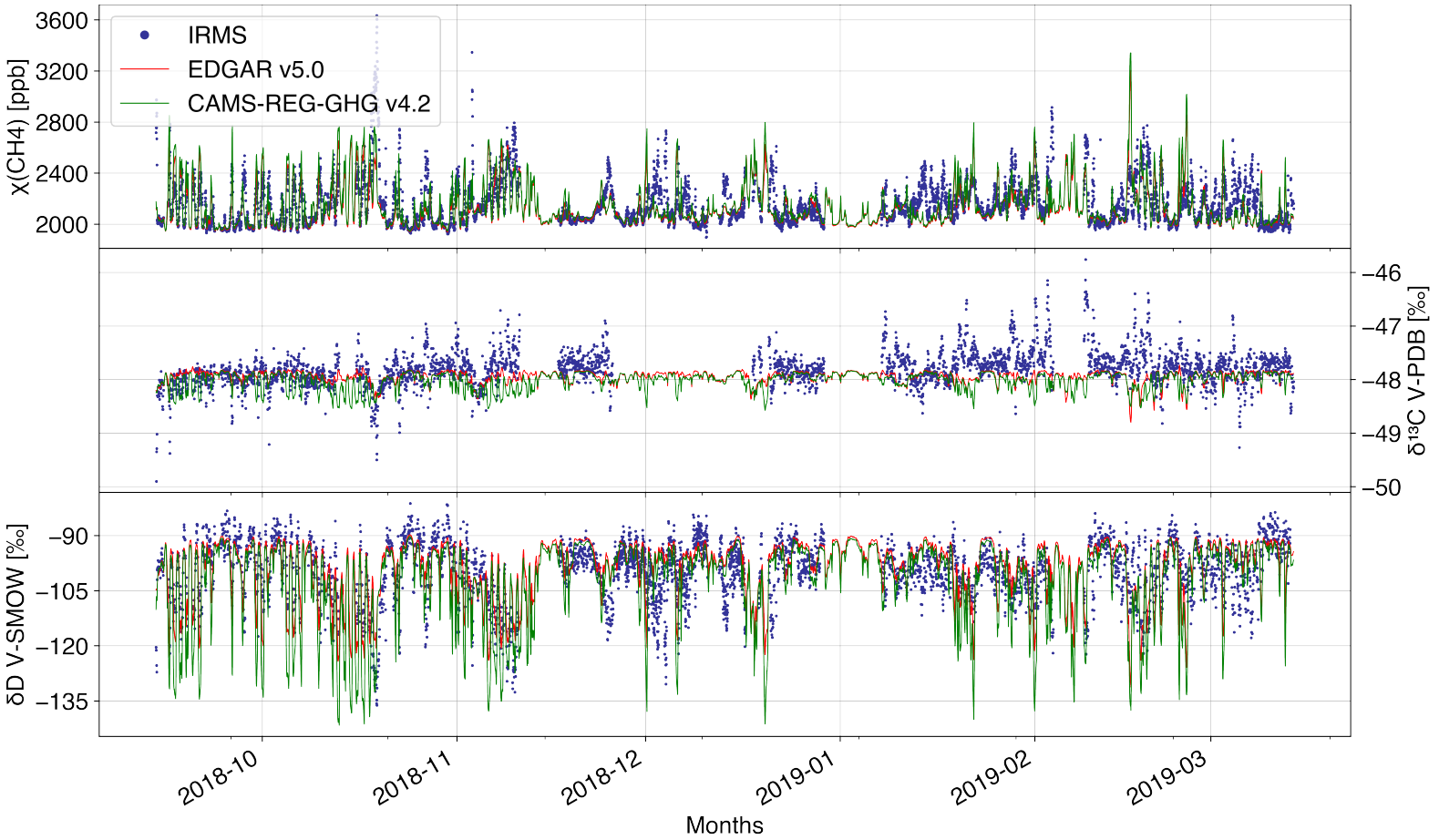

Figure 4. Time series of the observed (blue circles) and modelled $\chi(CH_4)$, $\delta^{13}C$ and $\delta^{2}H$, based on the EDGAR v5.0 (red) and CAMS-REG-GHG v4.2 (green) inventories.

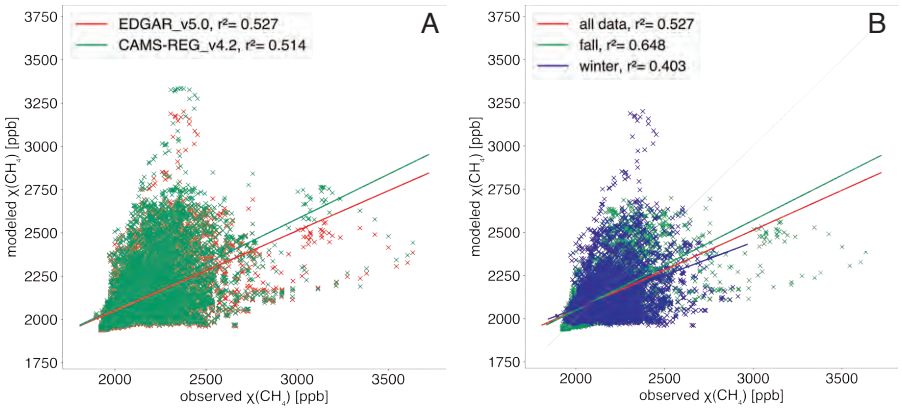

Figure 5. Correlation between observed and modelled $\chi(CH_4)$ values, using (a) the EDGAR v5.0 (red) or the CAMS-REG-GHG v4.2 (green) inventories, and (b) different time periods: fall (September 14 to November 15, 2018; green) or winter (November 15, 2018 to March 15, 2019; blue) computed using EDGAR v5.0.

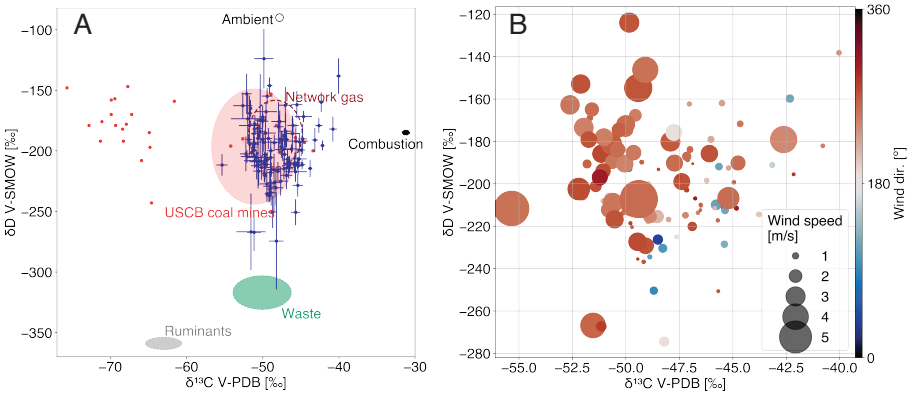

Figure 6. Dual isotope plots of the resulting source signatures from the CH_4 peaks identified in the time series. (a) Dark blue: source signatures with their associated 1σ uncertainties. Coloured areas: ranges of source signatures obtained from the collected samples. Red dots: source signatures of USCB coal gas derived from Kotarba (2001), Kotarba and Pluta (2009) and Kedzior et al. (2013). The combustion source signature is from coal waste burning samples reported in Menoud et al. (2020a). (b) Source signatures labeled by the average wind direction (colour) and speed (size) measured during the pollution event.

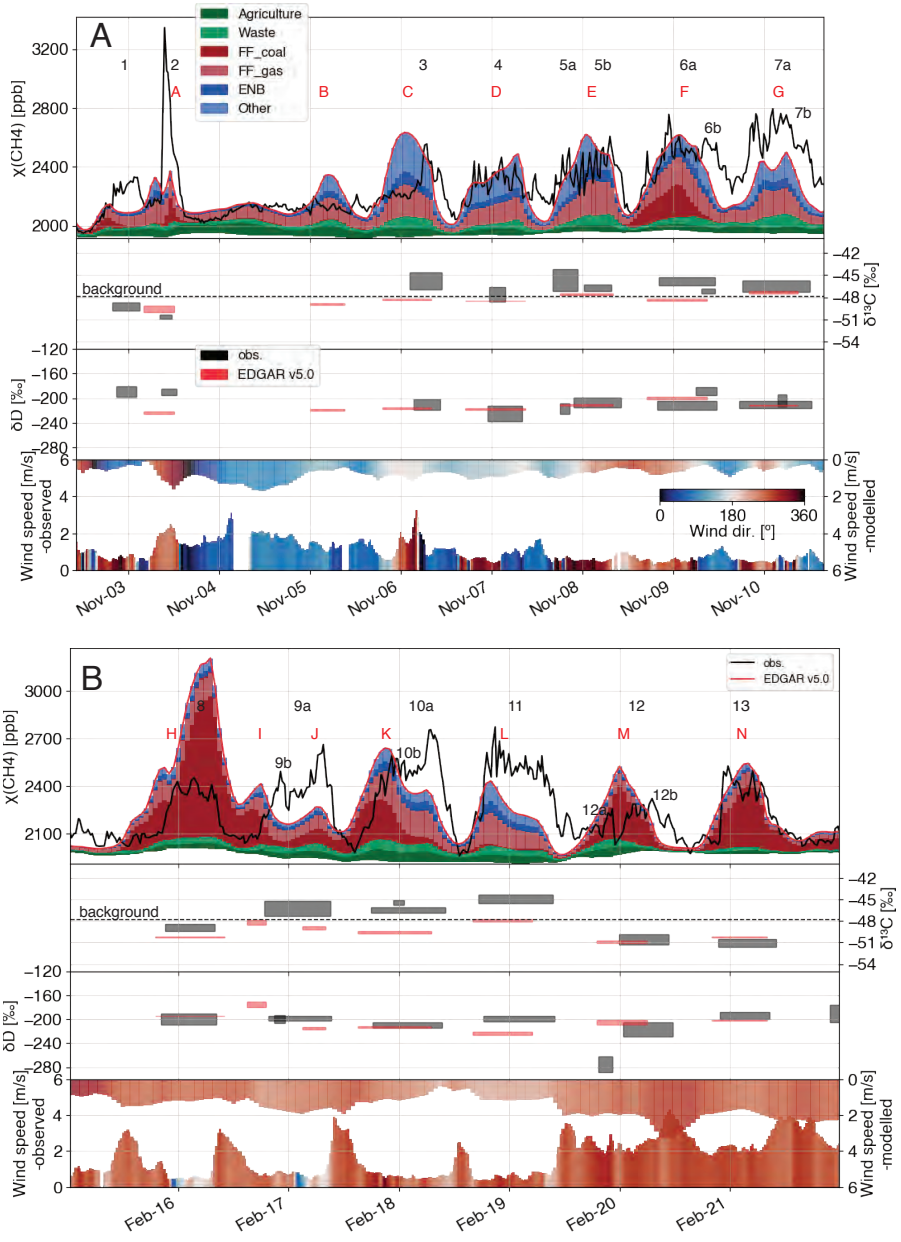

Figure 7. Detailed analysis of two subsets of the dataset, (a) from Nov. 2 to 10, 2018, (b) from Feb. 15 to 22, 2019. Top panels: observed (grey) and modelled (red) mole fractions and relative source contributions from the EDGAR v5.0 inventory. Middle panels: δ^{13}C and δ^{2}H source signatures of individual peaks of the observed (grey, from peak 1 to 13) and modelled (red, from peak A to N) time series. Box heights represent $\pm 1\sigma$ of each peak isotopic signature. Bottom panels: wind speed and direction measured simultaneously at the study site (pointing up), and used for the CHIMERE simulations (pointing down).

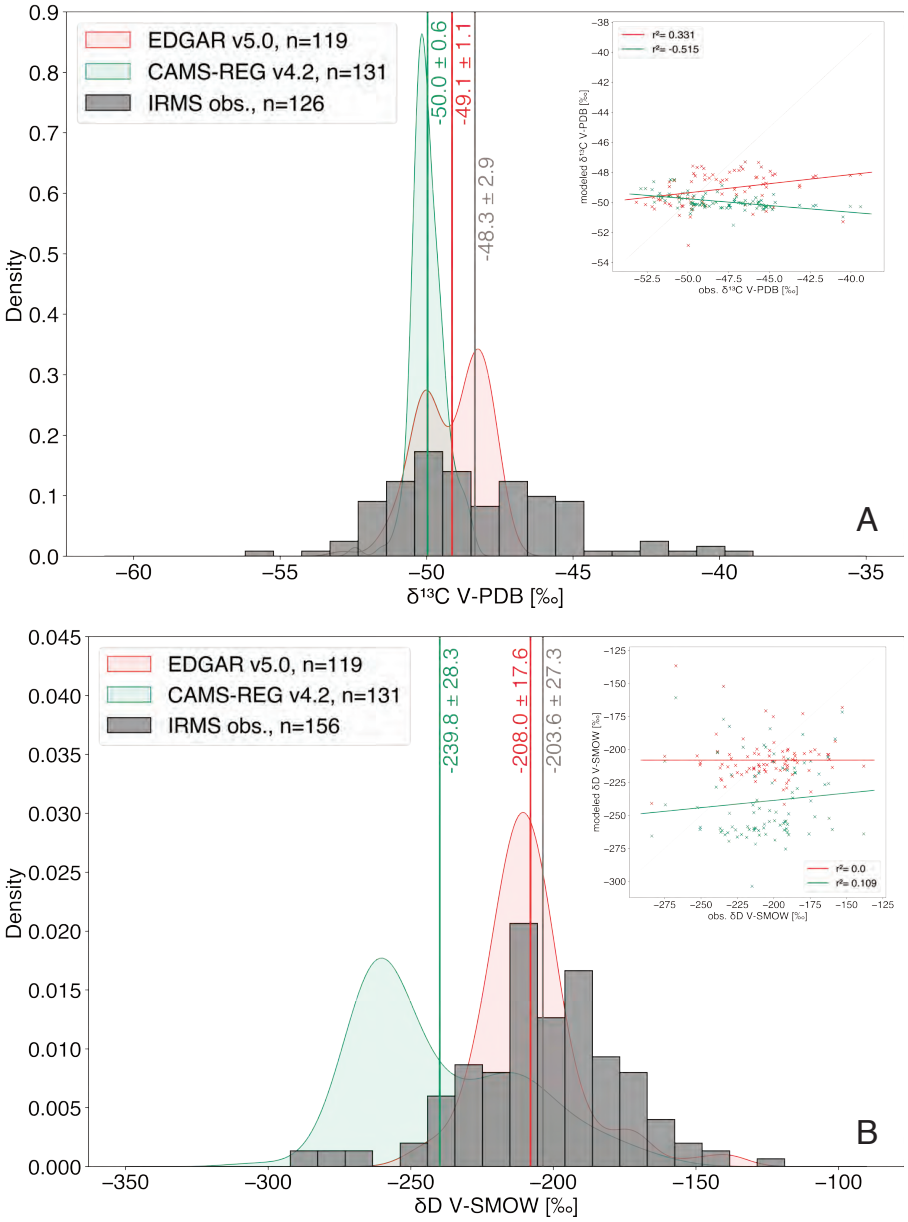

Figure 8. Distribution of source signatures of all peaks, and in the inset the correlation between modelled and observed ones. The vertical lines show the average values of each distribution ($\pm$ 1σ). (a) δ^{13}C signatures in the observed (grey, n=126), modelled using EDGAR v5.0 (red, n=119) and modelled using CAMS-REG-GHG v4.2 (green, n=131) time series. (b) δ^{2}H signatures in the observed (grey, n=157), modelled using EDGAR v5.0 (red, n=119) and modelled using CAMS-REG-GHG v4.2 (green, n=131) time series.

Table 1. Methane emission categories considered for this study, with the corresponding classification in the inventories, and the respective isotopic signature used to compute $\delta^{13}C$ and $\delta^{2}H$ time series with CHIMERE. If no references are specified, the assigned isotope values are derived from the sampling campaigns we carried out in the study area as described below.

CHIMERE source category	CRF sector[1]		IPCC 2006 code	EDGAR v5.0 sector	CAMS-REG-GHG v4.2 sector		Assigned $\delta^{13}C$ V-PDB [‰]	Assigned $\delta^{2}H$ SMOW [‰]
Agriculture	3	Agriculture	3A1 3A2 3C1b 3C2, 3C3, 3C4, 3C7	Enteric fermentation Manure management Agriculture waste burning Agriculture soils	K L	Agriculture -livestock Agriculture -other	-63	-359
Waste	5	Waste	4A, 4B 4C 4D	Solid waste landfills Solid waste incineration Waste water handling	J	Waste	-51.6	-299
Fossil fuels	1B	Energy - Fugitive emissions from fuels	1B1a 1bB2bi, 1B2bii 1B2aiii2, 1B2aiii3	Fuel explotation, coal Fuel explotation, gas Fuel explotation, oil	D	Fugitives	-51 -48.5 -49.3	-192 -194 -193
Non-industrial combustion	1A4, 1A5	Energy - Other sectors, Other[2]	1A4, 1A5	Energy for buildings	C	Other stationary combustion	-32.1[3]	-185[3]
Other anthropogenic	1A	Energy - Industries	1A1a 1A1b, 1A1ci, 1A1cii, 1A5biii, 1B1b, 1B2aiii6, 1B2biii3, 1B1c 1A2	Power industry Oil refineries and transformation industry Combustion for manufacturing	A	Public power	-49.3	-193
	2	Industrial processes and product use	5B 2B 2C1, 2C2 2D3, 2E, 2F, 2G	Fossil fuel fires Chemical processes Iron and steel production Solvents and products use	B E	Industry Solvents		
	1A3	Energy - Transport	1A3b 1A3d 1A3a 1A3c, 1A3e	Road transportation Shipping Aviation Railways, pipelines, off-road transport	F G H I	Road transport Shipping Aviation Off-road		
Wetlands							-73.2[3]	-323[3]
Background							-47.8	-89

[1] European Environment Agency (2019)

[2] Mostly the use of coal for heating households (European Environment Agency (2019))

[3] Menoud et al. (2020ab)

Table 2. Isotope signatures of the different sources sampled in the region surrounding the study site.

Source type	Number of sites	Mean δ^{13}C V-PDB [‰]	1σ	Mean δ^{2}H V-SMOW [‰]	1σ
Coal mine	16	-51.0	7.1	-191.6	27.8
Cow barn	1	-63.0		-358.7	
Landfill	2	-55.4	0.8	-275.0	34.5
Manhole	8 (5/3)	-45.0 (-42.5/-49.1)	9.0 (10.9/3.1)	-233.7 (-176.4/-329.2)	81.0 (21.1/12.3)
Network gas	7 (1)	-48.5 (-51.4)	2.9 (0.4)	-193.6 (-205.0)	17.3 (0.001)
Unknown	23	-49.0	6.2	-195.3	39.8

Table 3. Methane absolute emissions and contributions of the different source categories used in CHIMERE to the total simulated $\chi(CH_4)$, for the EDGAR v5.0 and CAMS-REG-GHG v4.2 inventories.

	Emissions over domain [$TgCH_4/yr$]		Contribution at Krakow [ppb/ppb]	
Source categories	EDGAR v5.0	CAMS-REG-GHG v4.2	EDGAR v5.0	CAMS-REG-GHG v4.2
Agriculture	2.02	1.64	0.168	0.114
Waste	1.88	1.22	0.142	0.438
Fossil fuels - coal	0.52	-	0.145	
Fossil fuels - gas	1.23	-	0.309	
Fossil fuels - oil	0.02	-	0.00226	
Fossil fuels - total	1.77	1.32	0.456	0.346
Non-industrial combustion/Energy for buildings	0.31	0.28	0.0986	0.0667
Other anthropogenic	0.09	0.16	0.118	0.0201
Wetlands	0.4		0.0178	0.0157
Total	6.07	4.64	1	1